Atoms on a Worldline: A Path-Integral Approach to Electromagnetic Casimir Energies

by

He Zheng

A dissertation accepted and approved in partial fulfillment of the
requirements for the degree of
Doctor of Philosophy
in Physics

Dissertation Committee:

Steven van Enk , Chair

Daniel Steck , Advisor

Dietrich Belitz , Core Member

Michael Kellman , Institutional Representative

University of Oregon

Summer 2025

DISSERTATION ABSTRACT

He Zheng

Doctor of Philosophy in Physics

Title: Atoms on a Worldline: A Path-Integral Approach to Electromagnetic Casimir Energies

The Casimir effect arises from quantum fluctuations of the electromagnetic field and leads to observable forces between material bodies even in vacuum. While the Casimir force between simple geometries has been well studied, accurately calculating Casimir interactions in general or many-body configurations remains a challenging problem, especially when electromagnetic vector properties and material responses are taken into account.

Among the primary advancements in computational tools for Casimir physics, the worldline path-integral approach provides a powerful alternative to traditional mode summation and scattering approaches by reformulating the quantum vacuum energy in terms of an ensemble of fluctuating particle paths. The worldline method offers strong potential for handling arbitrary geometries through intuitive Monte Carlo sampling and parallelizable algorithms. However, most prior worldline formulations are restricted to scalar fields or simplified boundary conditions.

This dissertation aims to extend and strengthen the worldline formalism in both numerical and analytical directions. First, it develops a pathwise

differentiation technique that enables efficient computation of Casimir forces and higher derivatives of the energy numerically. Second, the thesis contrasts with the Green-tensor formalism and investigates the breakdown of scalar approximations in electromagnetic Casimir worldlines between discrete polarizable atoms, highlighting the necessity of vectorial field treatments in the worldline method. These findings demonstrate the critical effects of electromagnetic polarization mixing in Casimir energy computations and suggest new pathways for studying dispersion forces in many-body systems.

This dissertation contains previously published as well as unpublished co-authored materials.

CURRICULUM VITAE

NAME OF AUTHOR: He Zheng

GRADUATE AND UNDERGRADUATE SCHOOLS ATTENDED:

University of Oregon, Eugene, OR, USA

University of California Los Angeles, Los Angeles, CA, USA

DEGREES AWARDED:

Doctor of Philosophy, Physics, 2025, University of Oregon

Bachelor of Science, Physics, 2017, UCLA

Bachelor of Science, Mathematics, 2017, UCLA

AREAS OF SPECIAL INTEREST:

Quantum Optics

Atomic Physics

PROFESSIONAL EXPERIENCE:

Graduate Teaching Assistant, University of Oregon, 2018 – 2025

GRANTS, AWARDS AND HONORS:

Departmental Highest Honors, UCLA, 2017

Weiser Physics Teaching Award, University of Oregon, 2023

Emanuel Optical, Molecular, and Quantum Sciences Fellowship, 2025

PUBLICATIONS:

H. Zheng and D. A. Steck. Preprint: arXiv:2502.15997 [quant-ph].

J. B. Mackrory, H. Zheng, and D. A. Steck. Phys. Rev. A 110, 042826 (2024).

T. Cohen, S. Majewski, B. Ostdiek and P. Zheng. JHEP 06 (2020) 019.

ACKNOWLEDGEMENTS

I would like to express deep gratitude to my advisor, Prof. Daniel Steck, for the guidance and scientific insights throughout the doctoral journey. I am thankful to the committee members for their constructive feedback and thought-provoking questions, which have helped me refine and strengthen my research work.

I also wish to thank my collaborators and fellow graduate students for the many valuable discussions and shared moments in physics.

Lastly, I am grateful to my parents for their support and encouragement along the way.

TABLE OF CONTENTS

Chapter Page

I INTRODUCTION TO CASIMIR PHYSICS 13

1.1 Historical Background and Physical Origin 13
1.2 Casimir Pressure Between Parallel Plates 17
1.3 Quantum Electrodynamics with Magnetodielectric Media 22
1.4 Atom Interacting with a Planar Surface 24
1.5 An Overview of Experiments 29
1.6 An Overview of Computational Methods 35

II ELECTROMAGNETIC WORLDLINE FORMALISM 41

2.1 Introduction 41
2.2 Path Integrals 42
2.3 Scalar Field Worldline Formulation 47
2.4 Worldline Form of Scalar Electromagnetism 53
2.5 Monte Carlo Simulation 65

III PATHWISE DIFFERENTIATION OF WORLDLINE PATH INTEGRALS 76

3.1 Introduction 76
3.2 Derivatives of Worldline Casimir–Polder Energies 79

Chapter Page

3.3 Differentiation of Worldline Casimir Energies 94

3.4 Numerical Results 100

3.5 Summary 116

Appendix to Chapter III 119

A.1 Boundary Crossing Statistics 119

A.2 Derivation of the TE-Mode Casimir Energy Between Two Thin Delta-Planes 123

A.3 Fitting Range and Parameters 133

IV THE VALIDITY OF SCALAR APPROXIMATION 134

4.1 Introduction 134

4.2 Green Tensor Calculation of the Casimir–Polder Potential Between Atoms 135

4.3 Multi-Atom Generalization of Scalar Worldlines 144

4.4 The Breakdown of Scalar Approximation at $N = 3$ 156

4.5 Physical Interpretation and Future Direction 160

Appendix to Chapter IV 163

A.1 Derivation of $N = 3$ Co-linear Casimir–Polder Potential with Green-Tensor Decomposition 163

REFERENCES CITED 167

LIST OF FIGURES

Figure Page

1.1. A sketch of the parallel-plate setup and the constrained electromagnetic modes. Only blue modes with half integer multiples of wavelength are allowed between the plates. 14

1.2. Feynman diagram representing a ground-state atom interacting with EM field through emission and re-absorption of virtual photons. 27

2.1. Decomposition of electromagnetic modes into TE and TM polarizations for a planar stratified system. TE modes have the electric field perpendicular to the plane of incidence, while TM modes have the magnetic field perpendicular to it. 55

2.2. Casimir–Polder worldlines pinned to the atomic position. (a) The vacuum loop does not contribute to the potential. (b) Only the one that sojourns the medium contributes. 64

2.3. Linear drift applied to Wiener processes to force the bridge closure. . . 67

3.1. Schematic path showing partial averaging up to the mth discrete path increment up to and after the source point $\mathbf{x}_0$. The diagram shows the example geometry of the Casimir–Polder potential for an atom in vacuum near a planar interface with a dielectric material of susceptibility χ. . . 87

3.2. Schematic of an atom between two dielectric half-spaces with respective susceptibilities χ_1 and χ_2, illustrating the prototype problem for the partial-averaging technique of Section 3.2.3 close to one body. The dashed spheres show the typical extent of the paths at various running times $\mathcal{T}$ (i.e., times over which the paths can diffuse). At $\mathcal{T}_1$ the paths typically touch only the nearer body, while at $\mathcal{T}_2$ they typically touch *both* bodies. The time interval for partial averaging the paths is $\mathcal{T}_m$. The method of Sec. 3.2.2 requires the background dielectric to be approximately uniform in the vicinity of the atom, and thus that $\mathcal{T}_m \ll \mathcal{T}_1$ so that the paths are unlikely to touch either interface during the partial-averaging time. However, because the path integral can be evaluated in the presence of a single, planar interface, the partial averaging can be extended such that $\mathcal{T}_m \sim \mathcal{T}_1$, provided $\mathcal{T}_m \ll \mathcal{T}_2$, so that most paths only hit the nearer interface during the partial-averaging time. 90

Figure Page

3.3. Geometry for interacting dielectric bodies of susceptibility χ_j, centered at $\mathbf{R}_j$ relative to the origin. The normal vectors $\hat{n}_j$ to the surface of the jth body are also shown. 95

3.4. Numerical evaluation of the path integral (3.4) for the (normalized, dimensionless) Casimir–Polder potential of an atom near a dielectric half-space, as a function of the (dimensionless) dielectric susceptibility χ (data shown as circles). The remaining curves, each successively offset by a factor of 10^{-2} for clarity, show spatial derivatives of the potential according to the method of Eq. (3.11), for $n = 1$ (squares), 2 (diamonds), 4 (triangles), 7 (inverted triangles), and 10 (stars) derivatives. The solid lines give the analytic result (3.45) for comparison in each case. Error bars delimit one standard error. Details of the calculations are given in the text, but the computational difficulty increases with increasing n, and accuracy noticeably suffers by the $n = 10$ case. The same random numbers are used for all the points in the same curve. 104

3.5. Magnitude of the relative error in the computation of (a) one spatial derivative and (b) two derivatives of the atom–surface Casimir–Polder potential, for a surface dielectric susceptibility $\chi = 100$. The plots compare the performance of the finite-difference (circles) and partial-averaging (triangles) methods. The finite-difference data are plotted with respect to the spatial displacement δ, normalized to the atom–surface distance d, while the partial-averaging results are plotted as a function of the averaging fraction m/N, where m appears in Eq. (3.16) and N is the number of points per discrete path. The calculations employed paths with $N = 10^4$ points per path, averaging over 10^{11} paths. Error bars delimit one standard error. The lines are fits to the data (except for the second derivative in the finite-difference case), and the intersection (marked by a star) gives the estimated best performance of the method. Data points within each method are statistically independent. 105

3.6. Magnitude of the relative error in the computation of (a) one spatial derivative and (b) two derivatives of the atom–surface Casimir–Polder potential. The calculations here are similar to those in Fig. 3.5, except here the surface is a perfect conductor ($\chi \longrightarrow \infty$). Also, the calculations here employed paths with $N = 10^6$ points per path (with subpaths of 10^5 points on either side of the point closest to the surface), averaging over 10^9 paths. Other details are as in Fig. 3.5. 107

3.7. Numerical evaluation of the derivatives of the path integral (3.2) for the (normalized, dimensionless) Casimir potential of two dielectric thin planes, as a function of the (dimensionless) susceptibility parameter $\hat{\chi}$

(data shown as circles). The first ($n = 1$) derivative is shown (circles) along with the second ($n = 2$) derivative (squares, offset by a factor 10^{-2} for clarity). The solid lines give the derivatives of the analytic result (3.50) for comparison in each case. The calculation used 10^9 paths of 10^5 points per path. Error bars delimit one standard error (on the order of a few times 10^{-4} to a few times 10^{-3} in this plot). The same random numbers are used for the points in each curve. 111

3.8. Magnitude of the relative error in the computation of (a) one spatial derivative and (b) two derivatives of the Casimir potential for two thin planes, for susceptibility parameter $\hat{\chi} = 1$. The plots compare the performance of the finite-difference (circles) and partial-averaging (triangles) methods; the second derivative additionally has one finite difference applied to each surface (squares). The finite-difference data are plotted with respect to the spatial displacement δ, normalized to the atom–surface distance d, while the partial-averaging results are plotted as a function of the averaging fraction m/N, where m appears in Eq. (3.16) and N is the number of points per discrete path. The calculations employed paths with $N = 10^5$ points per path, averaging over 10^9 paths. Error bars delimit one standard error. The lines are fits to the data, and the intersection (marked by a star) gives the estimated best performance of the method. Data points within each method are statistically independent. 117

3.9. Magnitude of the relative error in the computation of (a) one spatial derivative and (b) two derivatives of the Casimir potential for 2 thin planes, for susceptibility parameter $\hat{\chi} = 0.01$. Details are as in Fig. 3.8. 118

4.1. A sketch of two atoms interacting with each other in the worldline picture. The path of total running time $\mathcal{T}$ starts from one atom and is set to hit the second atom at an arbitrary intermediate time τ'. 147

4.2. The Casimir–Polder coefficients for the three-body interaction obtained from the worldline scalar sum and the Green tensor method, as a function of the cosine of the angle between the displacement vectors. The comparison for $b/c = 0.5$ is shown in (a), where the collinear configuration corresponds to $\cos\theta = 1$. The case $b/c = 1$ is shown in (b), where the equilateral-triangle configuration corresponds to $\cos\theta = 0.5$. In both cases, the energy shift is plotted in units of $\hbar c\alpha_1\alpha_2\alpha_3/(4\pi\varepsilon_0)^3\pi R^{10}$. . . 159

CHAPTER I

INTRODUCTION TO CASIMIR PHYSICS

This thesis comprises research projects unified by the goal of extending the worldline approach to Casimir energy calculations toward broader applicability.

1.1 Historical Background and Physical Origin

The Casimir effect is one of the most remarkable and conceptually illuminating phenomena arising from the interplay between quantum field theory and macroscopic boundary conditions. First predicted by Hendrik Casimir in 1948 [1], the effect refers to the emergence of a measurable force between two neutral, perfectly conducting plates in vacuum due solely to the quantization of the electromagnetic field. The original calculation, carried out in the context of quantum electrodynamics (QED), showed that the modification of vacuum fluctuations between the plates results in a net attractive force. This prediction challenged the classical view of the vacuum as inert and featureless, instead portraying it as a dynamic entity teeming with zero-point fluctuations.

In Casimir's canonical setup, two parallel plates are placed at a fixed separation a, and the electromagnetic field is required to vanish on their surfaces. A sketch is shown in Fig. 1.1. The boundary conditions discretize the allowed modes of the field, effectively excluding long-wavelength modes between the plates compared to the unbounded vacuum outside. The vacuum energy, which is formally the sum of the zero-point energies $\frac{1}{2}\hbar\omega$ of all allowed modes, becomes geometry-dependent due to this restriction. Casimir computed the difference in vacuum energy between the

confined and free cases and found the resulting force per unit area to be

$$F = -\frac{\pi^2 \hbar c}{240 a^4}, \tag{1.1}$$

a strikingly simple and universal result that depends only on fundamental constants and the separation between the plates.

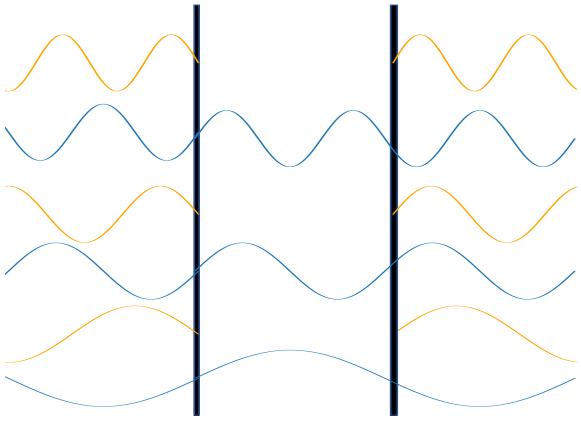

FIGURE 1.1. A sketch of the parallel-plate setup and the constrained electromagnetic modes. Only blue modes with half integer multiples of wavelength are allowed between the plates.

At the time of Casimir's prediction, the physical reality of zero-point energy itself was still a topic of debate. However, subsequent theoretical developments and increasingly precise experiments have confirmed the existence of Casimir forces, solidifying their role in modern physics. The first clear experimental observation was achieved by Sparnaay in the 1950s, though with limited precision. More definitive measurements came decades later, notably by Lamoreaux (1997) and Mohideen & Roy (1998), who confirmed the Casimir force between metallic surfaces to within a few percent of theoretical predictions. These experiments, together with advances in nanotechnology, have propelled the Casimir effect from a theoretical curiosity

to a practical consideration in micro-electromechanical systems (MEMS), where unwanted stiction due to Casimir forces can lead to device failure.

While the Casimir effect can be regarded as a general feature of quantum field theory subject to boundary conditions, the electromagnetic Casimir effect is particularly significant. Unlike scalar fields, the electromagnetic field possesses massless quanta—photons—whose long-range interactions dominate over other forces at macroscopic distances. Moreover, the electromagnetic coupling to matter is vastly stronger than gravity, the only other long-ranged fundamental interaction, making Casimir forces observable even at micrometer scales.

Physically, the Casimir effect can be interpreted in several complementary ways. In the field-theoretic picture, it results from alterations in the vacuum zero-point energy due to boundary-induced modifications of the electromagnetic mode structure. Alternatively, at the microscopic level, it can be viewed as a manifestation of the interaction between fluctuating electric dipoles in different bodies via the exchange of virtual photons. This viewpoint connects the Casimir effect seamlessly to van der Waals forces, first described by van der Waals in 1873, where quantum fluctuations of instantaneous dipole moments lead to attractive forces between molecules. In fact, the Casimir–Polder potential, derived by Casimir and Polder in 1948, explicitly describes the interaction between a neutral atom and a conducting wall as a retarded extension of the van der Waals force, highlighting the unification of these phenomena under the framework of quantum electrodynamics.

Beyond its foundational role as a signature of quantum vacuum fluctuations, the Casimir effect has grown increasingly important in both experimental physics and technological applications. Its first unambiguous measurement was achieved by Lamoreaux in 1997 [2], who introduced a sphere-plane geometry to circumvent

the alignment challenges of parallel-plate setups. This configuration, combined with precision torsion balance techniques, enabled reliable force measurements at submicron separations. Since then, the Casimir force has been confirmed across a wide range of materials and geometries. In micro- and nano-scale systems, vacuum-induced forces can significantly affect device operation, making Casimir effects an essential consideration in nanoscale engineering. Moreover, precision Casimir experiments have been proposed as sensitive tests of physics beyond the Standard Model, including searches for hypothetical forces or light scalar particles coupling to matter at short range. A more detailed account of key experimental milestones is presented in Sec. 1.5.

In addition to being a testbed for quantum field theory, the Casimir effect plays an increasingly critical role in modern technologies and quantum information science. In microelectromechanical systems (MEMS), Casimir forces can induce stiction, causing mechanical components to adhere and potentially fail [3]. Similarly, Casimir forces influence the behavior of ultracold atoms near dielectric surfaces, setting fundamental limits on trapping distances and coherence times [4, 5, 6]. These technological implications have driven the need for accurate and flexible computational methods capable of predicting Casimir interactions in realistic geometries and materials.

The nontrivial dependence of the Casimir effect on geometry, material properties, and temperature has spurred the development of a wide range of theoretical approaches. While early calculations relied on mode summation and idealized assumptions, more sophisticated methods have since emerged, including scattering theory approaches, Green's function techniques, and path integral formulations. Of particular interest is the worldline method — the focus of this thesis — which provides a geometrically intuitive and numerically powerful tool for tackling

general configurations. Initially developed for scalar fields interacting with idealized backgrounds, extending the worldline approach to the full electromagnetic case remains a challenging but promising direction for Casimir physics.

1.2 Casimir Pressure Between Parallel Plates

The Casimir effect provides one of the most tangible demonstrations of the nontrivial structure of the quantum vacuum. Quantum field theory reveals that the vacuum state is populated by fluctuating fields, a consequence of the Heisenberg uncertainty principle. These fluctuations give rise to a nonzero ground state energy, known as zero-point energy, for each mode of the quantized field.

For the electromagnetic field, each mode with wavevector $\mathbf{k}$ and polarization λ behaves as an independent harmonic oscillator, contributing a zero-point energy $\frac{1}{2}\hbar\omega_k$, where $\omega_k = c|\mathbf{k}|$. The formal expression for the vacuum energy is therefore $E_{\text{vac}} = \frac{1}{2}\sum_{k,\lambda}\hbar\omega_k$.

Although the sum diverges, differences in vacuum energy between physical configurations, such as the presence or absence of boundaries, yield finite and measurable quantities. Introducing material boundaries modifies the allowed field modes, resulting in a shift in the vacuum energy E_0, which manifests as a force:

$$F = -\frac{\partial \Delta E_0}{\partial a}, \tag{1.2}$$

where a denotes the separation between the bodies. For a simple, parallel configuration as shown in Fig. 1.1, the quantum zero-point energy of the electromagnetic field between two perfectly conducting plates of area A at zero

temperature can be formally expressed as

$$\begin{aligned} E_0(a) &= \frac{1}{2}\sum_{k,\lambda}\hbar\omega_k \\ &= \frac{1}{2}\hbar c\sum_{\mathbf{k}_\perp}\sum_{n=-\infty}^{\infty}\sqrt{\mathbf{k}_\perp^2+(\frac{\pi n}{a})^2} \\ &= \frac{1}{2}\hbar cA\int_{-\infty}^{\infty}\frac{d^2k_\perp}{(2\pi)^2}\sum_{n=-\infty}^{\infty}\sqrt{\mathbf{k}_\perp^2+(\frac{\pi n}{a})^2}. \end{aligned} \tag{1.3}$$

The direct mode-summation approach to the Casimir effect leads to formally divergent expressions due to the contribution of infinitely many high-frequency vacuum modes. To make these expressions mathematically well-defined, a high-frequency cutoff function $f(k)$, where $k = |\mathbf{k}|$, is introduced to suppress contributions from large wavevectors. Physically, this reflects the fact that real materials cannot reflect arbitrarily high-frequency radiation: the conduction electrons responsible for reflectivity have finite mass and response time, and cannot follow field oscillations beyond a certain threshold. At asymptotically high frequencies ($\omega_k \to \infty$), materials become effectively transparent, and the electromagnetic modes behave as though no boundary were present.

The cutoff function $f(k) \to 0$ as $k \to \infty$, and suppresses these unphysical contributions. Thus, it serves as a proxy for the finite-frequency response of real materials. In more complete treatments, this behavior is incorporated explicitly through a complex, frequency-dependent dielectric function $\varepsilon(\omega)$. From a computational perspective though, $f(k)$ is often just a formal trick to regulate divergent sums.

Importantly, the cutoff function does not appear in the final physical answer. It cancels out when computing differences in vacuum energies — such as the energy

between configurations with and without boundaries — because high-frequency modes are unaffected by the presence of the surfaces and contribute equally in both cases. Thus, while $f(k)$ is crucial to intermediate steps in the derivation, it ultimately drops out, leaving a finite and physically meaningful Casimir energy.

After subtracting the offset corresponding to the zero-point energy in the free space, the difference in energy becomes

$$\begin{aligned}\Delta E_0(a) &= \frac{1}{4\pi}\hbar c A \int_0^\infty k_\perp dk_\perp \Big[\sum_{n=-\infty}^{\infty} \sqrt{k_\perp^2 + (\frac{\pi n}{a})^2}\ f(k) \\ &\quad - \frac{a}{\pi}\int_{-\infty}^{\infty} dk_z \sqrt{k_\perp^2 + k_z^2}\ f(\sqrt{k_\perp^2 + k_z^2})\Big] \\ &= \frac{\pi^2 \hbar c A}{4a^3}\Big[h(0)/2 + \sum_{n=1}^{\infty} h(n) - \int_0^\infty dz\, h(z)\Big], \end{aligned} \tag{1.4}$$

where

$$h(z) \equiv \int_0^\infty d\rho \sqrt{\rho + z^2} f(\pi\sqrt{\rho + z^2}/a) = 2\int_{|z|}^\infty dt\, t^2 f(\pi t/a), \tag{1.5}$$

with the change of variables as $\rho \equiv (ak_\perp/\pi)^2$ and $z \equiv ak_z/\pi$. To extract a meaningful finite result, one standard technique is to apply the Euler–Maclaurin summation formula, which relates sums to integrals through correction terms involving higher derivatives of the summand. A truncated approximation up to the third derivative is given by

$$h(0)/2 + \sum_{n=1}^{\infty} h(n) \approx \int_0^\infty dz\, h(z) - \frac{h'(0)}{12} + \frac{h'''(0)}{720}. \tag{1.6}$$

By Eq. (1.5), for $z \geq 0$, $g'(z)$ vanishes at $z = 0$. The third derivative therefore dominates the energy difference and yields

$$\Delta E_0(a) = -\frac{\pi^2 \hbar c A}{720 a^3}. \tag{1.7}$$

The Casimir pressure between two conducting plates is thus

$$P_0 = \partial_a \Delta E_0 / A = -\frac{\pi^2 \hbar c}{240 a^4}, \tag{1.8}$$

which is the Casimir force per unit area from Eq. (1.1). The pressure is negative, indicating that the force between the plates is attractive. Notably, the result is universal — it does not depend on any material parameter such as charge, mass, or coupling strength. This universality emerges from the fact that, in the idealized limit of perfect conductors, the only relevant scale in the problem is the plate separation itself. While this derivation is based on a highly symmetric geometry and idealized boundary conditions, it sets the foundation for understanding Casimir forces in more realistic configurations.

1.2.1 Lifshitz Theory for Dielectric Half-Spaces

The original Casimir effect based on idealized configurations revealed the physical significance of zero-point energy, but real materials are not perfect reflectors, and real interfaces are seldom idealized planes. To address this limitation, the theory was extended by Lifshitz in 1956 [7] to account for frequency-dependent dielectric response, finite temperature, and continuous media.

Lifshitz's formalism marks a significant generalization of Casimir's result, replacing mode summation with a fluctuation-electrodynamic treatment grounded in

the principles of statistical physics and linear response theory. In contrast to idealized boundary conditions, Lifshitz theory incorporates material-specific response through their complex, frequency-dependent dielectric functions. It provides a framework for calculating dispersion forces — commonly known as van der Waals and Casimir forces—between planar dielectric half-spaces by evaluating the stress tensor in the intervening vacuum, sourced by fluctuating polarization currents in the surrounding media.

Subsequent developments by Dzyaloshinskii and Pitaevskii [8] refined the formalism using Green's function methods and fluctuation-dissipation theorems, making the theory amenable to both analytic and numerical analysis. Beyond its foundational importance, Lifshitz theory is indispensable in applications ranging from nanomechanics to precision metrology. Experimental verifications of Casimir forces between real materials invariably require this framework, especially when dielectric contrast, temperature dependence, or material absorption are non-negligible. As such, the Lifshitz formalism provides the essential starting point for any rigorous study of Casimir forces in realistic settings.

We consider two semi-infinite, planar, non-magnetic dielectrics with permittivities $\varepsilon_1(\omega)$ and $\varepsilon_2(\omega)$, separated by a vacuum gap of width d. At zero temperature, the Casimir pressure arises from the modification of the electromagnetic zero-point fluctuations due to reflection at the interfaces.

After Wick rotation to imaginary frequency $\omega \to i\xi$, the field in the vacuum gap is decomposed into transverse-electric (TE) and transverse-magnetic (TM) plane-wave modes with in-plane wavevector $\mathbf{k}_\perp$. Define the decay constants

$$\kappa_0 = \sqrt{k_\perp^2 + \xi^2/c^2}, \qquad \kappa_a = \sqrt{k_\perp^2 + \varepsilon_a(i\xi)\,\xi^2/c^2}, \quad (a = 1, 2). \tag{1.9}$$

The Fresnel reflection coefficients for vacuum–medium a interfaces on the imaginary axis are

$$r_a^{\mathrm{TM}}(i\xi, k_\perp) = \frac{\varepsilon_a(i\xi)\,\kappa_0 - \kappa_a}{\varepsilon_a(i\xi)\,\kappa_0 + \kappa_a}, \qquad r_a^{\mathrm{TE}}(i\xi, k_\perp) = \frac{\kappa_0 - \kappa_a}{\kappa_0 + \kappa_a}. \tag{1.10}$$

The free energy per unit area is then

$$\mathcal{F}(d) = \frac{\hbar}{2\pi}\int_0^\infty d\xi \int \frac{d^2\mathbf{k}_\perp}{(2\pi)^2} \sum_{p=\mathrm{TE,TM}} \log\Big[1 - r_1^{(p)}(i\xi, k_\perp)\, r_2^{(p)}(i\xi, k_\perp)\, e^{-2\kappa_0 d}\Big]. \tag{1.11}$$

Differentiating with respect to d gives the pressure,

$$P(d) = -\frac{\partial \mathcal{F}}{\partial d} = -\frac{\hbar}{\pi}\int_0^\infty d\xi \int_0^\infty \frac{k_\perp\, dk_\perp}{2\pi} \sum_{p=\mathrm{TE,TM}} \frac{\kappa_0\, r_1^{(p)} r_2^{(p)}\, e^{-2\kappa_0 d}}{1 - r_1^{(p)} r_2^{(p)}\, e^{-2\kappa_0 d}}. \tag{1.12}$$

This is the standard zero-temperature Lifshitz formula for the Casimir pressure between two parallel dielectric half-spaces separated by vacuum — a significant step forward in describing interactions between real materials.

1.3 Quantum Electrodynamics with Magnetodielectric Media

Quantum electrodynamics (QED) in linear media extends the formalism of free-space QED to systems in which the electromagnetic field interacts with material bodies characterized by spatially and frequency-dependent dielectric permittivity $\varepsilon(\mathbf{r}, \omega)$ and magnetic permeability $\mu(\mathbf{r}, \omega)$. These properties modify the quantization of the field and determine the structure of vacuum fluctuations, which are central to Casimir and Casimir–Polder interactions.

1.3.1 Green Tensors in Linear Media

The starting point is Maxwell's equations in the presence of linear media. In the frequency domain, assuming a time dependence $\sim e^{-i\omega t}$, the source-modified Maxwell equations for time-harmonic fields $\mathbf{E}(\mathbf{r},\omega)$ and $\mathbf{B}(\mathbf{r},\omega)$ read:

$$\nabla \cdot \mathbf{D}(\mathbf{r},\omega) = 0, \tag{1.13}$$

$$\nabla \cdot \mathbf{B}(\mathbf{r},\omega) = 0, \tag{1.14}$$

$$\nabla \times \mathbf{E}(\mathbf{r},\omega) = i\omega \mathbf{B}(\mathbf{r},\omega), \tag{1.15}$$

$$\nabla \times \mathbf{H}(\mathbf{r},\omega) = -i\omega \mathbf{D}(\mathbf{r},\omega) + \mathbf{J}_{\text{ext}}(\mathbf{r},\omega), \tag{1.16}$$

with constitutive relations for isotropic, homogeneous linear media:

$$\mathbf{D}(\mathbf{r},\omega) = \varepsilon_0 \varepsilon(\mathbf{r},\omega)\mathbf{E}(\mathbf{r},\omega), \quad \mathbf{B}(\mathbf{r},\omega) = \mu_0 \mu(\mathbf{r},\omega)\mathbf{H}(\mathbf{r},\omega). \tag{1.17}$$

Combining Eqs. (1.15) and (1.16) leads to the inhomogeneous vector Helmholtz equation for the electric field:

$$\nabla \times \mu^{-1}(\mathbf{r},\omega)\nabla \times \mathbf{E}(\mathbf{r},\omega) - \frac{\omega^2}{c^2}\varepsilon(\mathbf{r},\omega)\mathbf{E}(\mathbf{r},\omega) = i\omega\mu_0 \mathbf{J}_{\text{ext}}(\mathbf{r},\omega). \tag{1.18}$$

The solution to this equation is expressed in terms of the dyadic electromagnetic Green tensor $\mathbf{G}(\mathbf{r},\mathbf{r}',\omega)$, defined as the response function satisfying:

$$\left[\nabla \times \mu^{-1}(\mathbf{r},\omega)\nabla \times -\frac{\omega^2}{c^2}\varepsilon(\mathbf{r},\omega)\right]\mathbf{G}(\mathbf{r},\mathbf{r}',\omega) = \delta(\mathbf{r}-\mathbf{r}')\mathbf{I}. \tag{1.19}$$

This Green tensor encodes how a point dipole source at position $\mathbf{r}'$ generates an electric field at $\mathbf{r}$, incorporating the full influence of material boundaries and dispersion.

Given an external current distribution $\mathbf{J}_{\text{ext}}(\mathbf{r}, \omega)$, the electric field is obtained by convolution:

$$\mathbf{E}(\mathbf{r}, \omega) = i\omega\mu_0 \int d^3\mathbf{r}' \, \mathbf{G}(\mathbf{r}, \mathbf{r}', \omega) \cdot \mathbf{J}_{\text{ext}}(\mathbf{r}', \omega). \tag{1.20}$$

In quantum electrodynamics with media, the Green tensor also governs the spectral and spatial structure of field fluctuations. In particular, linear response theory relates the field commutator to the imaginary part of the Green tensor. At zero temperature, the vacuum expectation value of the electric field commutator is given by the fluctuation-dissipation theorem:

$$\langle [\hat{E}_i(\mathbf{x}, t), \hat{E}_j(\mathbf{x}', t')] \rangle = \frac{\hbar}{\pi} \int_{-\infty}^{\infty} d\omega \, \text{Im}[G_{ij}(\mathbf{x}, \mathbf{x}', \omega)] \exp[-i\omega(t - t')]. \tag{1.21}$$

This relation will serve as the cornerstone for computing Casimir–Polder shifts in the subsequent analysis.

1.4 Atom Interacting with a Planar Surface

The Casimir–Polder effect predicts that a ground-state atom near a conducting surface is attracted to the surface due to the local modification of the field modes in the vacuum state. The interaction between an atom and the quantized electromagnetic field is central to understanding a wide range of physical phenomena, including spontaneous emission, van der Waals and Casimir–Polder forces, and radiative energy shifts. At the microscopic level, the interaction between an atom and the quantized electromagnetic field originates from the minimal coupling prescription

in the Coulomb gauge, where the vector potential $\hat{\mathbf{A}}(\hat{\mathbf{r}}, t)$ satisfies the transversality condition $\nabla \cdot \hat{\mathbf{A}} = 0$. For a single electron bound in an external potential $V(\hat{\mathbf{r}})$, the Hamiltonian takes the form

$$\hat{H} = \frac{1}{2m}\left[\hat{\mathbf{p}} + e\hat{\mathbf{A}}(\hat{\mathbf{r}}, t)\right]^2 + V(\hat{\mathbf{r}}), \tag{1.22}$$

where $\hat{\mathbf{p}} = -i\hbar\nabla$ is the canonical momentum operator and e is the electron charge.

Expanding the square yields three distinct contributions:

$$\hat{H} = \frac{\hat{\mathbf{p}}^2}{2m} + \frac{e}{2m}\left(\hat{\mathbf{p}} \cdot \hat{\mathbf{A}} + \hat{\mathbf{A}} \cdot \hat{\mathbf{p}}\right) + \frac{e^2}{2m}\hat{\mathbf{A}}^2 + V(\hat{\mathbf{r}}). \tag{1.23}$$

The first term describes the kinetic energy of the bound electron. The second term represents the interaction between the particle and the quantized electromagnetic field and gives rise, via second-order perturbation theory, to spontaneous emission, van der Waals and Casimir–Polder forces. The third term contributes to radiative corrections such as the Lamb shift, though in simplified treatments it is often absorbed into renormalized parameters or neglected in the dipole approximation.

In general, $\hat{\mathbf{p}}$ and $\hat{\mathbf{A}}(\hat{\mathbf{r}}, t)$ do not commute

$$[\hat{p}_i, \hat{A}_j(\hat{\mathbf{r}})] = -i\hbar\,\partial_i \hat{A}_j(\hat{\mathbf{r}}) \neq 0, \tag{1.24}$$

so the linear coupling term must be symmetrized to ensure Hermiticity. However, in the electric-dipole approximation, which assumes that the field varies negligibly over the extent of the atom, one approximates $\hat{\mathbf{A}}(\hat{\mathbf{r}}, t) \approx \hat{\mathbf{A}}(\mathbf{r}_N, t)$, where $\mathbf{r}_N$ is the nuclear position. Under this assumption, $\hat{\mathbf{A}}$ becomes a constant operator with respect to $\hat{\mathbf{r}}$, and thus commutes with $\hat{\mathbf{p}}$, allowing the minimal-coupling interaction to be written

simply as

$$\hat{H}_{\text{int}} = \frac{e}{m}\hat{\mathbf{p}} \cdot \hat{\mathbf{A}}. \tag{1.25}$$

While Eq. (1.22) is exact, it is often more convenient to perform a unitary transformation to the multipolar gauge, in which the field couples directly to the atomic multipole moments. This transformation is achieved using the Power–Zienau–Woolley (PZW) unitary operator:

$$\hat{U}_{\text{PZW}} = \exp\left[-\frac{i}{\hbar}\sum_j e_j \hat{\mathbf{r}}_j \cdot \hat{\mathbf{A}}(\hat{\mathbf{R}})\right], \tag{1.26}$$

where $\hat{\mathbf{R}}$ is the center-of-mass coordinate of the atom, and the sum is over charged constituents j (for simplicity, we focus on a single electron with charge $-e$ and position $\hat{\mathbf{r}}$).

To leading order in the multipole expansion of the atom–field coupling, the interaction energy reduces to that between the atomic electric dipole moment and the electric field evaluated at the position of the atom:

$$\hat{H}_{\text{int}} = -\hat{\mathbf{d}} \cdot \hat{\mathbf{E}}(\mathbf{r}_A), \tag{1.27}$$

where $\hat{\mathbf{d}} = -e\hat{\mathbf{r}}$ is the electric dipole moment operator of the atom, and $\hat{\mathbf{E}}(\mathbf{r}_A)$ is the quantized electric field operator at the atomic center-of-mass position $\mathbf{r}_A$.

This derivation rests on the dipole approximation, which assumes that the wavelength of the electromagnetic field is much larger than the spatial extent of the atom. As a result, the spatial dependence of $\hat{\mathbf{A}}(\hat{\mathbf{r}})$ is neglected over the volume of the atom and approximated by its value at the center-of-mass coordinate $\hat{\mathbf{R}}$. This form

is especially useful in time-dependent perturbation theory and is the starting point for analyzing spontaneous emission, energy shifts, and fluctuation-induced forces.

Given the interaction Hamiltonian, the energy shift of the ground state can be calculated with second-order perturbation theory

$$V_{\mathrm{CP}} = -\sum_{j}\sum_{k,\zeta} \frac{|\langle g|\mathbf{d}|e_j\rangle \cdot \langle 0|\mathbf{E}|1_{k,\zeta}\rangle|^2}{\hbar(\omega_{j0}+\omega_k)}, \tag{1.28}$$

where $\omega_{j0} = (E_j - E_0)/\hbar$ is the transition frequency between the excited and ground states of the atom, and ω_k is the energy of the mode $(\mathbf{k}, \zeta)$ labelled by the wave vector k and the polarization index ζ. The field matrix element $\langle 0|\hat{\mathbf{E}}(\mathbf{r}_A)|1_{\mathbf{k},\zeta}\rangle$ describes

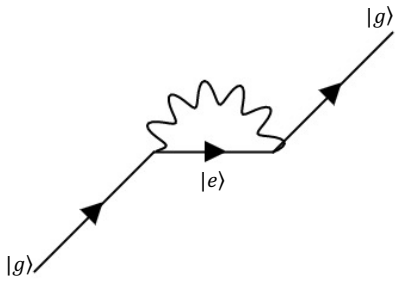

FIGURE 1.2. Feynman diagram representing a ground-state atom interacting with EM field through emission and re-absorption of virtual photons.

the electric field of a single-photon excitation in the mode $(\mathbf{k}, \zeta)$ evaluated at the atomic position $\mathbf{r}_A$, while the atomic dipole matrix element $\langle g|\hat{\mathbf{d}}|e_j\rangle$ characterizes the transition strength between the ground state $|g\rangle$ and excited state $|e_j\rangle$. This second-order expression represents the sum over virtual photon exchange processes where the atom briefly transitions to an excited state and the field to a one-photon state, followed by a return to the ground state. This process is illustrated by the diagram in Fig. 1.2.

The energy shift may be recast into a form that separates the atomic and field degrees of freedom. Defining the atomic polarizability tensor via the Kramers–Heisenberg relation,

$$\alpha_{ik}(\omega) = \frac{2}{\hbar} \sum_j \frac{\omega_{j0} \langle g|\hat{d}_i|e_j\rangle \langle e_j|\hat{d}_k|g\rangle}{\omega_{j0}^2 - \omega^2}, \tag{1.29}$$

we may write the energy shift as an integral over the vacuum field correlation function evaluated at the position of the atom. The zero-point electric field fluctuations in the presence of a dielectric medium are characterized by the symmetrized two-point function as given by the fluctuation–dissipation theorem in Eq. (1.21).

Substituting the polarizability and the time-ordered field correlator into the perturbative expression, the Casimir–Polder potential appears as an integral over real frequencies. To render the expression suitable for both analytic continuation and numerical evaluation, the frequency integral is rotated to the imaginary axis via a Wick rotation $\omega \to i\xi$. This contour deformation is justified by the analytic properties of the Green tensor and polarizability as causal response functions. Eventually, the Casimir–Polder potential takes the widely used form

$$V_{\mathrm{CP}}(\mathbf{r}_A) = -\frac{\hbar}{2\pi} \int_0^\infty d\xi \, \alpha_{ij}(i\xi) \, G_{ij}(\mathbf{r}_A, \mathbf{r}_A; i\xi), \tag{1.30}$$

where the integration is over imaginary frequencies and repeated indices are summed. The Green tensor characterizes the medium-modified vacuum fluctuations of the electric field, while the atomic polarizability encapsulates the atom's internal response to those fluctuations.

Although this compact result arises from a formulation in which both the atom and the electromagnetic field are quantized, the final expression for the energy shift

does not depend explicitly on the details of how the field is quantized. This is particularly important, as the quantization of electromagnetic fields in dissipative or absorbing media is technically challenging. The simplification here lies in the fact that the result only requires knowledge of the classical electromagnetic response functions — namely, the dielectric and magnetic susceptibilities — through the Green tensor. Equally noteworthy is that this expression emerges from a linear, dipole-type interaction Hamiltonian, and thus only captures lowest-order (linear) response between the atom and field. Nevertheless, it provides a powerful and general framework for computing dispersion interactions in complicated environments.

In addition to calculating the interaction of atoms with macroscopic bodies, the Green tensor formalism can also be used for calculating Casimir–Polder potential between two polarizable atoms in vacuum. This case will be discussed in detail in **Chapter IV**.

1.5 An Overview of Experiments

1.5.1 Experimental Confirmation and Technological Advancements

The experimental confirmation of the Casimir effect, originally predicted by Hendrik Casimir in 1948, has evolved into a cornerstone of modern precision measurement and quantum vacuum physics. Initial attempts to detect Casimir forces faced formidable challenges due to the minuscule scale of the interaction, which becomes significant only at submicron separations. Nonetheless, rapid advances in experimental control, materials fabrication, and surface metrology by the late 20th century paved the way for high-precision measurements, culminating in a series of landmark experiments that established the Casimir effect as a real and measurable consequence of quantum electrodynamics.

A pivotal breakthrough occurred in 1997, when Lamoreaux performed the first quantitative measurement of the Casimir force between macroscopic bodies [2]. In this experiment, a torsion pendulum apparatus was used to measure the attractive force between a gold-coated spherical lens and a parallel gold-coated flat plate. The sphere-plate configuration approximates the parallel-plate geometry while avoiding the problem of maintaining strict parallelism. Electrostatic calibrations were carried out by applying known voltages between the surfaces to isolate and subtract Coulomb contributions. The measured force was found to be in agreement with theoretical predictions, including corrections for finite conductivity and surface roughness, within approximately 5%. This work marked the first unambiguous confirmation of the Casimir effect in a macroscopic setup and validated the foundational predictions of Casimir's original theory in a real experimental context.

Building upon this success, Mohideen and Roy introduced a new methodology in 1998 based on atomic force microscopy (AFM) [9]. Their experiment used a much smaller polystyrene sphere (radius ~ 100 μm) coated with a thin layer of gold, attached to an AFM cantilever interacting with a planar gold-coated surface. This setup allowed for direct force curve measurements with sub-pico-Newton sensitivity and nanometer spatial resolution, particularly in the critical 100–500 nm separation range. Interferometric techniques were employed to accurately determine the sphere-plate separation, and electrostatic calibrations ensured that residual potentials did not contaminate the measurements. Their results showed excellent agreement with theoretical predictions incorporating finite conductivity corrections. Notably, this experiment was the first to resolve the Casimir force in the deep submicron regime with high precision, establishing AFM-based force measurements as the standard tool for Casimir metrology.

A third major milestone came in 2001, when Chan, Aksyuk, Kleiman, Bishop, and Capasso demonstrated the influence of Casimir forces in microelectromechanical systems (MEMS) [10]. Their experiment featured a microfabricated gold-coated cantilever suspended above a stationary gold-coated substrate, forming a nearly parallel-plate geometry with gap distances ranging from hundreds of nanometers to below 100 nanometers. As the separation decreased, the Casimir attraction eventually overwhelmed the mechanical restoring force of the cantilever, inducing a "pull-in" instability where the beam snapped into contact with the substrate. By comparing the critical pull-in distance with theoretical models incorporating the measured optical response of the gold coatings, they verified the magnitude and distance dependence of the Casimir force in a microstructured system. This experiment not only provided another precise confirmation of Casimir theory but also highlighted the importance of quantum vacuum forces in the engineering of nanoscale devices, ushering in the field of Casimir-aware MEMS design.

Aside from a quantum vacuum phenomena, an intriguing classical analogue of the Casimir effect emerges in the context of acoustic wave phenomena, where fluctuating quantum fields are replaced by externally generated classical noise. In this so-called acoustic Casimir effect, two bodies immersed in a fluid or gas experience an effective force due to the suppression of acoustic modes between them relative to the ambient field outside. Unlike conventional Casimir forces — which originate from quantum vacuum or thermal fluctuations—the acoustic Casimir effect is driven by engineered noise fields with tunable spectral properties. When the acoustic field exhibits a flat (white) frequency spectrum, the induced force between plates is typically attractive and monotonic with respect to separation, closely mirroring the behavior of quantum Casimir forces. However, if the noise spectrum is frequency-dependent,

non-monotonic and even repulsive forces can arise. The effect was experimentally demonstrated by Larraza and Denardo in 1998 [11], who observed tunable acoustic-induced forces between parallel plates subjected to controlled band-limited noise, providing a macroscopic, classical platform to explore Casimir-like physics in a regime entirely decoupled from quantum field fluctuations.

These foundational experiments collectively transformed the Casimir effect from a theoretical curiosity into an experimentally verified and technologically relevant phenomenon. They established the feasibility of measuring vacuum-induced forces with pico-Newton precision, and spurred further investigations into temperature dependence, material-specific effects and nontrivial geometries. The legacy of these experiments continues to influence modern research at the intersection of quantum field theory, materials science, and precision measurement, solidifying the Casimir effect as a crucial phenomenon in both fundamental physics and applied nanotechnology.

1.5.2 Searches for BSM Physics and Modifications of Gravity

Beyond metrology, precision measurements of Casimir forces have gained increasing prominence in the context of probing new physics beyond the Standard Model (BSM) and testing possible deviations from Newtonian gravity at sub-micron scales.

The principal reason why Casimir experiments are relevant for fundamental physics searches lies in the strength and range of the Casimir force: at separations below a few microns, it dominates over the gravitational interaction between laboratory-scale test bodies by many orders of magnitude. Consequently, the Casimir background must be carefully modeled and subtracted in any attempt to isolate

weaker hypothetical interactions, but also provides a well-understood quantum phenomenon that can be leveraged to place constraints on new forces.

In many theoretical scenarios, such hypothetical interactions are mediated by light scalar or vector bosons, leading to Yukawa-type modifications of the Newtonian gravitational potential:

$$V(r) = -\frac{G_N m_1 m_2}{r}\left(1 + \alpha e^{-r/\lambda}\right), \tag{1.31}$$

where α represents the strength of the new interaction relative to gravity, and $\lambda = \hbar/(mc)$ sets the force range, determined by the inverse mass m of the hypothetical mediator. Such interactions naturally arise in theories involving dilatons, moduli fields from string compactifications, axion-like particles, chameleon fields, or Kaluza-Klein gravitons in models with large extra dimensions.

Experimental efforts to probe these effects in the context of Casimir physics generally follow two complementary approaches. The first involves precise measurements of Casimir forces in well-defined geometries, typically between metallic or dielectric plates or spheres, and comparison with theoretical predictions based on Lifshitz theory or scattering formalisms. Any deviation between theory and experiment may signal new physics, provided systematic uncertainties such as surface roughness, finite conductivity, patch potentials, and thermal corrections are well controlled.

A notable example is the series of torsion pendulum experiments conducted by Decca et al., in which the Casimir force between a metallic plate and a gold-coated sphere was measured with sub-pico-Newton sensitivity. By achieving agreement with theoretical predictions at the level of 1% or better in the $0.2 \sim 1$ μm range, these

experiments were able to place stringent bounds on Yukawa-type forces with $\alpha \sim 10^2$ and $\lambda \sim 0.5$ μm, ruling out wide classes of BSM scenarios [12, 13].

The second approach, often termed the isoelectronic or Casimir-less technique, aims to null out the standard Casimir background by clever material design. In these experiments, test masses are fabricated such that the Casimir forces from different regions cancel out due to identical electronic properties (e.g., gold versus germanium layers with similar optical response), while the hypothetical new interaction remains sensitive to differences in mass density. The INFN Padova group pioneered such experiments, achieving differential force sensitivity at the femto-Newton level. These null experiments provide especially clean constraints on composition-dependent or density-coupled exotic forces [14].

Theoretical modeling of new interactions in this context typically assumes that the additional force is additive over the bulk volumes of the test bodies. Thus, the total hypothetical signal is computed by integrating the Yukawa potential over the geometry of interest, taking into account the densities and geometrical configuration. The resulting constraints on α and λ are typically plotted in a two-dimensional exclusion plot, with Casimir-based experiments providing some of the strongest bounds in the range $\lambda \sim 10$ nm to $\lambda \sim 10$ μm.

Beyond Yukawa-type modifications, Casimir experiments have also been employed to probe models involving environmentally sensitive scalar fields, non-Newtonian power-law potentials, axion-mediated dipole forces and axion dark matter [15, 16, 17, 18]. While Casimir experiments are not directly sensitive to spin-dependent interactions, they remain among the most effective probes of scalar-mediated, composition-dependent fifth forces in the mesoscopic regime.

In summary, the Casimir effect has transcended its role as a canonical prediction of quantum electrodynamics to become a sensitive tool in the search for new forces and modifications of gravity. Through a combination of theoretical precision and experimental ingenuity, Casimir-based setups continue to refine the landscape of allowable BSM interactions, providing a unique window into potential new physics at the micron and submicron frontier.

1.6 An Overview of Computational Methods

Modern applications increasingly demand exact or systematically improvable methods. We introduce here the proximity force approximation as a simple but crude method and the scattering formalism as the general-purpose method so far. These computational methods motivate the development of the path-integral-based worldline formalism.

1.6.1 Proximity Force Approximation

The Proximity Force Approximation (PFA) is one of the most widely used computational tools for estimating Casimir forces between curved surfaces. Originally developed in the context of van der Waals forces and surface adhesion, it has since become an essential approximation technique for Casimir interactions, particularly in experimental configurations where non-planar geometries are involved. The core idea behind PFA is to approximate the Casimir energy (or force) between gently curved objects by summing over infinitesimal contributions from locally parallel surface elements, assuming each local region behaves like a pair of parallel plates separated by a local distance.

For a sphere of radius R near a flat plate at closest separation $a \ll R$, the PFA yields an approximate expression for the Casimir energy by integrating the energy per unit area between parallel plates over the curved surface of the sphere:

$$E_{\mathrm{PFA}}(a) = 2\pi R \int_a^\infty dz\, \mathcal{E}_\parallel(z), \tag{1.32}$$

where $\mathcal{E}_\parallel(z)$ is the Casimir energy density per unit area between two parallel plates separated by distance z. For perfect conductors at zero temperature,

$$\mathcal{E}_\parallel(z) = -\frac{\pi^2 \hbar c}{720 z^3}, \tag{1.33}$$

leading to the standard PFA result:

$$E_{\mathrm{PFA}}(a) = -\frac{\pi^3 \hbar c R}{360 a^2}, \quad F_{\mathrm{PFA}}(a) = -\frac{\pi^3 \hbar c R}{120 a^3}. \tag{1.34}$$

This expression is widely used in interpreting experimental data, especially in sphere-plane and cylinder-plane geometries, where exact solutions are not easily tractable.

Despite its practical utility, the PFA is not a systematically controlled approximation. It lacks a small parameter expansion in a rigorous sense. Its validity rests on the assumption that the radius of curvature R of the surfaces is much larger than the minimal separation a:

$$\frac{a}{R} \ll 1. \tag{1.35}$$

Under this condition, the local curvature changes slowly compared to the decay length of the Casimir interaction, justifying the assumption of near-planarity. However, the PFA does not correctly capture diffraction, retardation, or multiple-scattering effects that become important when a/R increases. Corrections beyond PFA are nontrivial

and have been actively studied through both analytical expansions and numerical methods such as the scattering formalism.

Moreover, the PFA does not account for non-additivity of Casimir interactions — the fact that the total Casimir energy of a system is not simply the sum of pairwise interactions. This becomes especially important in many-body configurations or in the presence of structured materials such as photonic crystals or metasurfaces.

The PFA is widely used in analyzing Casimir force measurements involving sphere-plate geometries, such as in the high-precision experiments of Lamoreaux [2] and Mohideen and Roy [9]. In these setups, a metallic sphere is brought close to a flat metallic surface, and the resulting force is measured using torsional balances or atomic force microscopy. The PFA provides a practical means of comparing experimental data with theoretical predictions, especially when the surface separation remains small.

However, to achieve quantitative agreement at the few-percent level or better, experiments must incorporate corrections beyond PFA, including those due to surface roughness, finite conductivity, temperature, and geometry-induced deviations. Theoretical work has provided gradient expansions and exact scattering-theoretic corrections that extend PFA systematically [19, 20].

The proximity force approximation remains a central computational tool in Casimir physics, especially in interpreting experimental data in curved geometries. While limited in accuracy beyond the short-distance, large-radius regime, its simplicity and physical transparency continue to make it an essential part of the Casimir toolkit. Its limitations have also motivated the development of more robust numerical techniques, which aim to extend precision Casimir force predictions to arbitrary geometries and material properties.

1.6.2 Surface Current Scattering Formalism

As Casimir experiments and applications have progressed toward increasingly intricate geometries and material models, the demand for general, accurate, and systematically extensible computational frameworks has intensified. Among the most powerful and rigorously developed approaches is the *scattering matrix formalism* [21], which reformulates Casimir interactions in terms of the electromagnetic response of objects via their individual scattering matrices. This method is both conceptually clear and computationally robust, enabling the calculation of Casimir forces between bodies of arbitrary shape, material composition, and spatial arrangement.

The central idea of the scattering formalism is that the Casimir energy arises from multiple reflections of virtual photons between distinct bodies. Each object is characterized by a T-matrix (or reflection matrix), which encodes how incident electromagnetic multipole fields are scattered into outgoing ones. The interaction between objects is governed by translation matrices, which relate the multipole expansions centered on different bodies.

The finite-temperature Casimir free energy between two compact bodies, labeled 1 and 2, is given by a Matsubara frequency sum:

$$\mathcal{F}(a) = k_B T \sum_{n=0}^{\infty}{}' \log\det\left[\mathbf{I} - \mathbb{T}_1(i\xi_n)\mathbb{U}_{12}(i\xi_n)\mathbb{T}_2(i\xi_n)\mathbb{U}_{21}(i\xi_n)\right], \tag{1.36}$$

where $\xi_n = 2\pi n k_B T/\hbar$ are the Matsubara frequencies, $\mathbb{T}_i(i\xi_n)$ are the T-matrices of the objects evaluated at imaginary frequencies, and $\mathbb{U}_{ij}(i\xi_n)$ are the translation operators mapping fields from one object to the coordinate frame of the other. The

prime on the sum indicates that the $n = 0$ term carries half-weight:

$$\sum_{n=0}^{\infty}{}' f(\xi_n) = \tfrac{1}{2} f(\xi_0) + \sum_{n=1}^{\infty} f(\xi_n). \tag{1.37}$$

This formulation can be rigorously derived from a functional integral over the electromagnetic field, constrained by boundary conditions enforced through auxiliary surface currents $\mathbf{J}(\mathbf{r})$ on each object. Integrating out the field yields an effective action coupling the induced currents via the vacuum Green tensor $\mathbf{G}^{(0)}(\mathbf{r}, \mathbf{r}'; i\xi)$:

$$S_{\text{eff}}[\mathbf{J}] = \frac{1}{2} \int d^3\mathbf{r} \int d^3\mathbf{r}' \, \mathbf{J}(\mathbf{r}) \cdot \mathbf{G}^{(0)}(\mathbf{r}, \mathbf{r}'; i\xi) \cdot \mathbf{J}(\mathbf{r}'). \tag{1.38}$$

This makes manifest that the Casimir interaction results from quantum correlations between fluctuating surface currents.

For numerical evaluation, the surface currents are expanded in a suitable vector basis, such as vector spherical harmonics (for spheres), cylindrical modes (for rods), or plane-wave modes (for planar objects). The T-matrix encapsulates the object's response in this basis, while the translation matrices handle the coupling between distinct coordinate systems. The determinant in Eq. (1.36) compactly encodes the entire multiple-scattering series, and generalizes naturally to more than two bodies through an expansion in irreducible many-body scattering amplitudes.

This scattering formalism has enabled exact numerical calculations in a wide variety of settings: sphere-plane, sphere-sphere, cylinder-cylinder, sphere-grating, and more. Its strength lies in its ability to incorporate material dispersion, anisotropy, and temperature, all within a unified matrix-based framework. It continues to serve as a cornerstone of modern theoretical and computational Casimir physics.

While the scattering matrix formalism is highly successful, the computational cost can grow rapidly with the number of scattering channels required for convergence, especially in many-body or non-spherical systems. In contrast, the worldline path-integral method offers a complementary approach that is basis-independent, parallelizable, more intuitive, and can efficiently capture Casimir interactions via stochastic sampling of fluctuating paths, naturally accommodating arbitrary geometries. Thus, the worldline formalism fills a crucial gap in Casimir computations where traditional operator-based methods become intractable.

CHAPTER II

ELECTROMAGNETIC WORLDLINE FORMALISM

2.1 Introduction

The previous chapter presents two primary approaches to calculating atom–surface Casimir interactions: explicit mode summation — typically assuming perfectly conducting boundaries — and the more general QED Green tensor formalism, which accommodates dielectric response. While both methods are analytically powerful in highly symmetric geometries, they become intractable when the surfaces involved lack symmetry or involve arbitrary spatial profiles. This motivates the development of alternative techniques that are more amenable to numerical implementation in general geometries.

In this chapter, we introduce the worldline path integral method — a powerful approach for computing Casimir energies and forces that extends naturally to a wide range of geometries, including macroscopic bodies. Originally developed for scalar fields in quantum field theory [22, 23], the method provides both a conceptual and computational foundation for more complete electromagnetic treatments. While scalar models omit the full vector structure of electromagnetism, they remain physically meaningful in many contexts, such as scalar decompositions in symmetric settings, and serve as a practical starting point for worldline-based techniques.

The worldline approach reformulates the Casimir energy as a path integral over ensembles of fluctuating field configurations, which can be interpreted as closed particle worldlines in Euclidean spacetime. This path integral is evaluated using stochastic sampling — effectively a Monte Carlo method over Brownian trajectories.

Unlike mode summation or Green-function-based methods, which require solving field equations for each geometry, the worldline method encodes geometry implicitly via the interaction of these worldlines with the background bodies. In the sections that follow, we develop this framework in electromagnetism, with particular attention to its numerical realization and to the connection between worldline averages and physically observable quantities such as Casimir forces.

2.2 Path Integrals

The path integral approach to quantum mechanics [24, 25] provides an alternative to the operator-based formulation by expressing quantum amplitudes as a sum over all possible trajectories weighted by an action-dependent phase. This formulation offers deep insight into quantum fluctuations and serves as the foundation for modern approaches to quantum field theory and semiclassical approximations.

2.2.1 Propagators in Quantum Mechanics

Consider a non-relativistic particle of mass m moving in one dimension under a potential $V(x)$. The transition amplitude for the particle to move from position x_i at time t_i to x_f at time t_f is given by the kernel:

$$K(x_f, t_f; x_i, t_i) = \langle x_f | e^{-i\hat{H}(t_f - t_i)/\hbar} | x_i \rangle, \tag{2.1}$$

where the Hamiltonian operator is $\hat{H} = \hat{T} + \hat{V} = \frac{\hat{p}^2}{2m} + V(\hat{x})$.

To evaluate this, we partition the time interval into N equal slices of step size $\epsilon = (t_f - t_i)/N$, and insert complete sets of position eigenstates at each intermediate

time:

$$K(x_f, t_f; x_i, t_i) = \lim_{N\to\infty} \left(\frac{m}{2\pi i\hbar\epsilon}\right)^{N/2} \int \prod_{j=1}^{N-1} dx_j \prod_{j=0}^{N-1} \langle x_{j+1}|e^{-i\epsilon\hat{H}/\hbar}|x_j\rangle \tag{2.2}$$

$$\equiv \lim_{N\to\infty} \int \mathcal{D}x \prod_{j=0}^{N-1} K_\epsilon(x_{j+1}, x_j), \tag{2.3}$$

with $x_0 = x_i$, $x_N = x_f$, and the path integral measure defined by

$$\mathcal{D}x \equiv \left(\frac{m}{2\pi i\hbar\epsilon}\right)^{N/2} \prod_{j=1}^{N-1} dx_j. \tag{2.4}$$

The short-time propagator K_ϵ is evaluated using the Trotter formula:

$$e^{-i\epsilon\hat{H}/\hbar} = e^{-i\epsilon(\hat{T}+\hat{V})/\hbar} \approx e^{-i\epsilon\hat{T}/\hbar} e^{-i\epsilon\hat{V}/\hbar} + \mathcal{O}(\epsilon^2). \tag{2.5}$$

The kinetic term is most naturally evaluated in the momentum basis. Using $\langle x|p\rangle = (2\pi\hbar)^{-1/2} e^{ipx/\hbar}$, we have:

$$\begin{aligned}\langle x_{j+1}|e^{-i\epsilon\hat{T}/\hbar}|x_j\rangle &= \int \frac{dp}{2\pi\hbar} e^{ip(x_{j+1}-x_j)/\hbar} e^{-i\epsilon p^2/2m\hbar} \\ &= \sqrt{\frac{m}{2\pi i\hbar\epsilon}} \exp\left[\frac{im}{2\hbar\epsilon}(x_{j+1}-x_j)^2\right].\end{aligned} \tag{2.6}$$

The potential term is local in position space:

$$\langle x_{j+1}|e^{-i\epsilon\hat{V}/\hbar}|x_j\rangle \approx \delta(x_{j+1}-x_j) \exp\left[-\frac{i\epsilon}{\hbar}V(x_j)\right]. \tag{2.7}$$

Combining both terms yields the short-time propagator:

$$K_\epsilon(x_{j+1}, x_j) = \sqrt{\frac{m}{2\pi i\hbar\epsilon}} \exp\left[\frac{i\epsilon}{\hbar}\left(\frac{m}{2}\left(\frac{x_{j+1}-x_j}{\epsilon}\right)^2 - V(x_j)\right)\right], \tag{2.8}$$

and the full transition amplitude becomes:

$$\begin{aligned} K(x_f, t_f; x_i, t_i) = \lim_{N\to\infty} \int \prod_{j=1}^{N-1} dx_j \left(\frac{m}{2\pi i\hbar\epsilon}\right)^{N/2} \\ \times \exp\left[\frac{i}{\hbar}\sum_{j=0}^{N-1}\epsilon\left(\frac{m}{2}\left(\frac{x_{j+1}-x_j}{\epsilon}\right)^2 - V(x_j)\right)\right]. \end{aligned} \tag{2.9}$$

In the continuum limit $\epsilon \to 0$, this becomes a path integral over all continuous paths $x(t)$ with endpoints $x(t_i) = x_i$, $x(t_f) = x_f$:

$$K(x_f, t_f; x_i, t_i) = \int_{x(t_i)=x_i}^{x(t_f)=x_f} \mathcal{D}x(t)\, \exp\left[\frac{i}{\hbar} S[x(t)]\right], \tag{2.10}$$

where the classical action is

$$S[x(t)] = \int_{t_i}^{t_f} dt \left[\frac{1}{2} m\dot{x}^2(t) - V(x(t))\right]. \tag{2.11}$$

To render the integral convergent and connect to statistical mechanics, one often performs a Wick rotation $t \to -i\tau$ to make the action become Euclidean:

$$S_E[x(\tau)] = \int_{\tau_i}^{\tau_f} d\tau \left[\frac{1}{2} m \left(\frac{dx}{d\tau}\right)^2 + V(x(\tau))\right], \tag{2.12}$$

and the propagator becomes

$$K_E(x_f, \tau_f; x_i, \tau_i) = \int \mathcal{D}x(\tau)\, \exp\left[-\frac{1}{\hbar} S_E[x(\tau)]\right]. \tag{2.13}$$

In this form, the path integral has the structure of a partition function over Brownian motion trajectories, and is foundational in the worldline representation of quantum field theory.

This formulation provides an intuitive and powerful method for analyzing quantum systems via classical paths weighted by the action. Its extension to multiple dimensions and field configurations underpins path integral approaches to quantum field theory, statistical field theory, and the numerical worldline methods used in this thesis to evaluate Casimir energies.

2.2.2 The Feynman–Kac Formula

The Feynman–Kac formula provides a fundamental bridge between stochastic processes and the solutions to a class of parabolic partial differential equations (PDEs), and plays a central role in the probabilistic formulation of quantum mechanics, statistical physics, and finance.

Consider a non-relativistic quantum particle of mass m in one dimension, governed by the Hamiltonian

$$\hat{H} = -\frac{\hbar^2}{2m}\frac{d^2}{dx^2} + V(x). \tag{2.14}$$

The propagator in imaginary time, which is the Euclidean analog of the quantum mechanical kernel, reads:

$$K_E(x_f, \tau_f; x_i, \tau_i) = \langle x_f | e^{-(\tau_f - \tau_i)\hat{H}/\hbar} | x_i \rangle. \tag{2.15}$$

In the context of statistical mechanics, this object is interpreted as the amplitude for a particle to diffuse from x_i to x_f in time $\tau_f - \tau_i$, under the influence of a potential

$V(x)$. The goal is to show that this propagator can be expressed as an ensemble average over Brownian paths weighted by the Euclidean action.

From the Feynman path integral in imaginary time (2.13), the Euclidean propagator is:

$$K_E(x_f, \tau_f; x_i, \tau_i) = \int_{x(\tau_i)=x_i}^{x(\tau_f)=x_f} \mathcal{D}x(\tau) \exp\left[-\frac{1}{\hbar}\int_{\tau_i}^{\tau_f} d\tau \left(\frac{1}{2}m\dot{x}^2(\tau) + V(x(\tau))\right)\right]. \tag{2.16}$$

This path integral resembles the probability distribution for Brownian motion with a weight factor from the potential.

To make this precise, we write the kinetic term as a Wiener measure:

$$P[x(\tau)] \sim \exp\left(-\frac{1}{\hbar}\int_{\tau_i}^{\tau_f} \frac{1}{2}m\dot{x}^2(\tau)d\tau\right), \tag{2.17}$$

which is just the Gaussian weight for Brownian motion (after rescaling time). Thus, we interpret the measure $\mathcal{D}x(\tau)$ as an average over Brownian paths:

$$K_E(x_f, \tau_f; x_i, \tau_i) = \mathbb{E}^{\mathrm{BM}}_{x_i \to x_f}\left[\exp\left(-\frac{1}{\hbar}\int_{\tau_i}^{\tau_f} V(x(\tau))\, d\tau\right)\right], \tag{2.18}$$

where the expectation $\mathbb{E}^{\mathrm{BM}}$ denotes averaging over all Brownian paths connecting x_i to x_f in time $\tau_f - \tau_i$.

Let us now define:

$$u(x, \tau) := \langle x | e^{-(T-\tau)\hat{H}/\hbar} | \psi_0 \rangle, \tag{2.19}$$

where $|\psi_0\rangle$ is some initial state and T is a fixed Euclidean time. Then $u(x, \tau)$ satisfies the Euclidean Schrödinger (or heat) equation:

$$\frac{\partial u}{\partial \tau} = \left(\frac{\hbar^2}{2m}\frac{\partial^2}{\partial x^2} - V(x)\right) u(x, \tau), \tag{2.20}$$

with final condition $u(x,T) = \psi_0(x)$. The Feynman–Kac formula now asserts:

$$u(x,\tau) = \mathbb{E}^x \left[\exp\left(-\frac{1}{\hbar} \int_\tau^T V(x(s))\, ds \right) \psi_0(x(T)) \right], \tag{2.21}$$

where $x(s)$ is a Brownian path starting at $x(\tau) = x$ and evolving under free diffusion until time T.

The Feynman–Kac formula thus provides a probabilistic representation of the solution to the heat equation with a potential. The term $\exp(-\int V)$ acts like a weight that penalizes paths passing through regions of large potential energy. This notable result offers an elegant route from quantum mechanics to stochastic processes and forms the basis of practical numerical methods for Casimir energies and effective actions in curved or bounded geometries.

2.3 Scalar Field Worldline Formulation

In the following, we develop the path-integral, or worldline, approach to computing Casimir energies in general geometries, including interactions between extended macroscopic bodies. The original formulation of this method was introduced in the context of scalar fields, which, while not representing the full electromagnetic field, provide a valuable conceptual and computational framework for introducing the technique. The method recasts the effective action of a quantum field theory in terms of a functional integral over ensembles of closed particle trajectories, enabling a numerical Monte Carlo evaluation of Casimir energies. This stochastic formulation contrasts sharply with the traditional mode summation and Green tensor approaches, and is particularly well suited for problems with nontrivial geometries where analytical methods become intractable.

2.3.1 Schwinger Proper-Time Formalism

The Schwinger proper-time formalism [26] is a powerful technique in quantum field theory that rewrites operator inverses — such as propagators or determinants arising in one-loop effective actions — into integrals over an auxiliary parameter known as the *proper time*. This method provides a unifying framework that is not only elegant but also computationally advantageous, especially in curved or bounded geometries where mode-summation techniques become intractable.

In quantum field theory, loop diagrams often lead to divergent integrals. Schwinger introduced the proper-time method in 1951 to systematically treat such divergences and calculate vacuum polarization effects in quantum electrodynamics (QED). His formulation recasts loop amplitudes as proper-time integrals, thereby exposing their mathematical structure and allowing for efficient regularization. This method also forms the basis for worldline path-integral techniques used in modern computations of Casimir energies.

Let us consider a free scalar field of mass m. The Feynman propagator in position space is the Green's function of the Klein–Gordon operator:

$$G(x,x') = \langle x|\frac{1}{-\Box + m^2 - i\epsilon}|x'\rangle. \tag{2.22}$$

Using the identity

$$\frac{1}{A} = \int_0^\infty ds\, e^{-sA}, \tag{2.23}$$

which holds for a positive-definite operator A, we may write

$$G(x,x') = \int_0^\infty ds\, \langle x|e^{-s(-\Box+m^2)}|x'\rangle. \tag{2.24}$$

The quantity inside the integrand is the heat kernel:

$$K(x,x';s) \equiv \langle x|e^{-s(-\Box+m^2)}|x'\rangle, \tag{2.25}$$

which solves the heat equation

$$\left(\frac{\partial}{\partial s} + (-\Box + m^2)\right) K(x,x';s) = 0, \quad K(x,x';0) = \delta(x-x'). \tag{2.26}$$

Thus, the scalar propagator becomes an integral over the proper time s:

$$G(x,x') = \int_0^\infty ds\, K(x,x';s). \tag{2.27}$$

For a scalar field interacting with a background potential $V(x)$, the one-loop effective action is formally:

$$\Gamma[V] = \frac{1}{2}\mathrm{Tr}\log\left(-\Box + m^2 + V(x)\right). \tag{2.28}$$

Using the identity

$$\log A = -\int_0^\infty \frac{ds}{s}\, e^{-sA}, \tag{2.29}$$

the effective action becomes:

$$\Gamma[V] = -\frac{1}{2}\int_0^\infty \frac{ds}{s}\,\mathrm{Tr}\left(e^{-s(-\Box+m^2+V(x))}\right). \tag{2.30}$$

In position space, this trace reads:

$$\Gamma[V] = -\frac{1}{2}\int_0^\infty \frac{ds}{s}\int d^dx\, K(x,x;s), \tag{2.31}$$

where $K(x, x; s)$ is the diagonal part of the heat kernel.

This representation makes divergences manifest as small-s behavior in the integrand. Various regularization schemes — such as dimensional regularization, zeta function regularization, or cutoff regularization — can be introduced at this stage.

The heat kernel $K(x, x'; s)$ admits a representation as a quantum mechanical path integral over all trajectories of fixed proper-time s:

$$K(x, x'; s) = \int_{x(0)=x'}^{x(s)=x} \mathcal{D}x(t) \, \exp\left[-\int_0^s dt \left(\frac{\dot{x}^2(t)}{4} + V(x(t))\right)\right]. \tag{2.32}$$

This expression treats the field-theoretic propagator as an average over first-quantized particle trajectories, with each path weighted by a Euclidean action. When $x = x'$, the path is closed and periodic, forming the basis of the worldline formalism. The one-loop effective action is then:

$$\Gamma[V] = -\frac{1}{2}\int_0^\infty \frac{ds}{s} \int d^d x_0 \int_{x(0)=x(s)=x_0} \mathcal{D}x(t) \, \exp\left[-\int_0^s dt \left(\frac{\dot{x}^2(t)}{4} + V(x(t))\right)\right]. \tag{2.33}$$

This functional arises from the Schwinger proper-time representation of the operator trace $\mathrm{Tr}\log(-\partial^2 + V)$, which encodes the quantum corrections to the classical action at one-loop order. The integration over closed paths $x(t)$ with coincident endpoints, $x(0) = x(s) = x_0$, reflects the contribution of virtual particle loops in configuration space. The proper-time parameter s plays the role of an internal Schwinger parameter, controlling the scale of fluctuation modes. This formulation effectively rewrites the one-loop effective action as a path integral over particle trajectories, and is therefore known as the *worldline formalism*.

2.3.2 Partition Function, Ground-State Energy, and Functional Determinants

Having established the one-loop effective action in the Schwinger proper-time representation, we now interpret this formalism through the lens of statistical field theory, where thermodynamic quantities are naturally expressed via the partition function. The Euclidean path integral serves as a partition function encoding vacuum fluctuations and energy levels of the system.

In statistical mechanics, the partition function $\mathcal{Z}$ of a quantum system at temperature T is defined by tracing over the Boltzmann factor:

$$\mathcal{Z}(\beta) = \mathrm{Tr}\left(e^{-\beta \hat{H}}\right), \tag{2.34}$$

where $\hat{H}$ is the Hamiltonian operator, and $\beta = 1/(k_B T)$ is the inverse temperature. This quantity encodes the complete thermodynamic information of the system. In the low-temperature limit $\beta \to \infty$, the partition function is dominated by the ground state energy E_0, such that

$$\mathcal{Z}(\beta) \sim e^{-\beta E_0}, \qquad \Rightarrow \qquad E_0 = -\lim_{\beta\to\infty} \frac{1}{\beta} \log \mathcal{Z}(\beta). \tag{2.35}$$

Let us consider a free real scalar field $\phi(x)$ in d-dimensional spacetime with a quadratic Hamiltonian. After performing a Wick rotation $t \mapsto -i\tau$, the partition function becomes a Euclidean path integral over field configurations that are periodic in imaginary time with period β:

$$\mathcal{Z}(\beta) = \int_{\phi(0,\mathbf{x})=\phi(\beta,\mathbf{x})} \mathcal{D}\phi \, \exp\left[-\int_0^\beta d\tau \int d^{d-1}x \, \mathcal{L}_E(\phi)\right], \tag{2.36}$$

where the Euclidean Lagrangian density is given by

$$\mathcal{L}_E(\phi) = \frac{1}{2}\left(\frac{\partial\phi}{\partial\tau}\right)^2 + \frac{1}{2}(\nabla\phi)^2 + \frac{1}{2}m^2\phi^2 + \frac{1}{2}V(\mathbf{x})\phi^2. \tag{2.37}$$

This is a Gaussian path integral over a quadratic action. To evaluate it, we identify the quadratic form operator acting on ϕ:

$$A = -\partial_\tau^2 - \nabla^2 + m^2 + V(\mathbf{x}), \tag{2.38}$$

so the functional integral takes the standard form

$$\mathcal{Z}(\beta) \propto [\det A]^{-1/2}, \tag{2.39}$$

up to normalization factors irrelevant for thermodynamics. This is the infinite-dimensional analog of the standard Gaussian integral in finite dimensions.

The free energy is defined thermodynamically as

$$F(\beta) = -\frac{1}{\beta}\log\mathcal{Z}(\beta), \tag{2.40}$$

and substituting Eq. (2.39) gives

$$F(\beta) = \frac{1}{2\beta}\log\det A. \tag{2.41}$$

Using the identity $\log\det A = \mathrm{Tr}\log A$, valid for trace-class operators, we write

$$F(\beta) = \frac{1}{2\beta}\mathrm{Tr}\log A. \tag{2.42}$$

Therefore, the ground-state energy of the system can be expressed as

$$E_0 = -\lim_{\beta\to\infty} \frac{1}{\beta} \log \mathcal{Z}(\beta) = \lim_{\beta\to\infty} F(\beta). \tag{2.43}$$

Equivalently, using the product rule,

$$\frac{\partial}{\partial\beta} \log \mathcal{Z}(\beta) = -F(\beta) - \beta \frac{\partial F}{\partial\beta}, \tag{2.44}$$

so

$$E_0 = -\lim_{\beta\to\infty} \frac{\partial}{\partial\beta} \log \mathcal{Z}(\beta), \tag{2.45}$$

which is often taken as the operational definition of vacuum energy in terms of the partition function.

This result establishes a rigorous connection between the spectral properties of the differential operator A, the Euclidean functional integral, and the vacuum energy of the system. In worldline approaches to quantum field theory, this trace-log formula becomes the foundation for computing Casimir energies via a proper-time representation and Monte Carlo sampling of closed paths.

2.4 Worldline Form of Scalar Electromagnetism

2.4.1 Scalar Decomposition of Electromagnetism

The scalar field considered in the previous section is artificial and does not relate to realistic physical settings, since electromagnetism is a massless spin-1 gauge theory with two physical polarization degrees of freedom. In many applications of quantum electrodynamics, particularly those involving fluctuations or Casimir phenomena, it is advantageous to exploit symmetries in the system to simplify the vectorial

structure of the electromagnetic field. One widely used simplification is the scalar decomposition of the electromagnetic field, where the full vector field is separated into independent scalar components. This decomposition is especially useful in geometries with high symmetry, such as planar or cylindrical stratified media, where translational invariance in transverse directions enables a reduction of Maxwell's equations to scalar wave equations. These scalar reductions provide the foundation for scalar approximations in worldline path integral methods.

We begin with the action for a source-free electromagnetic field in a linear, isotropic, and inhomogeneous medium characterized by spatially varying permittivity $\varepsilon(z)$ and permeability $\mu(z)$. Working in the temporal gauge $\phi = 0$, the action becomes:

$$S[\mathbf{A}] = \frac{1}{2}\int d^4x \left[\varepsilon(z)\left(\frac{\partial \mathbf{A}}{\partial t}\right)^2 - \frac{1}{\mu(z)}\left(\nabla \times \mathbf{A}\right)^2\right], \tag{2.46}$$

where $\mathbf{A}(\mathbf{r}, t)$ is the vector potential. Varying this action with respect to $\mathbf{A}$ gives the Euler–Lagrange equations:

$$-\frac{\varepsilon(z)}{c^2}\frac{\partial^2 \mathbf{A}}{\partial t^2} + \nabla \times \left[\frac{1}{\mu(z)}\nabla \times \mathbf{A}\right] = 0. \tag{2.47}$$

We now specialize to a planar stratified geometry, in which $\varepsilon(z)$ and $\mu(z)$ depend only on the coordinate z. The system is translationally invariant in the transverse x- and y-directions. Therefore, we Fourier expand the fields in those directions:

$$\mathbf{A}(\mathbf{r}, t) = \mathbf{A}(z), e^{i(\mathbf{k}_\perp \cdot \mathbf{r}_\perp - \omega t)}, \tag{2.48}$$

with transverse momentum $\mathbf{k}_\perp = (k_x, k_y)$. The residual freedom in gauge fixing is removed by imposing the Coulomb gauge $\nabla \cdot \mathbf{A} = 0$, which, for the above ansatz,

reduces to:

$$i\mathbf{k}_\perp \cdot \mathbf{A}_\perp(z) + \partial_z A_z(z) = 0. \tag{2.49}$$

This constraint implies that only two independent field components remain — corresponding to the physical polarizations of the photon. These naturally split into TE and TM sectors.

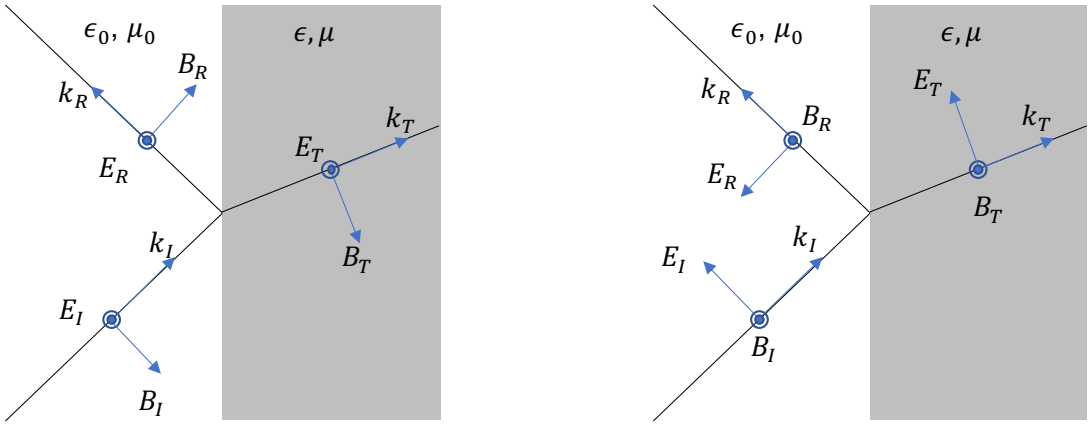

FIGURE 2.1. Decomposition of electromagnetic modes into TE and TM polarizations for a planar stratified system. TE modes have the electric field perpendicular to the plane of incidence, while TM modes have the magnetic field perpendicular to it.

Transverse Electric (TE) Modes. Choose the vector potential to be polarized along the y-direction: $\mathbf{A}(z) = A_y(z)\,\hat{\mathbf{y}}$. The electric and magnetic fields are then: $\mathbf{E} = -\partial_t \mathbf{A} = i\omega A_y(z)\hat{\mathbf{y}}$, $\mathbf{B} = \nabla \times \mathbf{A} = (\partial_z A_y\,\hat{\mathbf{x}} - ik_x A_y\,\hat{\mathbf{z}})$. The electric field is orthogonal to the x–z plane (plane of incidence), identifying this as the TE polarization. From Maxwell's equations, one obtains a scalar wave equation for $E_y(z,t)$:

$$\nabla \cdot \left(\frac{1}{\mu(z)}\nabla E_y\right) - \frac{\varepsilon(z)}{c^2}\frac{\partial^2 E_y}{\partial t^2} = 0. \tag{2.50}$$

Transverse Magnetic (TM) Modes. Now let the vector potential lie in the x–z plane: $\mathbf{A}(z) = A_x(z)\,\hat{\mathbf{x}} + A_z(z)\,\hat{\mathbf{z}}$. The Coulomb gauge implies a relation between A_x and A_z. The resulting magnetic field is: $\mathbf{B} = \nabla \times \mathbf{A} = (0,\, ik_x A_z - \partial_z A_x,\, 0)$. This configuration yields a magnetic field along $\hat{\mathbf{y}}$, defining the TM mode. The corresponding electric field lies in the x–z plane. The y-component $B_y(z,t)$ obeys a scalar wave equation:

$$\nabla \cdot \left(\frac{1}{\varepsilon(z)} \nabla B_y \right) - \frac{\mu(z)}{c^2} \frac{\partial^2 B_y}{\partial t^2} = 0. \tag{2.51}$$

Equations (2.50) and (2.51) describe the propagation of each polarization mode in an inhomogeneous medium. These equations form the basis of scalar approximations in electromagnetic Casimir computations. In the worldline formalism, each scalar equation admits a path-integral representation of its Green function, enabling efficient numerical evaluation of Casimir energies. As discussed in the next section, the spatial variation of $\varepsilon(z)$ and $\mu(z)$ enters as a position-dependent "mass" term, and the curvature-induced corrections are treated using the variable-mass path integral framework.

2.4.2 Electromagnetic Partition Function

As discussed in Sec. 2.3, the partition function of the physical system plays the pivotal role in calculating the ground-state energies. With the scalar decomposition of electromagnetic fields in Sec. 2.4.1, the equations of motion for TE (2.50) and TM

(2.51) fields respectively lead to the resulting actions:

$$S_{\text{TE}} = \frac{1}{2\mu_0}\int dx^4 \Big[\frac{\varepsilon(z)}{c^2}\big(\frac{\partial\phi}{\partial t}\big)^2 - \frac{1}{\mu(z)}|\nabla\phi|^2\Big], \tag{2.52}$$

$$S_{\text{TM}} = \frac{1}{2\varepsilon_0}\int dx^4 \Big[\frac{\mu(z)}{c^2}\big(\frac{\partial\varphi}{\partial t}\big)^2 - \frac{1}{\varepsilon(z)}|\nabla\varphi|^2\Big] \tag{2.53}$$

The partition function for either scalar field (TE or TM) is given by the Euclidean path integral over periodic field configurations, with the action determined by the corresponding scalar wave operator. Explicitly,

$$\mathcal{Z}_{\text{TE}} = \int \mathcal{D}\phi \exp\left[-\frac{1}{2\hbar c\mu_0}\int_0^{\beta\hbar c} d\tau \int dx^3 \left(\varepsilon(\mathbf{x})\big(\frac{\partial\phi}{\partial\tau}\big)^2 + \frac{1}{\mu(\mathbf{x})}|\nabla\phi|^2\right)\right], \tag{2.54}$$

where $\tau \equiv \beta\hbar c$. The TM partition function can be obtained by the swapping symmetry $\mathbf{E} \leftrightarrow \mathbf{H}, \mathbf{B} \leftrightarrow -\mathbf{D}, \varepsilon \leftrightarrow \mu$.

According to the development in Sec. 2.3.2, the partition function is totally determined by the imaginary-time Green operator corresponding to each scalar mode

$$\log \mathcal{Z}_i = \frac{1}{2}\text{Tr}\log G_i\big|_{t\to i\hbar\beta} \tag{2.55}$$

where $i \in \{\text{TE}, \text{TM}\}$.

In the TE sector, for instance, the Green operator for an inhomogeneous, linear, isotropic medium with spatially varying permittivity and permeability takes the form

$$G_{\text{TE}} = \left[-\nabla\cdot\left(\frac{1}{\mu(\mathbf{r})}\nabla\right) + \frac{\varepsilon(\mathbf{r})}{c^2}\big(\frac{\partial}{\partial t}\big)^2\right]^{-1}. \tag{2.56}$$

In the worldline representation, the term $1/\mu(\mathbf{r})$ in the Laplacian acts as a position-dependent mass, which leads to a nontrivial curved-space kinetic term in the

worldline action:

$$S_{\rm kin}[\mathbf{x}(\tau)] \propto \int_0^{\mathcal{T}} d\tau\, \mu(\mathbf{x}(\tau))\, \dot{\mathbf{x}}^2(\tau). \tag{2.57}$$

To simplify the structure of the kinetic term, we define a rescaled operator via a transformation using $\mu^{1/2}(\mathbf{r})$:

$$\tilde{G}^{-1}_{\rm TE} = \mu^{1/2}(\mathbf{r})\, G^{-1}_{\rm TE}\, \mu^{1/2}(\mathbf{r}). \tag{2.58}$$

The goal here is to use the operator commutation relation to remove space-dependent masses on the ∇^2 terms, effectively recasting the Green operator in flat space. The consequence of this process is to introduce extra effective potentials. Specifically, these matter-induced potentials are given by

$$\begin{aligned} V_{\rm TE} &= \frac{1}{2}[(\nabla \log\sqrt{\mu})^2 - \nabla^2 \log\sqrt{\mu}] \\ V_{\rm TM} &= \frac{1}{2}[(\nabla \log\sqrt{\varepsilon})^2 - \nabla^2 \log\sqrt{\varepsilon}]. \end{aligned} \tag{2.59}$$

Finally, the electromagnetic partition functions in scalar decomposition (2.54) are evaluated to be

$$\begin{aligned} \mathcal{Z}_{\rm TE} &= \det\left[-\frac{1}{2}\varepsilon\mu\partial_\tau^2 - \frac{1}{2}\nabla^2 - V_{\rm TE}\right]^{-1/2} \\ \mathcal{Z}_{\rm TM} &= \det\left[-\frac{1}{2}\varepsilon\mu\partial_\tau^2 - \frac{1}{2}\nabla^2 - V_{\rm TM}\right]^{-1/2}, \end{aligned} \tag{2.60}$$

2.4.3 Worldline Casimir Energies and Renormalization

To extract zero-temperature Casimir energies from the field-theoretic partition function, one considers the ground-state energy encoded in the logarithm of the

partition function. Specifically, the vacuum energy is given formally by

$$E = -\frac{\partial}{\partial\beta}\log\mathcal{Z}(\beta)\bigg|_{\beta\to\infty}, \tag{2.61}$$

which captures the dominant contribution from the lowest energy eigenstate in the zero-temperature limit. However, this energy includes divergent contributions from the self-energies of individual objects and the infinite vacuum energy of the free field. Since only energy differences are physically meaningful, a renormalization procedure must be employed. This is typically achieved by subtracting the energy of a reference configuration—usually the same system with objects placed at infinite separation—which yields a finite, well-defined Casimir interaction energy:

$$E_{\text{Casimir}} = -\frac{\partial}{\partial\beta}\left[\log\mathcal{Z}(\beta) - \log\mathcal{Z}_0(\beta)\right]_{\beta\to\infty}. \tag{2.62}$$

This subtraction removes geometry-independent vacuum divergences and isolates the finite interaction energy due to boundary conditions or material interfaces. The choice of reference configuration, while arbitrary in principle, is commonly taken to be a configuration in which the objects are sufficiently far apart such that their mutual interaction vanishes.

To evaluate Casimir energies, the key is to represent $\log\mathcal{Z}$ in a convenient form. Here we choose to utilize $\log\det A = \operatorname{Tr}\log A$ to recast it into trace-log form, and apply the integral representation of logarithm (2.29). After these transforms, the development of worldline expressions then follows directly from standard path-integral treatments. The unrenormalized Casimir energy in terms of worldlines is then

$$E_i = -\frac{\hbar c}{2(2\pi)^{D/2}}\int_0^\infty \frac{d\mathcal{T}}{\mathcal{T}^{1+D/2}}\int d\mathbf{x}_0\left\langle\!\!\left\langle \frac{e^{-\mathcal{T}\langle V_i\rangle}}{\langle\varepsilon\mu\rangle^{1/2}}\right\rangle\!\!\right\rangle_{\mathbf{x}(t)}, \tag{2.63}$$

where $i \in \{\mathrm{TE}, \mathrm{TM}\}$ and the double angled brackets denote an ensemble average over Brownian bridges that start at $\mathbf{x}_0$, with running time $\mathcal{T}$. The single brackets represent path average of a functional

$$\langle f[\mathbf{x}] \rangle = \frac{1}{\mathcal{T}} \int_0^{\mathcal{T}} d\tau \, f[\mathbf{x}(\tau)]. \tag{2.64}$$

The variable $\mathcal{T}$ here is the "proper time" by analogy with the Schwinger formalism in Sec. 2.3.1. In Casimir energy computations, however, it is important to emphasize that $\mathcal{T}$ in this context is not the actual proper time of a physical relativistic particle. Rather, it is a dimensionful auxiliary variable arising from the Schwinger representation of the functional determinant, and it governs the scale of the virtual loop fluctuations contributing to the Casimir energy. The corresponding proper time variable $\mathcal{T}$ in fact has a dimension of length squared. This is consistent with interpreting $\mathcal{T}$ as controlling the typical extent of the fluctuating worldline paths, which scale as $\sqrt{\mathcal{T}}$. In Casimir settings, $\mathcal{T}$ acts as a resolution parameter: short $\mathcal{T}$ probes ultraviolet (small-scale) contributions near surfaces, while large $\mathcal{T}$ captures long-range effects.

Details of the derivation of worldline path integrals can be found in Ref. [27].

2.4.4 Worldline Casimir–Polder Potentials

The Casimir energy of scalar EM in the worldline form is

$$E_{\mathrm{EM}} = -\frac{\hbar c}{2(2\pi)^{D/2}} \int_0^\infty \frac{d\mathcal{T}}{\mathcal{T}^{1+D/2}} \int d^{D-1}x_0 \left\langle\!\!\left\langle \langle \epsilon_r \mu_r \rangle_{x(\tau)}^{-1/2} e^{-\mathcal{T}\langle V \rangle_{x(\tau)}} \right\rangle\!\!\right\rangle_{x(\tau)}, \tag{2.65}$$

where V in the exponential is either V_{TE} or V_{TM} depending on the polarization mode considered.

In principle, Casimir–Polder interactions between an atom and a macroscopic object can be computed by modeling the atom as a small piece of magnetodielectric material embedded within the environment. However, in the worldline numerical framework, the naive generation of paths suffers from poor efficiency since the atom occupies an extremely small region of space, and the vast majority of randomly sampled closed loops will fail to intersect it, yielding negligible contribution to the renormalized energy. In fact, only those loops that simultaneously intersect both the atomic location and the macroscopic medium can contribute meaningfully to the two-body Casimir interaction after renormalization.

To address this, it is advantageous to employ a tailored path-integral formulation adapted specifically to the atom-surface configuration. The introduction of the atom is modeled by a sharply localized perturbation to the medium's permittivity and permeability:

$$\delta\varepsilon(\mathbf{r}) = \frac{\alpha_0}{\varepsilon_0}\,\delta^{(D-1)}(\mathbf{r}-\mathbf{r}'), \qquad \delta\mu(\mathbf{r}) = \mu_0\beta_0\,\delta^{(D-1)}(\mathbf{r}-\mathbf{r}'), \tag{2.66}$$

where α_0 and β_0 represent the static polarizability and magnetizability of the atom located at $\mathbf{r}'$. The relevant interaction energy is given by the difference between the Casimir energies in the presence and absence of the atomic perturbation. Assuming the perturbations are small, this energy shift can be computed via first-order functional derivatives:

$$\begin{aligned}\delta E &= E[\varepsilon+\delta\varepsilon, \mu+\delta\mu] - E[\varepsilon,\mu] \\ &= \int d\mathbf{r}\left[\frac{\delta E}{\delta\varepsilon(\mathbf{r})}\delta\varepsilon(\mathbf{r}) + \frac{\delta E}{\delta\mu(\mathbf{r})}\delta\mu(\mathbf{r}) + \mathcal{O}[(\delta\varepsilon)^2, (\delta\mu)^2]\right],\end{aligned} \tag{2.67}$$

Substituting Eq. (2.66), we obtain:

$$\delta E = \frac{\alpha_0}{\varepsilon_0} \frac{\delta E}{\delta \varepsilon(\mathbf{r})}\bigg|_{\mathbf{r}=\mathbf{r}'} + \mu_0 \beta_0 \frac{\delta E}{\delta \mu(\mathbf{r})}\bigg|_{\mathbf{r}=\mathbf{r}'}. \tag{2.68}$$

Although the perturbation $\delta\varepsilon$ is singular, the Taylor expansion is not performed with respect to the delta function itself, but rather in terms of a small physical parameter — the atomic polarizability α_0. We model the permittivity profile as a background plus a localized perturbation due to the atom:

$$\varepsilon(\mathbf{x}) = \varepsilon_{\text{bg}}(\mathbf{x}) + \delta\varepsilon(\mathbf{x}), \quad \text{with} \quad \delta\varepsilon(\mathbf{x}) = \frac{\alpha_0}{\epsilon_0} f_\eta(\mathbf{x} - \mathbf{r}), \tag{2.69}$$

where f_η is a smooth, normalized bump function localized near the atomic position $\mathbf{r}$ with characteristic width $\eta \ll \lambda$ (the field variation scale). The energy functional is then expanded in α_0:

$$E[\varepsilon + \delta\varepsilon] = E[\varepsilon] + \frac{\alpha_0}{\epsilon_0} \int d^D\mathbf{x} \, \frac{\delta E}{\delta \varepsilon(\mathbf{x})} f_\eta(\mathbf{x} - \mathbf{r}) + \mathcal{O}(\alpha_0^2). \tag{2.70}$$

In the point-dipole limit $\eta \to 0$, we identify $f_\eta(\mathbf{x} - \mathbf{r}) \to \delta(\mathbf{x} - \mathbf{r})$, and the first-order correction becomes

$$\Delta E = \frac{\alpha_0}{\epsilon_0} \, \frac{\delta E}{\delta \varepsilon(\mathbf{x})}\bigg|_{\mathbf{x}=\mathbf{r}}. \tag{2.71}$$

Thus, the delta function is not introduced directly in the expansion, but rather as a notational shorthand for a localized finite distribution, always accompanied by the small factor α_0. The limit is taken *after* the functional derivative is evaluated. This procedure is consistent with the physical assumption that the atom is much smaller than the wavelength of the field, justifying its treatment as a point dipole.

The delta function is a convenient and well-defined distributional representation of this limit.

This expression (2.68) represents the Casimir–Polder potential experienced by the atom due to its magnetodielectric environment. Physically, it corresponds to the change in ground-state energy arising from the interaction of the atom's dipole moments with vacuum fluctuations modulated by the macroscopic body.

Given the worldline expression of the energy Eq. (2.65), we explicitly calculate the variations in V_{TE} and the path-averaged material properties, which leads to the TE-mode Casimir–Polder expression:

$$V_{\mathrm{CP}}^{\mathrm{TE}}(\mathbf{r}) = \frac{\hbar c}{4(2\pi)^{D/2}} \int_0^\infty \frac{d\mathcal{T}}{\mathcal{T}^{1+D/2}} \Bigg\langle\!\!\Bigg\langle \left(\alpha_0 \varepsilon_0^{-1} \mu(\mathbf{r}) + \beta_0 \mu_0 \varepsilon(\mathbf{r}) \right) \langle \varepsilon\mu \rangle^{-3/2} e^{-\mathcal{T}\langle V_{\mathrm{TE}} \rangle} - \frac{\beta_0 \mu_0 \mathcal{T}}{2\mu(\mathbf{r})} \left[\nabla^2 \log\mu + \nabla \log\mu \cdot \nabla + \nabla^2 \right] \langle \varepsilon\mu \rangle^{-1/2} e^{-\mathcal{T}\langle V_{\mathrm{TE}} \rangle} \Bigg\rangle\!\!\Bigg\rangle_{\mathbf{x}(t)|\mathbf{x}(0)=\mathbf{r}} . \quad (2.72)$$

The TM expression can be obtained via the duality symmetry $\beta_0\mu_0 \leftrightarrow \alpha_0/\varepsilon_0, \mu \leftrightarrow \varepsilon, V_{\mathrm{TE}} \leftrightarrow V_{\mathrm{EM}}$. The path is pinned to start and end at the atomic location. This is the consequence of the delta functions present in the atomic perturbations. Detailed calculations of inter-atomic Casimir–Polder potentials will be shown in **Chapter IV**.

The renormalization of Casimir–Polder worldlines is addressed as follows. For an atom located at position $\mathbf{r}$ in otherwise empty space, the divergent contribution to the Casimir–Polder potential arises from the field modes interacting with the point-like atomic polarizability. This divergence is canceled by subtracting the reference configuration in which all material boundaries are moved to infinity:

$$V_{\mathrm{ren}}(\mathbf{r}) = V(\mathbf{r}) - V_\infty(\mathbf{r}), \quad (2.73)$$

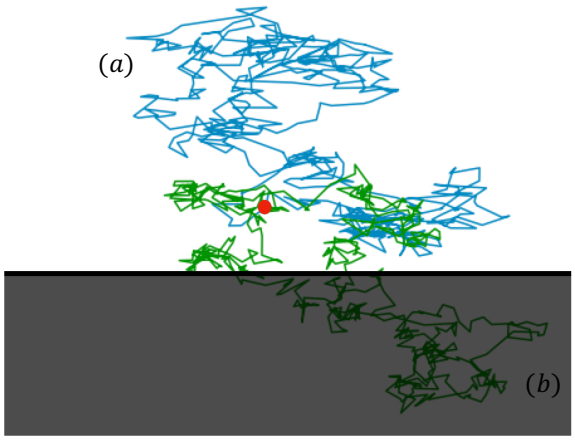

FIGURE 2.2. Casimir–Polder worldlines pinned to the atomic position. (a) The vacuum loop does not contribute to the potential. (b) Only the one that sojourns the medium contributes.

where $V_\infty(\mathbf{r})$ denotes the potential the atom would experience if the material bodies were infinitely far removed. This subtraction removes the $\mathcal{T} \to 0$ divergence in the worldline path integral representation, yielding a finite, renormalized Casimir–Polder energy.

On the other hand, consider an atom embedded within the dielectric half-space of a vacuum-dielectric planar interface. Even though the atom is inside a homogeneous material, the presence of the interface modifies the vacuum fluctuations and leads to a nontrivial potential. However, the total energy again contains an unphysical divergent part corresponding to the bulk dielectric environment. To isolate the interaction with the interface, we subtract the contribution from a configuration in which the interface is moved infinitely far away, while the atom remains embedded in the same dielectric medium:

$$V_{\mathrm{ren}}^{(\mathrm{interface})}(\mathbf{r}) = V(\mathbf{r}) - V_{\mathrm{bulk}}(\mathbf{r}), \tag{2.74}$$

where $V_{\text{bulk}}(\mathbf{r})$ is the Casimir–Polder energy of the atom in an infinite homogeneous dielectric with no boundaries. This ensures that the renormalized potential captures only the influence of the interface, removing the background self-energy contribution.

In the worldline path-integral formalism, this subtraction is implemented by only counting particle paths that intersect or are reflected by material boundaries. Paths entirely confined to homogeneous regions contribute identically in both configurations and cancel under subtraction. As such, the renormalized energy corresponds to the difference in path averages between the actual geometry and its reference configuration, ensuring a finite result. See Fig. 2.2 for an illustration.

2.5 Monte Carlo Simulation

Monte Carlo simulation is a class of numerical techniques that estimate quantities of interest by averaging over random samples. The method is particularly powerful for evaluating high-dimensional integrals, solving stochastic differential equations, or sampling from probability distributions that are analytically intractable.

In a typical setting, Monte Carlo methods are used to compute an expectation value of the form

$$\mathbb{E}[f(X)] = \int f(x)p(x)\,dx, \tag{2.75}$$

where $p(x)$ is a probability density function and $f(x)$ is an integrable function. This expectation can be approximated by sampling independent random variables $x_1, \ldots, x_N$ from $p(x)$ and computing the sample mean:

$$\mathbb{E}[f(X)] \approx \frac{1}{N}\sum_{i=1}^{N} f(x_i). \tag{2.76}$$

The central limit theorem ensures that, as $N \to \infty$, the error in this approximation scales as $1/\sqrt{N}$, independent of the dimensionality of x. This dimension-independence makes Monte Carlo methods especially attractive for problems involving many degrees of freedom, such as statistical mechanics, quantum field theory, and Bayesian inference.

Modern variants, such as importance sampling and Markov chain Monte Carlo (MCMC), are designed to improve efficiency and reduce variance by tailoring the sampling strategy to the specific structure of the problem. For the worldline approach, Monte Carlo simulation provides a natural numerical method to estimate functional integrals over stochastic paths, by generating ensembles of random trajectories and computing observables as statistical averages over them.

In the context of Casimir calculations, a typical worldline expression of an observable takes the form of

2.5.1 Path Generation

The numerical evaluation of worldline path integrals is central to the Casimir calculations presented in this thesis. Essentially, it relies on sampling an ensemble of stochastic trajectories. These trajectories are realizations of Brownian paths, discretized in time and conditioned to satisfy certain boundary conditions. The foundational stochastic process for this purpose is the *Brownian bridge*, which represents a Brownian (Wiener) process constrained to begin and end at prescribed values.

In its simplest form, a Brownian bridge $B(t)$ over the interval $t \in [0, 1]$ is a one-dimensional process satisfying $B(0) = B(1) = 0$. For intermediate times, it

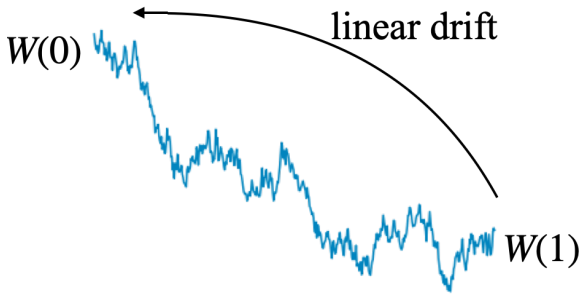

FIGURE 2.3. Linear drift applied to Wiener processes to force the bridge closure.

undergoes Gaussian diffusion according to standard Wiener statistics:

$$\langle\langle dB(t) \rangle\rangle = 0, \tag{2.77}$$

$$\langle\langle dB(t)\, dB(t') \rangle\rangle = \delta(t - t')\, dt. \tag{2.78}$$

A discrete representation of such a path can be generated numerically by sampling N steps $\{B_j\}_{j=0}^{N}$ with $B_0 = B_N = 0$, and evolving the intermediate points via a recurrence relation.

The algorithm used in this thesis to construct discrete Brownian bridges is adapted from the so-called "v-loop" method introduced by Gies *et al.* [22] and modified in [27]. It generates successive points B_j by

$$B_j = \sqrt{\frac{c_j}{N}}\, z_j + c_j B_{j-1}, \quad j = 1, \ldots, N-1, \tag{2.79}$$

where z_j are independent standard normal random variables, $B_0 = 0$, $B_N = 0$, and the recursion coefficients are defined by

$$c_j = \frac{N - j}{N - j + 1}. \tag{2.80}$$

This procedure yields realizations of paths consistent with the Brownian bridge measure corresponding to fixed endpoints at the origin.

In more sophisticated numerical procedures — such as the partial-averaging method introduced in **Chapter III** — one requires Brownian bridges with arbitrary endpoints, $B(0) = a$ and $B(1) = b$. The recurrence (2.79) generalizes in this case to

$$B_j = \sqrt{c_j \Delta t}\, z_j + c_j(B_{j-1} - b) + b, \quad j = 1, \ldots, N-1, \tag{2.81}$$

where $\Delta t = 1/N$ is the time step, and the endpoint conditions $B_0 = a$ and $B_N = b$ are enforced.

In several applications, such as the Hermite–Gaussian partial averaging method in Sec. 3.2.2, only a segment of the path is constructed a priori (e.g., the first m and last m time steps), while the intermediate section must be filled in using a conditioned Brownian bridge. Suppose we have determined the value of the path at some intermediate index k, i.e., B_k is known, and we wish to sample the remaining $N_k = N - k$ steps from $t = k/N$ to $t = 1$ subject to the final endpoint $B_N = 0$.

The remaining portion is then generated by shifting the generalized bridge formula (2.81):

$$B_j = \sqrt{\frac{c_j}{N}}\, z_j + c_j(B_{j-1} - b) + b, \quad j = k+1, \ldots, N-1, \tag{2.82}$$

with B_k as the starting point, $b = B_N = 0$ as the final endpoint, and recursion coefficients

$$c_j = \frac{N-j}{N-j+1}. \tag{2.83}$$

Note that the indices in Eq. (2.82) have been shifted to match the segment $j \in \{k+1, \ldots, N-1\}$, and thus this process can be interpreted as the final N_k steps of a standard bridge over $[0,1]$ translated to begin at $t = k/N$.

This completion method plays an essential role in ensuring the consistency of path segments and facilitates recursive evaluation of quantities such as path derivatives, curvature estimators, or reweighted observables. It also ensures compatibility with boundary or symmetry constraints imposed by the underlying physics of the Casimir interaction being modeled.

2.5.2 Proper Time Sampling

In the worldline representation of Casimir energies, the quantum effective action is expressed as a path integral over an ensemble of closed trajectories, each scaled by a proper time $\mathcal{T}$ that parametrizes the physical size of the loop. The total energy or force is computed by averaging the contribution of such loops over a distribution of $\mathcal{T}$, weighted by a characteristic power-law kernel.

However, for a given Brownian path, its contribution to the renormalized integrand is zero unless the loop intersects all of the relevant bodies in the geometry. This condition is met only when $\mathcal{T}$ exceeds a minimal value $\mathcal{T}_0$, which is the first proper time at which the path intersects the geometry as required. For example:

- In the worldline approach to Casimir energies, the renormalized interaction energy arises from paths that intersect all relevant bodies. For instance, consider a one-dimensional Brownian bridge starting at a point x_0 located between two parallel planes at positions $L_1 < x_0 < L_2$. A given path only contributes to the Casimir interaction energy if it touches both boundaries during its evolution.

To determine the minimal proper time $\mathcal{T}$ required for such a path to reach both boundaries, we must consider the maximal spatial excursion of the Brownian path relative to its total proper time. In one dimension, the spatial extent of a standard Brownian bridge scales as $\sim \sqrt{\mathcal{T}}$. Therefore, the condition for a path to reach the lower or upper plane is: $|x_0 - L_{1,2}| \lesssim x_{\max} \sim \sqrt{\mathcal{T}}$. Inverting this gives the minimal proper time needed to reach each boundary: $\mathcal{T}_{1,2} = \frac{(x_0 - L_{1,2})^2}{x_\pm^2}$ where $x_\pm$ is the normalized extremum (typically the maximum displacement from the bridge trajectory, which is sampled over the ensemble). The smallest such proper time $\mathcal{T}_0$ that ensures intersection with both objects is then:

$$\mathcal{T}_0 = \max\left[\frac{(L_1 - x_0)^2}{x_-^2}, \frac{(L_2 - x_0)^2}{x_+^2}\right]. \tag{2.84}$$

This cutoff time determines the lower limit of integration in the worldline representation of the Casimir energy. Paths with $\mathcal{T} < \mathcal{T}_0$ are too short to reach both boundaries and hence do not contribute to the interaction part of the energy.

– In Casimir–Polder energies, $\mathcal{T}_0$ is the time beyond which the path intersects the extended body (excluding the atom itself).

This motivates the use of an importance sampling distribution for $\mathcal{T}$, tailored to each path, that captures both the lower bound $\mathcal{T}_0$ and the asymptotic power-law behavior of the kernel. A particularly effective choice is the truncated power-law:

$$P(\mathcal{T}; \mathcal{T}_0, m) = \frac{(m-1)\mathcal{T}_0^{m-1}}{\mathcal{T}^m}\,\Theta(\mathcal{T} - \mathcal{T}_0), \tag{2.85}$$

where $m > 1$ and Θ is the Heaviside step function. This choice ensures that $P(\mathcal{T})$ is properly normalized over $\mathcal{T} \in [\mathcal{T}_0, \infty)$, and mimics the power-law decay of the integrand while avoiding unnecessary sampling below the physical cutoff $\mathcal{T}_0$.

To generate random samples of $\mathcal{T} \sim P(\mathcal{T}; \mathcal{T}_0, m)$, one uses the inverse transform sampling method. The cumulative distribution function (CDF) is

$$F(\mathcal{T}) = \int_{\mathcal{T}_0}^{\mathcal{T}} P(\mathcal{T}'; \mathcal{T}_0, m)\, d\mathcal{T}' = 1 - \left(\frac{\mathcal{T}_0}{\mathcal{T}}\right)^{m-1}, \tag{2.86}$$

whose inverse is

$$\mathcal{T}(u) = \mathcal{T}_0\,(1-u)^{-1/(m-1)}, \tag{2.87}$$

where $u \in (0, 1)$ is a uniformly distributed random number. Thus, the sampling algorithm is as follows:

1. For each loop, estimate the minimal contributing time $\mathcal{T}_0$ based on the rescaled geometry.

2. Generate a uniform random variable $u \in (0, 1)$.

3. Compute $\mathcal{T} = \mathcal{T}_0(1-u)^{-1/(m-1)}$.

In practice, $\mathcal{T}_0$ is estimated per path by scaling the Brownian loop and checking whether it intersects the geometry. This may involve a search over $\mathcal{T}$ for which the loop first touches all required surfaces or in symmetric geometries, an analytic expression for the minimal spanning time.

Once $\mathcal{T}_0$ is determined, one draws $\mathcal{T} \sim P(\mathcal{T}; \mathcal{T}_0, m)$ and rescales the path accordingly. The integrand for the Casimir energy is then evaluated and reweighted by $\mathcal{T}^{-1-D/2}/P(\mathcal{T})$, preserving the correctness of the total integral.

This strategy is essential in reducing the cost of computing Casimir interactions across a wide range of length scales. By focusing sampling effort on physically relevant regions of proper time, the truncated power-law distribution ensures accurate estimates with fewer Monte Carlo samples.

2.5.3 Path Source Point Reweighting

In the worldline path integral formulation of Casimir energies, one often encounters an integral over the spatial base point x_0 of a closed Brownian path. Physically, x_0 represents the center of mass or anchor point of the loop, and its integration accounts for all possible global translations of the loop in space. Mathematically, this appears in expressions such as

$$E \propto \int_0^\infty \frac{d\mathcal{T}}{\mathcal{T}^\alpha} \int_{\mathbb{R}^d} d^d x_0 \left\langle\!\!\left\langle \mathcal{O}[x(t)] \right\rangle\!\!\right\rangle_{x_0,\mathcal{T}}, \tag{2.88}$$

where $\mathcal{O}[x(t)]$ is a path-dependent observable encoding the interaction with external boundaries or media.

In many cases, especially for geometries involving infinite parallel planes, this integration can be greatly simplified due to the structure of the observable and the properties of the contributing paths. Specifically, consider a geometry involving two parallel planes separated by a distance a, and a loop ensemble generated for computing the Casimir energy in this setup. The key observation is that only those loops which intersect the gap between the two plates contribute nontrivially to the energy. Loops that lie entirely outside this interaction region cancel upon subtraction of the free-space vacuum energy.

Because only loops intersecting the gap contribute, the domain of integration over x_0 can be effectively restricted to the projection of the loop onto the direction perpendicular to the plates—i.e., to the interval

$$x_0 \in [x_{\min}, x_{\max}], \tag{2.89}$$

where $x_{\min}$ and $x_{\max}$ denote the minimum and maximum coordinates of a particular loop $x(t)$ along the normal direction. This observation allows one to either numerically integrate x_0 over this finite interval for each loop, or replace the integration over x_0 by a suitably weighted Monte Carlo average over representative points on the loop. The latter approach is more computationally efficient and commonly adopted in the worldline numerics involved in this thesis.

To approximate the integral over x_0 via Monte Carlo sampling, one may choose a discrete point x_k from the loop path $\{x_j\}_{j=0}^{N-1}$, and identify it with x_0. This amounts to replacing the continuous uniform integral over $x_0 \in [x_{\min}, x_{\max}]$ by uniform random sampling from the N discrete path points $\{x_j\}$. However, the discrete points x_j are not uniformly distributed over the interval—they reflect the stochastic nature of Brownian motion, with higher density near the center.

To account for this nonuniformity and preserve unbiased estimation, a corrective weighting factor must be applied.

Let us suppose:

– x_k is the path point selected as the representative for x_0,

– x_{k-} is the largest path point before x_k such that $x_{k-} < x_k$,

– x_{k+} is the smallest path point after x_k such that $x_{k+} > x_k$.

If one had drawn x_0 uniformly from the continuous interval $[x_{\min}, x_{\max}]$, then the probability that x_0 lands in the interval (x_{k-}, x_{k+}) is approximately

$$P(x_0 \in (x_{k-}, x_{k+})) = \frac{x_{k+} - x_{k-}}{x_{\max} - x_{\min}}. \tag{2.90}$$

However, when x_k is chosen uniformly among the N path points, the selection probability is $1/N$. To correct for this mismatch in distributions, we apply the ratio of the two probabilities as a Monte Carlo weight:

$$w_k = \frac{P_{\text{uniform}}(x_0 \in (x_{k-}, x_{k+}))}{P_{\text{MC}}(x_k)} = \frac{(x_{k+} - x_{k-})/(x_{\max} - x_{\min})}{1/N} = \frac{N(x_{k+} - x_{k-})}{x_{\max} - x_{\min}}. \tag{2.91}$$

In practice, rather than normalizing over the full path width $x_{\max} - x_{\min}$, one can factor it out in global normalization and define the relative Monte Carlo weight as:

$$w_k \propto \frac{1}{2} N(x_{k+} - x_{k-}), \tag{2.92}$$

where the factor of $1/2$ accounts for symmetric treatment around the midpoint. This weighting ensures that, averaged over many loops and sampling points, the estimation reproduces the correct integral over x_0.

For maximum computational efficiency and symmetry, a common choice is to fix x_0 to a point through which all contributing paths must pass, such as the midpoint between the plates. In such cases, one can skip sampling and directly evaluate observables at this fixed x_0, provided the appropriate normalization or weighting is retained.

In summary, the integral over the loop base point x_0 in worldline Casimir energy calculations can be replaced by stochastic sampling of loop points, provided a

correction factor is applied to account for the non-uniform distribution of Brownian paths. This technique significantly reduces computational cost while preserving accuracy, and is particularly powerful in planar geometries where translational symmetry allows for analytical simplifications.

CHAPTER III

PATHWISE DIFFERENTIATION OF WORLDLINE PATH INTEGRALS

This work was conducted in collaboration with former graduate student Jonathan B. Mackrory, under the supervision of Daniel A. Steck, and has been published in *Physical Review A* [28]. Jonathan contributed to the development of the partial averaging framework and conducted numerical analysis on the differentiation of the Casimir–Polder energy. Daniel conceived the methods for differentiation and performed numeric simulations for the one-body and two-body methods. My contributions include solving for the Casimir energy in the two-delta-plane model and implementing numerical methods to compute its derivatives through worldline simulations.

3.1 Introduction

The Casimir effect is a fundamental consequence of quantum fields interacting with boundaries [1]. It typically arises as an attractive force between material bodies due to modifications of vacuum fluctuations by the presence of the bodies [7, 29]. An important experimental technique for measuring Casimir-type forces monitors the change in the frequency of a mechanical oscillator due to the presence of another dielectric body: Such experiments are sensitive to the *curvature* of the Casimir energy. This technique has been applied, for example, to Casimir-force measurements in microelectromechanical systems [30] and also to Casimir–Polder measurements with Bose-Einstein condensates in a magnetic trap near a dielectric mirror [31]. Theoretical predictions of Casimir forces (and corresponding frequency shifts in

experiments) require the computation of gradients of the Casimir energy. In general geometries, this requires a numerical approach.

The worldline path-integral method in particular is a promising framework for the numerical computation of Casimir energies [22, 23, 27, 32, 33, 34, 35, 36, 37, 38, 39, 40, 41, 42]. It continues to be a useful method in various areas of quantum field theory [43, 44, 45, 46, 47]. In this method one generates an ensemble of closed stochastic paths and evaluates the Casimir energy as a functional average over the material properties along the paths. The worldline method has been thus far primarily applied in the case of scalar fields interacting with Dirichlet boundary conditions [23, 32, 33, 34, 35]. For example, this work has been applied to computing Casimir forces and torques for cylinder-plate, sphere-plate, and inclined-plate geometries [36, 38], as well as to computing the stress-energy tensor for parallel planes [40, 42]. More recently, the worldline method has been extended to incorporate the coupling of the electromagnetic field to magnetodielectric media [27]. In that reference, the electromagnetic worldline path integrals are only exact in symmetric geometries where the vector electromagnetic field splits into two uncoupled scalar fields.

In connecting the worldline method to experiments, where one is interested in forces and curvatures as numerical quantities, it is therefore important to consider the numerical differentiation of worldline path integrals. Additionally, the worldline path integral for the part of the Casimir–Polder potential corresponding to the transverse-magnetic (TM) polarization involves the second derivative of a worldline path integral [27]. Similarly, the calculation of the stress-energy tensor via worldline methods involves derivatives of worldline path integrals [40, 42, 48]. Due to the importance of estimating gradients of Monte Carlo path averages in other areas

such as mathematical finance, there has already been a substantial effort towards developing general methods for differentiating path integrals [49, 50]. Since the methods in this paper apply quite generally, they may be applicable to such problems.

The most straightforward way to compute a numerical derivative is the finite-difference method. While finite-difference approximations are quite general and easy to implement, they have poor convergence properties for gradients of stochastic quantities [49, 50]. In computing a first derivative, for example, one needs to compare functional values of two slightly different paths, and then divide by a small parameter that characterizes the difference between them. In such averages over stochastic paths, the difference in the contributions of these paths may be large—in a worldline path integral, for example, one path may intersect a dielectric while its slightly shifted counterpart misses it, but these differences are precisely what determine the Casimir force. Thus, the finite-difference method can lead to a path average with a large sample variance, requiring extensive averaging—and thus excessive computing resources—to arrive at an accurate result. The problem is even worse for successive derivatives.

In this paper we present numerically efficient methods for computing gradients of worldline path integrals in two classes of problems. First, we consider derivatives of Casimir–Polder path integrals, where the derivatives are taken with respect to the source point of the paths. In this case, a reweighted path integral serves to compute the derivatives, but a partial-averaging technique is needed to avoid convergence problems in the limit of continuous-time paths. This method applies rather generally to numerical path integrals differentiated with respect to the source point. For example, it applies whenever the path functional is independent of the motion of the

path in some neighborhood of the source point. It also applies if the path functional may be approximately averaged over some time interval around the source point.

In the second class of problems, we consider the calculation of Casimir forces, curvatures, and torques due to extended material bodies. A particularly relevant method is that of Weber and Gies, who computed forces in the sphere–plane and cylinder–plane geometries with Dirichlet boundary conditions [38]. In that work paths are shifted until they graze the planar surface, taking advantage of the freedom of the integral over $\mathbf{x}_0$. The force on the planar surface is then computed by integrating over the times when the path intersects the spherical or cylindrical surface. By contrast, we consider a generally valid method that sums over the derivative of an estimate of the path average or value between two successive points in the discrete path. Again, a partial-averaging method accelerates convergence.

3.2 Derivatives of Worldline Casimir–Polder Energies

To serve as a concrete example of path-integral differentiation, we will consider Casimir-type energies for the scalar field corresponding to the transverse-electric (TE) polarization of the electromagnetic field coupled to a dielectric [27]. In the strong-coupling (perfect-conductor) limit, this path integral imposes the same Dirichlet boundary conditions as in the path integrals considered by Gies *et. al* [22].

The basic expression for the Casimir energy of this scalar field in a dielectric-permittivity background $\epsilon(\mathbf{r})$ is (without renormalization)

$$E = -\frac{\hbar c}{2(2\pi)^{D/2}} \int_0^\infty \frac{d\mathcal{T}}{\mathcal{T}^{1+D/2}} \int_{\text{all space}} d\mathbf{x}_0 \times \left\langle\!\!\left\langle \frac{1}{\langle \epsilon_{\text{r}}(\mathbf{x}) \rangle^{1/2}} \right\rangle\!\!\right\rangle_{\mathbf{x}(t)}, \tag{3.1}$$

or equivalently,

$$E = -\frac{\hbar}{(2\pi)^{(D+1)/2}} \int_0^\infty ds \int_0^\infty \frac{d\mathcal{T}}{\mathcal{T}^{(D+1)/2}} \int_{\text{all space}} d\mathbf{x}_0 \times \left\langle\!\!\left\langle e^{-s^2 \mathcal{T} \langle \epsilon_{\text{r}}(\mathbf{x}) \rangle / 2c^2} \right\rangle\!\!\right\rangle_{\mathbf{x}(t)}. \tag{3.2}$$

In these expressions, D is the number of spacetime dimensions, but the temporal dimension has been explicitly removed at this stage. This expression also assumes a dispersion-free dielectric at zero temperature, but it (and the following treatment) are readily generalized to incorporate dispersion and temperature effects [27]. In this expression, the double angle brackets $\langle\!\langle \cdots \rangle\!\rangle$ denote an ensemble average over closed Brownian paths $\mathbf{x}(t)$ (in $D-1$ spatial dimensions) that begin and end at $\mathbf{x}(0) = \mathbf{x}(\mathcal{T}) = \mathbf{x}_0$. The single-angle-bracket notation $\langle \epsilon_{\text{r}}(\mathbf{x}) \rangle$ indicates an average of the relative dielectric permittivity $\epsilon_{\text{r}} := \epsilon/\epsilon_0$ along the path $\mathbf{x}(t)$:

$$\langle \epsilon_{\text{r}} \rangle := \frac{1}{\mathcal{T}} \int_0^{\mathcal{T}} dt\, \epsilon_{\text{r}}[\mathbf{x}(t)]. \tag{3.3}$$

(The ":=" symbol here denotes "is defined to be.") The path increments $d\mathbf{x}(t)$ are Gaussian, with moments $\langle\!\langle d\mathbf{x}(t) \rangle\!\rangle = 0$ and $\langle\!\langle dx_i(t)\, dx_j(t) \rangle\!\rangle = \delta_{ij}\, dt$. The energy in these expressions must still be renormalized by subtracting the zero-body energy (obtained by replacing $\mathbf{x}$ by $\mathbf{x}_0$ in the stochastic average) and the one-body energy (obtained as a limit of widely separated bodies), removing the divergence at $\mathcal{T} = 0$. Physically, the zero-body term represents the energy associated with a uniform dielectric background of permittivity $\epsilon(\mathbf{x}_0)$.

The Casimir–Polder potential for an atom interacting with a dielectric body arises by treating the atom as a localized perturbation to the dielectric, $\epsilon_{\text{r}}(\mathbf{x}) \longrightarrow \epsilon_{\text{r}}(\mathbf{x}) +$

$\alpha_0\delta(\mathbf{x}-\mathbf{x}_0)/\epsilon_0$, and keeping the energy change to linear order in the (static) atomic polarizability α_0. Again, this prescription ignores dispersion and temperature, but such effects are straightforward to include [27]. The resulting path integral following from (3.1) is

$$V_{\text{CP}}(\mathbf{x}_0) = \frac{\hbar c \alpha_0}{4(2\pi)^{D/2}\epsilon_0} \int \frac{d\mathcal{T}}{\mathcal{T}^{1+D/2}} \left\langle\!\!\left\langle \frac{1}{\langle \epsilon_{\text{r}} \rangle^{3/2}} \right\rangle\!\!\right\rangle_{\mathbf{x}(t)}. \tag{3.4}$$

Again, this expression must be renormalized by subtracting the zero-body energy, which amounts to subtracting 1, assuming that the atom is not embedded in a dielectric medium (i.e., $\epsilon_{\text{r}} = 1$ in a neighborhood of $\mathbf{x}_0$). This expression for the Casimir–Polder potential is similar to that of the Casimir energy (3.1), but the potential here is solely a function of paths emanating from the atomic position $\mathbf{x}_0$.

3.2.1 Finite Differences

In path integrals such as Eq. (3.4) for the Casimir–Polder potential, one can compute the Casimir–Polder force $\mathbf{F}_{\text{CP}} = -\nabla E_{\text{CP}}$ by differentiating with respect to the source point $\mathbf{x}_0$ of the paths. A simple, direct way to compute such a gradient numerically is the finite-difference method. In this technique the derivative is computed in terms of the contribution of each path $\mathbf{x}(t)$ and its shifted counterparts of the form $\mathbf{x}(t) + \hat{r}_i\delta$, where δ is a small number, and $\hat{r}_i$ form an orthonormal basis for the configuration space. The simplest finite difference for the first derivative, for example, yields the following path integral for the force, from Eq. (3.4):

$$\begin{aligned}\mathbf{F}(\mathbf{x}_0) = &- \frac{\hbar c \alpha_0}{4(2\pi)^{D/2}\epsilon_0} \sum_i \hat{r}_i \int_0^\infty \frac{d\mathcal{T}}{\mathcal{T}^{1+D/2}} \\ &\times \left\langle\!\!\left\langle \frac{\langle \epsilon_{\text{r}}[\mathbf{x}(t) + \hat{r}_i\delta]\rangle^{-3/2} - \langle \epsilon_{\text{r}}[\mathbf{x}(t)]\rangle^{-3/2}}{\delta} \right\rangle\!\!\right\rangle_{\mathbf{x}(t)}.\end{aligned} \tag{3.5}$$

Unfortunately, as a numerical method this path integral performs poorly. Specifically, in the case of interfaces between regions of otherwise uniform dielectric permittivity, the contribution to the force path integral for a given path $\mathbf{x}(t)$ vanishes except when $\langle \epsilon_{\mathrm{r}} \rangle$ differs for the shifted and original paths $\mathbf{x}(t) + \hat{r}_i \delta$ and $\mathbf{x}(t)$, respectively. Depending on how $\langle \epsilon_{\mathrm{r}} \rangle$ is computed numerically, this difference may vary substantially among the possible paths $\mathbf{x}(t)$ in the limit of small δ. For example, in the limit of an interface between vacuum and a perfect conductor, the contribution for a given path $\mathbf{x}(t)$ vanishes except in the (unlikely) case that $\mathbf{x}(t) + \hat{r}_i \delta$ crosses the interface but $\mathbf{x}(t)$ does not. For small δ, only a small subset of the paths make a nonvanishing contribution to the path integral, and the sample variance diverges as $\delta \longrightarrow 0$. This problem becomes progressively worse when computing additional derivatives. Thus, it is important to consider alternative methods for computing derivatives.

Because of the presence of the $\mathcal{T}$ integral in the path integrals (3.1) and (3.4), it is possible in particular geometries to implement finite differences in a way that avoids the convergence problems noted above. This follows from noting that, for example, in the case of a planar dielectric interface, a shift in the source point of a path is equivalent to a change in the path's running time $\mathcal{T}$, as far as computing $\langle \epsilon_{\mathrm{r}} \rangle$ is concerned. Thus, the finite difference can effectively act on the $\mathcal{T}^{-1-D/2}$ factor instead of the path average. However, the rest of this paper will focus on methods that apply in general geometries and to path averages that lack the $\mathcal{T}$ integral.

3.2.2 Partial Averages in the Vicinity of the Source Point

To handle derivatives with respect to the atomic position in the Casimir–Polder energy (3.4), consider the general, schematic form of the path integral

$$\begin{aligned} I &= \left\langle\!\!\left\langle \Phi[\mathbf{x}(t)] \right\rangle\!\!\right\rangle_{\mathbf{x}(t)} \\ &= \int \prod_{n=1}^{N-1} d\mathbf{x}_n \, P[\mathbf{x}(t)] \, \Phi[\mathbf{x}(t)] \end{aligned} \tag{3.6}$$

in terms of an arbitrary path functional $\Phi[\mathbf{x}(t)]$ and probability measure $P[\mathbf{x}(t)]$ for the paths. The relevant paths for Casimir–Polder energies are closed, Gaussian paths (Brownian bridges) starting and ending at $\mathbf{x}(0) = \mathbf{x}(\mathcal{T}) = \mathbf{x}_0$; in discrete form with N discrete path samples, the probability density for these paths in $D-1$ dimensions is

$$\begin{aligned} P[\mathbf{x}(t)] = (2\pi\Delta\mathcal{T})^{-N(D-1)/2} \, & e^{-(\mathbf{x}_0-\mathbf{x}_{N-1})^2/2\Delta\mathcal{T}} \\ & \times e^{-(\mathbf{x}_0-\mathbf{x}_1)^2/2\Delta\mathcal{T}} \prod_{j=1}^{N-2} e^{-(\mathbf{x}_{j+1}-\mathbf{x}_j)^2/2\Delta\mathcal{T}}, \end{aligned} \tag{3.7}$$

where $\Delta\mathcal{T} = \mathcal{T}/N$. To proceed, we will assume the path functional Φ to be approximately independent of $\mathbf{x}_0$ ($\partial\Phi/\partial\mathbf{x}_0 \approx 0$). This is appropriate, for example, in Casimir–Polder calculations where the dielectric permittivity is constant in the vicinity of the atom (e.g., as in the case of an atom in vacuum, at a finite distance from a dielectric interface). In this case, derivatives of the path integral (3.6) with respect to $\mathbf{x}_0$ act only on the probability density P. For the Gaussian density (3.7),

the derivatives along a particular spatial direction have the form

$$\frac{\partial^n}{\partial x_0^n} P[x(t)] = (\Delta\mathcal{T})^{-n/2} H_n\left(\frac{\bar{x}_1 - x_0}{\sqrt{\Delta\mathcal{T}}}\right) P[x(t)], \tag{3.8}$$

where we are now indicating the spatial dependence in only the relevant direction for notational simplicity, $\bar{x}_1 = (x_1 + x_{N-1})/2$, and the Hermite polynomials H_n are defined according to the convention

$$\frac{d^n}{dx^n} e^{-x^2} = (-1)^n H_n(x)\, e^{-x^2}. \tag{3.9}$$

Note that we have written out the derivatives only for one-dimensional paths to simplify the expressions, but the results here generalize straightforwardly to multiple spatial dimensions (including multiple derivatives in one direction as well as cross-derivatives), in addition to non-Gaussian path measures (e.g., for paths corresponding to more general Lévy processes).

Combining Eq. (3.8) with the path integral (3.6) gives the expression

$$\frac{\partial^n}{\partial x_0^n} I = (\Delta\mathcal{T})^{-n/2} \left\langle\!\!\left\langle H_n\left(\frac{\bar{x}_1 - x_0}{\sqrt{\Delta\mathcal{T}}}\right) \Phi[x(t)] \right\rangle\!\!\right\rangle_{x(t)} \tag{3.10}$$

for the path-integral derivatives. However, this expression is problematic as a numerical derivative estimate because of the factor $\Delta\mathcal{T}^{-n/2}$, which diverges in the continuum limit $\Delta\mathcal{T} \longrightarrow 0$. This factor indicates large sample variances and cancellations between paths in this limit, resulting in inefficient numerical computations.

One approach to ameliorating this problematic behavior comes from the observation that if the path functional Φ is approximately independent of $\mathbf{x}_0$, then

in the limit of large N, Φ will also be approximately independent of neighboring points, such as $\mathbf{x}_1$, $\mathbf{x}_{N-1}$, and other nearby points. In this case, it is possible to carry out the integrals with respect to these points, to obtain a "partially averaged" path integral. (Note that this method is distinct from other partial-averaging methods [51, 52].) Carrying out the integrals over $x_1, \ldots, x_{m-1}$ and $x_{N-k+1}, \ldots, x_{N-1}$, Eq. (3.10) becomes

$$\frac{\partial^n}{\partial x_0^n} I \approx (2\nu_{mk})^{-n/2} \left\langle\!\!\left\langle H_n\left(\frac{\bar{x}_{mk} - x_0}{\sqrt{2\nu_{mk}}}\right) \Phi[x(t)] \right\rangle\!\!\right\rangle_{x(t)}, \tag{3.11}$$

where ν_{mk} and $\bar{x}_{mk}$ are defined by

$$\nu_{mk} := \frac{mk\Delta\mathcal{T}}{m+k} \tag{3.12}$$

$$\bar{x}_{mk} := \frac{kx_m + mx_{N-k}}{m+k}, \tag{3.13}$$

for $k, m \geq 1$. The probability density for the paths in the partially averaged expression (3.11) is

$$\begin{aligned} \bar{P}[x(t)] &:= \int dx_1 \ldots dx_{m-1} dx_{N-k+1} \ldots dx_{N-1}\, P[x(t)] \\ &= e^{-(x_0 - x_{N-k})^2/2k\Delta\mathcal{T}} e^{-(x_0 - x_m)^2/2m\Delta\mathcal{T}} \\ &\quad \times \prod_{j=m}^{N-k-1} e^{-(x_{j+1} - x_j)^2/2\Delta\mathcal{T}}, \end{aligned} \tag{3.14}$$

which has "large steps" from x_0 to x_m and x_{N-k} to x_0. For closed paths, it is generally most sensible to choose $m = k$ to apply the same partial averaging to the beginning

and end of the path, such that $\nu_m := \nu_{mm}$ and $\bar{x}_m := \bar{x}_{mm}$ simplify to

$$\nu_m = \frac{m\Delta\mathcal{T}}{2} = \frac{m\mathcal{T}}{2N} \tag{3.15}$$

$$\bar{x}_m = \frac{x_m + x_{N-m}}{2}, \tag{3.16}$$

and the steps at the beginning and end of the path are equally large on average, as shown schematically (omitting the Brownian nature of the path for visual clarity) in Fig. 3.1.

Since the prefactor in the derivative (3.11) now scales as $\nu_m^{-n/2}$, there is clearly some reduction in the sample variance in a numeric computation as m increases. However, the critical point is this: When chosen appropriately, this prefactor becomes *independent* of N, curing the divergent sample variance in the continuum limit. To choose the number m of points to partially average, the main consideration is that the averaging should not introduce significant error. Returning to the assumption that Φ is approximately independent of $\mathbf{x}_0$, at this point we will have to be somewhat more precise and assume that Φ depends on the path $\mathbf{x}(t)$ via a scalar function $V(\mathbf{x})$ in the form $\Phi[V(\mathbf{x})]$. Then the key assumption is that $V(\mathbf{x})$ is constant (or approximately constant) within a radius d of the source point $\mathbf{x}_0$. The error in averaging over the point $\mathbf{x}_m$, while ignoring the corresponding dependence of Φ, is small so long as there is a small probability for $\mathbf{x}_m$ to leave the constant region. Assuming m will be chosen to be small compared to N, the path from x_0 to x_m (and the corresponding path segment at the end) will behave approximately as an ordinary Wiener path. Since the probability for a one-dimensional Wiener path to cover a distance $d > 0$ from x_0 in time τ is given by

$$P_{\text{cross}} = \operatorname{erfc} \frac{d}{\sqrt{2\tau}}. \tag{3.17}$$

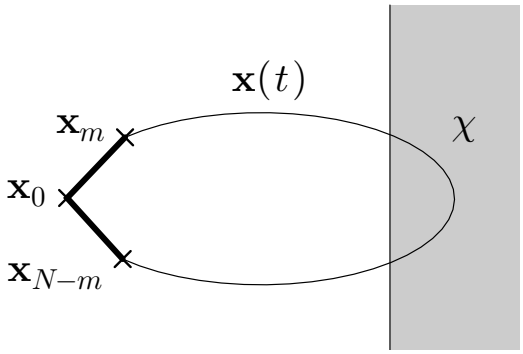

FIGURE 3.1. Schematic path showing partial averaging up to the mth discrete path increment up to and after the source point $\mathbf{x}_0$. The diagram shows the example geometry of the Casimir–Polder potential for an atom in vacuum near a planar interface with a dielectric material of susceptibility χ.

For $\tau \ll d^2$, this expression is bounded above by $e^{-d^2/2\tau}$. Then to keep the error acceptably small, the crossing probability is chosen to be below some small tolerance $\varepsilon > 0$. This condition can be solved to find the total average step time $\tau = m\Delta\mathcal{T}$ such that $P_{\text{touch}} \leq \varepsilon$. The fraction of the path one can acceptably average over is then given by

$$\frac{m}{N} = \frac{d^2}{2\mathcal{T}\ln(1/\varepsilon)}. \tag{3.18}$$

(In practice we choose ε to be much smaller than suggested by this formula.) Note that m/N is constant even as the path resolution N increases, so that the numerical fluctuations, governed by $\nu_m = m\mathcal{T}/2N$, are independent of N, as required. A bound for the numerical error then follows from multiplying the tolerance ε by the amount over which $V(x)$ varies from $\mathbf{x}_0$ to the exterior of the constant region.

These apply readily to the computation of derivatives of the Casimir–Polder potential. For example, the path integral for the Casimir–Polder force becomes

$$\mathbf{F} = \frac{\hbar c \alpha_0}{4(2\pi)^{D/2}} \int \frac{d\mathcal{T}}{\mathcal{T}^{1+D/2}} \left\langle\!\!\left\langle \frac{2\mathbf{x}_0 - \mathbf{x}_m - \mathbf{x}_{N-m}}{m\Delta\mathcal{T}} \right.\right. \\ \left.\left. \times \left(\langle \epsilon_\mathrm{r} \rangle^{-3/2} - [\epsilon_\mathrm{r}(\mathbf{x}_0)]^{-3/2} \right) \right\rangle\!\!\right\rangle_{\mathbf{x}(t)} \tag{3.19}$$

after partial averaging, where an appropriate estimator for the path average of the permittivity is

$$\langle \epsilon_\mathrm{r} \rangle = \frac{1}{N} \left[m\epsilon_\mathrm{r}(\mathbf{x}_0) + \frac{m}{2}\epsilon_\mathrm{r}(\mathbf{x}_m) + \frac{m}{2}\epsilon_\mathrm{r}(\mathbf{x}_{N-m}) \right. \\ \left. + \sum_{j=m+1}^{N-m-1} \epsilon_\mathrm{r}(\mathbf{x}_j) \right]. \tag{3.20}$$

Note that the details of how the points $\mathbf{x}_m$ and $\mathbf{x}_{N-m}$ enter this estimator are not critical, since for small tolerances ε the dielectric permittivity at these points should be equal to the source-point permittivity for the vast majority of paths. Figure 3.1 shows an example of the physical setup for this path integral for an atom near a planar dielectric surface. In evaluating this path integral numerically here, the distance scale d is simply the distance between the atom and the dielectric interface, and a small tolerance ε guarantees that the points x_m and x_{N-m} are unlikely to cross over the interface.

In this differentiated path integral for the force, in principle no renormalization term is required—any renormalization term is independent of the position of the atom, and thus vanishes under the derivative. That is, the $\epsilon_\mathrm{r}(\mathbf{x}_0)$ term in Eq. (3.19) does not ultimately contribute, because it vanishes under the ensemble average for any value of $\mathcal{T}$. However, on a pathwise basis this renormalization term is critical in

a numerical implementation of this path integral, because it cuts off the divergence at $\mathcal{T} = 0$ and dramatically reduces the sample variance of finite ensemble averages, particularly for small $\mathcal{T}$.

3.2.3 Partial Averages Close to One Body

The partial-averaging approach is also useful in computing derivatives in a geometry with two or more material bodies, when the source point of the path integral is close to one of the bodies. This situation applies, for example, when computing the two-body stress-energy tensor in the vicinity of one of the bodies [40, 42, 48], or when extracting the nonadditive, multibody contribution to the Casimir–Polder potential.

As a concrete example, consider differentiating the Casimir–Polder potential of an atom between two dielectric half-spaces, where the atom is close to one interface (Fig. 3.2). In this problem there are two relevant scales for the path running time $\mathcal{T}$: the first time $\mathcal{T}_1$ that the path touches *either* body, and the first time $\mathcal{T}_2$ that the path touches *both* bodies. For the atom at position x_0 between interfaces at positions d_1 and d_2, these times are on the order of $\mathcal{T}_1 \sim (d_1 - x_0)^2$ and $\mathcal{T}_2 \sim (d_2 - d_1)^2$, respectively. If the atom is particularly close to one body, then the dominant contribution to the worldline path integral comes from paths where $\mathcal{T} \sim \mathcal{T}_2 \gg \mathcal{T}_1$. The approach of the previous section is limited in this case, because it relies on the dielectric permittivity being approximately constant in a neighborhood of the source point, with the effectiveness of the method increasing with the radius of this neighborhood. The method thus only effects partial averaging to a limited extent, for $\mathcal{T}_m := m\Delta\mathcal{T} \ll \mathcal{T}_1$.

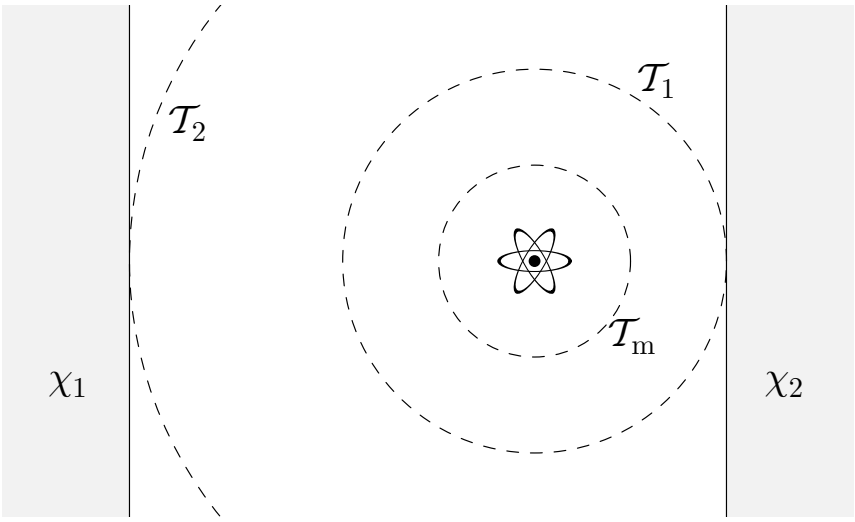

FIGURE 3.2. Schematic of an atom between two dielectric half-spaces with respective susceptibilities χ_1 and χ_2, illustrating the prototype problem for the partial-averaging technique of Section 3.2.3 close to one body. The dashed spheres show the typical extent of the paths at various running times $\mathcal{T}$ (i.e., times over which the paths can diffuse). At $\mathcal{T}_1$ the paths typically touch only the nearer body, while at $\mathcal{T}_2$ they typically touch *both* bodies. The time interval for partial averaging the paths is $\mathcal{T}_m$. The method of Sec. 3.2.2 requires the background dielectric to be approximately uniform in the vicinity of the atom, and thus that $\mathcal{T}_m \ll \mathcal{T}_1$ so that the paths are unlikely to touch either interface during the partial-averaging time. However, because the path integral can be evaluated in the presence of a single, planar interface, the partial averaging can be extended such that $\mathcal{T}_m \sim \mathcal{T}_1$, provided $\mathcal{T}_m \ll \mathcal{T}_2$, so that most paths only hit the nearer interface during the partial-averaging time.

The partial-averaging method extends to this case if there are approximate analytical solutions available for the path integral. As in the case of the TE-polarization path integral [27], it is possible to find analytical solutions for path integrals corresponding to certain material geometries, and then to recast more general worldline path integrals in a form that leverages those solutions. In particular, the (un-renormalized) Casimir–Polder energy can be written as an ensemble average over paths divided into N segments. The ensemble average in the path integral must then include an average over the positions of N points that

define a discrete path, as well as averages over all possible path segments connecting each pair of neighboring points:

$$V_{\rm CP}^{(\rm TE)}(\mathbf{x}_0) = \frac{\hbar c \alpha_0}{(2\pi)^{D/2}\sqrt{\pi}\epsilon_0} \int_0^\infty \frac{d\mathcal{T}}{\mathcal{T}^{1+D/2}} \int_0^\infty ds\, s^2\, e^{-s^2} \times \left\langle\!\!\left\langle \prod_{j=0}^{N-1} \left\langle\!\!\left\langle \exp\left[-\frac{s^2}{\mathcal{T}} \int_{\mathcal{T}_j}^{\mathcal{T}_{j+1}} d\tau\, \chi[\mathbf{x}(\tau)] \right] \right\rangle\!\!\right\rangle_{\Delta x_j} \right\rangle\!\!\right\rangle_{\mathbf{x}(\tau)} . \tag{3.21}$$

Here, the connected-double-angle brackets $\langle\!\langle\ \rangle\!\rangle_{\Delta x_j}$ denote an ensemble average over all bridges between $\mathbf{x}_j$ and $\mathbf{x}_{j+1}$, $\mathcal{T}_j = j\Delta\mathcal{T} = (j/N)\mathcal{T}$, and the dielectric susceptibility for the two bodies is $\chi[\mathbf{x}(\tau)] = \chi_1[\mathbf{x}(\tau)] + \chi_2[\mathbf{x}(\tau)]$. With this ordering of brackets, the averages over all path segments between points $\mathbf{x}_j$ and $\mathbf{x}_{j+1}$ occur for a fixed set of discrete points, and then the average must be taken over all possible discrete paths $\mathbf{x}_j$. The key point of this section is that for simple geometries, such as a single planar interface, it is possible to carry out the average over the path segments analytically. In the example of a single, planar interface, the solution corresponds to the generating function of the sojourn time of a Brownian bridge (see Ref. [27], Appendix B).

For sufficiently small time steps ($\Delta\mathcal{T} \ll \mathcal{T}_2$), the probability for the path to interact with both bodies on a given discrete step j is small, so the path integral over bridges is well-approximated by accounting only for the nearest body. For path increments $\Delta\mathbf{x}_j$ close to the χ_2 body, the path-segment average is then

$$\left\langle\!\!\left\langle e^{-(s^2/\mathcal{T})\int d\tau\,(\chi_1+\chi_2)} \right\rangle\!\!\right\rangle_{\Delta\mathbf{x}_j} \approx \left\langle\!\!\left\langle e^{-(s^2/\mathcal{T})\int d\tau\,\chi_2} \right\rangle\!\!\right\rangle_{\Delta\mathbf{x}_j} . \tag{3.22}$$

The crucial point is that this path integral (including the Gaussian probability measure for the path increment), which we can write as

$$U(\mathbf{x}_j, \mathbf{x}_{j+1}; t) = \frac{e^{-(\mathbf{x}_j - \mathbf{x}_{j+1})^2/2t}}{(2\pi t)^{(D-1)/2}} \left\langle\!\!\left\langle e^{-s^2 \int_0^t d\tau\, \chi[\mathbf{x}(\tau)]/\tau} \right\rangle\!\!\right\rangle_{\Delta \mathbf{x}_j}, \tag{3.23}$$

corresponds to a propagator for an associated diffusion equation [25, 53, 54, 55], so the solutions between adjacent steps can be composed into the solution for a larger, combined step. The partial averaging can then be carried out as in the method of the previous section by composing m steps together. To ensure that the error associated with the partial averaging is small, the probability to touch the more-distant body in time $\mathcal{T}_m = m\mathcal{T}/N$ should remain below some small tolerance ε. In the example of two planar interfaces, this condition has the explicit form

$$\frac{m}{N} = \frac{(d_2 - x_0)^2}{2\mathcal{T} \ln(1/\varepsilon)}, \tag{3.24}$$

using the same argument that led to Eq. (3.18). In more general material geometries, the analytical path integral must also approximate the shape of the nearest body. For example, a smooth but nonplanar interface (e.g., the surface of a spherical body) can be approximated locally by a plane for the purposes of the path-segment average in a given path increment. However, in this case, $\mathcal{T}_m$ is also constrained because the geometric approximation must hold over the typical extent of the path up to time $\mathcal{T}_m$. For example, in a local planar approximation, the distance that paths typically explore in time $\mathcal{T}_m$ must be small on the curvature scale of the interface.

After averaging, the derivatives are readily computed, although in general they will not yield the same Hermite-polynomial weighting factors as in Eq. (3.10):

$$\begin{aligned}\frac{\partial^n}{\partial x_0^n} V_{\mathrm{CP}}^{(\mathrm{TE})}(\mathbf{x}_0) = {} & \frac{\hbar c \alpha_0}{(2\pi)^{D/2}\sqrt{\pi}\epsilon_0} \int_0^\infty \frac{d\mathcal{T}}{\mathcal{T}^{1+D/2}} \int_0^\infty ds\, s^2\, e^{-s^2} \\ & \times \int \prod_{k=m}^{N-m} d\mathbf{x}_k \prod_{j=m}^{N-m-1} U(\mathbf{x}_j, \mathbf{x}_{j+1}; \Delta\mathcal{T}) \\ & \times \frac{\partial^n}{\partial x_0^n} [U(\mathbf{x}_0, \mathbf{x}_m; m\Delta\mathcal{T})\, U(\mathbf{x}_{N-m}, \mathbf{x}_0; m\Delta\mathcal{T})]. \end{aligned} \tag{3.25}$$

As discussed at the end of the previous section, this expression should be renormalized as necessary. Note that in the path integral here, the derivatives act on both the Gaussian path measure and the subaverages over path segments [via the bracketed factor in Eq. (3.23)]. In addition, the functional form of U may vary depending on the local path position $\mathbf{x}_j$, because it should reflect only the presence of the interface nearest $\mathbf{x}_j$. Although the approximate solution near the source point $\mathbf{x}_0$ of the path is crucial for the partial averaging, it is not necessary to use such analytical results for the entire path. For example, one could also use the simpler trapezoidal estimator [27] for the average of the dielectric function around the remainder of the path.

The averaging approach described here helps to improve the sample variance in a numerical average when the source point of the paths is close to an interface, even though the functional integral cannot be treated as approximately constant, as assumed in the previous method of Sec. 3.2.2. Both this and the previous methods of path-averaging described can be thought of as choosing nonuniform time steps in the discrete path. It is important to note, however, that in most path integrals, all of the time steps should be vanishingly small for good accuracy; but in the partially

averaged path integrals here, the "large" first and last steps should be of fixed time step, even in the limit as the remaining step sizes become vanishingly small. Since the derivatives act on the first and last path steps, the sample variance decreases as their respective time steps increase. In order to improve the statistical convergence of the path average, the first and last steps should therefore be as large as possible, while controlling the errors associated with the simplified, approximate integrands. The methods here still allow a high resolution for the middle section of the path, in order to accurately capture the geometry dependence of the path integral.

3.3 Differentiation of Worldline Casimir Energies

Path integrals of the form of Eqs. (3.1) or (3.2) correspond to Casimir energies between macroscopic bodies. The computation of their derivatives requires a different set of methods because they involve an integral over all possible source points for the paths. To compute forces, curvatures of potentials, and torques within this framework, it is necessary to differentiate with respect to generalized coordinates, such as distances and angles between bodies, in contrast to the derivatives with respect to path source points that we considered above. Here we will develop a general method to handle such derivatives of path integrals.

For the purposes of differentiation, the critical component of the Casimir-energy path integral has the form

$$E = \left\langle\!\!\left\langle \Phi\Big[f\Big(\big\langle\chi(\mathbf{x}(t),\mathbf{R}_1,\mathbf{R}_2)\big\rangle\Big)\Big] \right\rangle\!\!\right\rangle_{\mathbf{x}(t)}, \tag{3.26}$$

where Φ is a linear functional of a function f of the path average (3.3) of the susceptibility $\chi(\mathbf{r})$, and where $\mathbf{R}_1$ labels a generalized coordinate of the first body

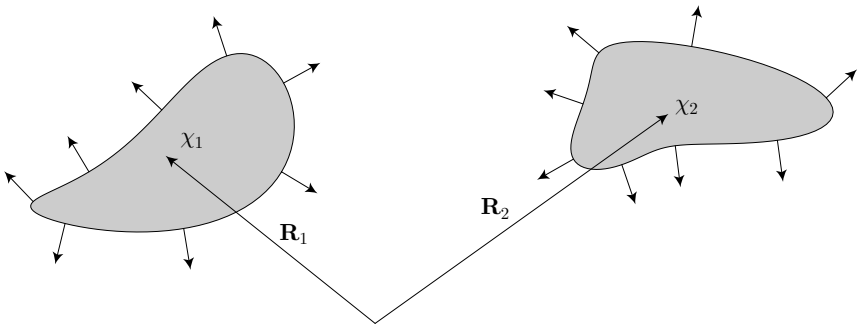

FIGURE 3.3. Geometry for interacting dielectric bodies of susceptibility χ_j, centered at $\mathbf{R}_j$ relative to the origin. The normal vectors $\hat{n}_j$ to the surface of the jth body are also shown.

(or collection of bodies), and $\mathbf{R}_2$ labels a generalized coordinate of the second body (or collection thereof). For example, a typical arrangement is depicted in Fig. 3.3, where uniform dielectric bodies are separated by vacuum, although the treatment here may be straightforwardly generalized to nonuniform dielectric media. In this case, the susceptibility $\chi(\mathbf{r})$ is given generally by

$$\chi(\mathbf{r}) = \sum_j \chi_j \Theta[\sigma_j(\mathbf{r} - \mathbf{R}_j)], \tag{3.27}$$

where χ_j is the dielectric susceptibility of body j; $\sigma_j(\mathbf{r}) = 0$ defines the surface of the jth body, with $\sigma_j > 0$ and $\sigma_j < 0$ on the interior and exterior of the body, respectively; and $\mathbf{R}_j$ is the center of the jth body. The integral still averages over the paths $\mathbf{x}(t)$ via the path average. Recall that Φ depends implicitly on $\mathcal{T}$ via the path statistics, because $\mathbf{x}(0) = \mathbf{x}(\mathcal{T}) = \mathbf{x}_0$.

3.3.1 Force

The force on a body follows from the gradient of the Casimir energy, where the derivatives are taken with respect to the body's position. For example, the force on

body 1 is given by differentiating the path integral in Eq. (3.26) with respect to the body position $\mathbf{R}_1$:

$$\mathbf{F}_1 = -\nabla_{\mathbf{R}_1} E = -\left\langle\!\!\left\langle \frac{\partial \Phi}{\partial f}\, \nabla_{\mathbf{R}_1} f \right\rangle\!\!\right\rangle_{\mathbf{x}(t)}. \tag{3.28}$$

In this expression, $\partial\Phi/\partial f$ is independent of f (since Φ is a linear function of f). In the case where f is exponential, we can divide the path average into two steps: first, averaging over the N discrete, uniform steps $\Delta\mathbf{x}_j := \mathbf{x}_{j+1} - \mathbf{x}_j$, and second, averaging over all the subpaths between $\mathbf{x}_j$ and $\mathbf{x}_{j+1}$:

$$\mathbf{F}_1 = -\left\langle\!\!\left\langle \frac{\partial \Phi}{\partial f}\, \nabla_{\mathbf{R}_1} \prod_{j=0}^{N-1} \langle\!\langle f \rangle\!\rangle_{\Delta\mathbf{x}_j} \right\rangle\!\!\right\rangle_{\mathbf{x}_n}. \tag{3.29}$$

Here the connected-double-angle brackets $\langle\!\langle\ \rangle\!\rangle_{\Delta\mathbf{x}_j}$ denotes an average over all such bridges between $\mathbf{x}_j$ and $\mathbf{x}_{j+1}$, as in Sec. 3.2.3, and the subscript $\mathbf{x}_n$ indicates an average over all discrete paths of N steps. Then applying the derivative to the product of subpaths,

$$\mathbf{F}_1 = -\left\langle\!\!\left\langle \frac{\partial \Phi}{\partial f}\, f \sum_{j=0}^{N-1} \frac{\nabla_{\mathbf{R}_1} \langle\!\langle f \rangle\!\rangle_{\Delta\mathbf{x}_j}}{\langle\!\langle f \rangle\!\rangle_{\Delta\mathbf{x}_j}} \right\rangle\!\!\right\rangle_{\mathbf{x}_n}. \tag{3.30}$$

There are typically N terms here, but if $\langle\!\langle f \rangle\!\rangle_{\Delta\mathbf{x}_j}$ is associated with a sharp surface, then only $O(N^{1/2})$ of them will contribute to the sum. Again, this form of the path integral is specific to an exponential f; for example, Eq. (3.2) is of the form

$$\begin{aligned} f\big(\langle\chi\rangle\big) &= e^{-s^2\mathcal{T}(1+\langle\chi\rangle)/2c^2} \\ \Phi &= -\frac{\hbar}{(2\pi)^{5/2}} \int_0^\infty ds \int_0^\infty \frac{d\mathcal{T}}{\mathcal{T}^{5/2}} \int d\mathbf{x}_0\, f(\langle\chi\rangle), \end{aligned} \tag{3.31}$$

and works with this method. Other path integrals, for example of the form of Eq. (3.1),

$$f(\langle\chi\rangle) = (1+\langle\chi\rangle)^{-1/2} \tag{3.32}$$
$$\Phi = -\frac{\hbar c}{8\pi^2}\int_0^\infty \frac{d\mathcal{T}}{\mathcal{T}^3}\int d\mathbf{x}_0\, f(\langle\chi\rangle),$$

can be handled using the alternate form for the force,

$$\mathbf{F}_1 = -\left\langle\!\!\left\langle \frac{\partial\Phi}{\partial f}\, f' \sum_{j=0}^{N-1} \nabla_{\mathbf{R}_1} \langle\!\langle \chi \rangle\!\rangle_{\Delta\mathbf{x}_j} \right\rangle\!\!\right\rangle_{\mathbf{x}_n}, \tag{3.33}$$

where $\mathcal{T}_j = j\Delta\mathcal{T} = j\mathcal{T}/N$. Qualitatively, the Casimir force on a body arises from paths that pierce its surface, with a vector path weight in the direction of the surface normal at the path source point. Although the surface of an arbitrary body involves surface normals pointing in all directions, each surface normal obtains a different geometry-dependent weight via the path ensemble. The result is, in general, a nonzero net force.

As in Sec. 3.2.2, a partial-averaging procedure accelerates convergence. If one surface is located at d_1, then the condition is

$$(x_{j+1} - d_1)(x_j - d_1) \le \varepsilon \tag{3.34}$$

for a positive tolerance ε [typically $10^4/(N\sqrt{\mathcal{T}})$; note that setting $\varepsilon = 0$ simply detects a surface crossing]. When this condition is satisfied for any boundary, the solution advances forward by $m > 1$ points, and the estimate of the function $\langle\!\langle f \rangle\!\rangle_{\Delta\mathbf{x}_j}$ or the susceptibility $\langle\!\langle \chi \rangle\!\rangle_{\Delta\mathbf{x}_j}$ is calculated with respect to this larger path length.

3.3.2 Potential Curvature

This method can be easily extended to the second derivative of the worldline energy, which yields the potential curvature,

$$C_{ij} := (\hat{r}_i \cdot \nabla_{\mathbf{R}_1})(\hat{r}_j \cdot \nabla_{\mathbf{R}_1})E, \tag{3.35}$$

in basis $\hat{r}_i$. Applying this to the path integral (3.26) gives

$$C_{ij} = \left\langle\!\!\left\langle \frac{\partial \Phi}{\partial f} (\hat{r}_i \cdot \nabla_{\mathbf{R}_1})(\hat{r}_j \cdot \nabla_{\mathbf{R}_1}) \prod_{k=0}^{N-1} \left\langle\!\!\left\langle f \right\rangle\!\!\right\rangle_{\Delta \mathbf{x}_k} \right\rangle\!\!\right\rangle_{\mathbf{x}_n}, \tag{3.36}$$

and applying the derivatives in the case where f is exponential yields

$$\begin{aligned} C_{ij} = \Bigg\langle\!\!\Bigg\langle \frac{\partial \Phi}{\partial f} f \Bigg[\sum_{\substack{\ell,k=0 \\ \ell \neq k}}^{N-1} \frac{\hat{r}_i \cdot \nabla_{\mathbf{R}_1} \left\langle\!\!\left\langle f \right\rangle\!\!\right\rangle_{\Delta \mathbf{x}_\ell}}{\left\langle\!\!\left\langle f \right\rangle\!\!\right\rangle_{\Delta \mathbf{x}_\ell}} \frac{\hat{r}_j \cdot \nabla_{\mathbf{R}_1} \left\langle\!\!\left\langle f \right\rangle\!\!\right\rangle_{\Delta \mathbf{x}_k}}{\left\langle\!\!\left\langle f \right\rangle\!\!\right\rangle_{\Delta \mathbf{x}_k}} \\ + \sum_{k=0}^{N-1} \frac{(\hat{r}_i \cdot \nabla_{\mathbf{R}_1})(\hat{r}_j \cdot \nabla_{\mathbf{R}_1}) \left\langle\!\!\left\langle f \right\rangle\!\!\right\rangle_{\Delta \mathbf{x}_k}}{\left\langle\!\!\left\langle f \right\rangle\!\!\right\rangle_{\Delta \mathbf{x}_k}} \Bigg] \Bigg\rangle\!\!\Bigg\rangle_{\mathbf{x}_n}. \end{aligned} \tag{3.37}$$

However, it is possible to recast one derivative with respect to the other surface,

$$C_{ij} = -\left\langle\!\!\left\langle \frac{\partial \Phi}{\partial f} (\hat{r}_i \cdot \nabla_{\mathbf{R}_2})(\hat{r}_j \cdot \nabla_{\mathbf{R}_1}) \prod_{k=0}^{N-1} \left\langle\!\!\left\langle f \right\rangle\!\!\right\rangle_{\Delta \mathbf{x}_k} \right\rangle\!\!\right\rangle_{\mathbf{x}_n}, \tag{3.38}$$

in which case, applying the derivatives, in the case where f is exponential, and making the approximation $\Delta \mathbf{x}_j \ll d$ for well separated bodies, where d characterizes

the body separation, we obtain

$$C_{ij} \approx -\left\langle\!\!\left\langle \frac{\partial\Phi}{\partial f}\, f \left[\sum_k \frac{\hat{r}_i \cdot \nabla_{\mathbf{R}_2} \langle\!\langle f \rangle\!\rangle_{\Delta\mathbf{x}_k}}{\langle\!\langle f \rangle\!\rangle_{\Delta\mathbf{x}_k}} \right] \right.$$
$$\left. \times \left[\sum_k \frac{\hat{r}_j \cdot \nabla_{\mathbf{R}_1} \langle\!\langle f \rangle\!\rangle_{\Delta\mathbf{x}_k}}{\langle\!\langle f \rangle\!\rangle_{\Delta\mathbf{x}_k}} \right] \right\rangle\!\!\right\rangle_{\mathbf{x}_n} . \tag{3.39}$$

In the general case, where f is any function, in the same approximation we obtain

$$C_{ij} \approx -\left\langle\!\!\left\langle \frac{\partial\Phi}{\partial f}\, f'' \sum_k \hat{r}_i \cdot \nabla_{\mathbf{R}_2} \langle\!\langle \chi \rangle\!\rangle_{\Delta\mathbf{x}_k} \right.$$
$$\left. \times \sum_\ell \hat{r}_j \cdot \nabla_{\mathbf{R}_1} \langle\!\langle \chi \rangle\!\rangle_{\Delta\mathbf{x}_\ell} \right\rangle\!\!\right\rangle_{\mathbf{x}_n} . \tag{3.40}$$

Partial averaging is then carried out as in Sec. 3.3.1.

3.3.3 Torque

The Casimir torque on a body follows in a similar way by considering the energy shift due to a small rotation. Specifically, consider an infinitesimal rotation of body 1 about the point $\mathbf{R}_1$, with axis $\hat{m}$, and through angle ϕ:

$$\chi(\mathbf{r}) = \chi_1 \Theta\big\{\sigma_1[\mathcal{R}(\phi)(\mathbf{r} - \mathbf{R}_1)]\big\} + \chi_2 \Theta[\sigma_2(\mathbf{r} - \mathbf{R}_2)]. \tag{3.41}$$

For a small rotation angle, the rotation matrix has the form

$$\mathcal{R}_{ij}(\phi) = \delta_{ij} - m_k \epsilon_{ijk} \phi + O(\phi^2), \tag{3.42}$$

where δ_{ij} is the Kronecker delta and ϵ_{ijk} is the Levi–Civita symbol; repeated indices are summed throughout this section. The torque for a rotation about axis $\hat{m}$ can be

written as $K_m := \hat{m}\cdot\mathbf{K} = -\partial_\phi E$. The ϕ derivative acts only on the path-averaged dielectric part of the energy integral,

$$\begin{aligned}\partial_\phi\langle\chi\rangle &= \chi_1\big\langle\partial_\phi\mathcal{R}_{ij}(\phi)[\mathbf{x}(t)-\mathbf{R}_1]_j[\hat{r}_i\cdot\nabla\Theta(\sigma_1)]\big\rangle \\ &= -\chi_1\big\langle m_k\epsilon_{kij}[\mathbf{x}(t)-\mathbf{R}_1]_j[\hat{r}_i\cdot\nabla\Theta(\sigma_1)]\big\rangle \\ &= \chi_1\hat{m}\cdot\big\langle[\mathbf{x}(t)-\mathbf{R}_1]\wedge\nabla\Theta(\sigma_1)\big\rangle, \end{aligned} \tag{3.43}$$

where in the last step we introduced the usual vector cross-product $(\mathbf{a}\wedge\mathbf{b})_i = \epsilon_{ijk}a_jb_k$. Substituting this into Eq. (3.26), the resulting path integral for the torque, after dropping the arbitrary axis $\hat{m}$, is

$$\mathbf{K} = \left\langle\!\!\left\langle \frac{\partial\Phi}{\partial f}\,f'\chi_1\sum_{j=0}^{N-1}\Big\langle\!\!\Big\langle\nabla\Theta(\sigma_1)\wedge[\mathbf{x}(t)-\mathbf{R}_1]\Big\rangle\!\!\Big\rangle_{\Delta\mathbf{x}_j}\right\rangle\!\!\right\rangle_{\mathbf{x}(t)} \tag{3.44}$$

This expression for the torque has the intuitive interpretation where the contribution from each surface element is the cross-product of the displacement vector from the rotation center to the surface point with the Casimir force density associated with that surface element.

3.4 Numerical Results

In this section we demonstrate the feasibility and good performance of the above methods for numerically differentiating worldline path integrals. As in previous work [27], the basic Casimir–Polder calculation of an atom interacting with a planar dielectric interface, along with the Casimir energy of two thin, parallel, planar dielectric membranes, will serve as the test cases for these methods.

3.4.1 Partial Averaging

Figure 3.4 demonstrates the utility of the Hermite-weighting method of Eq. (3.11) for computing derivatives of path integrals. The plot shows the results of the numerical evaluation of the path integral (3.4) for the Casimir–Polder potential of an atom near a dielectric half-space, along with the computed spatial derivatives up to the tenth. Since the potential and its derivatives are normalized to the potential in the perfect-conductor limit, the analytic result is distance-independent, and has the same form in each case, given by the expression

$$\eta_{\text{TE}}(\chi) = \frac{1}{6} + \frac{1}{\chi} - \frac{\sqrt{1+\chi}}{2\chi} - \frac{\sinh^{-1}\sqrt{\chi}}{2\chi^{3/2}}, \tag{3.45}$$

as discussed in Ref. [27] (while not completely realistic [56], this model suffices for a numerical test).

Some aspects of the calculations in this figure are worth discussing here. These computations nominally employed $N = 10^5$ points per path. However, at finite N, the error analysis in Ref. [27] indicates that numerical accuracy suffers, particularly at large values of the susceptibility χ, because the finitely sampled path does not have the same "extent" as the same path in the continuum limit. To help maintain accuracy at large χ, the paths employ some limited, finer sampling: the two path intervals on either side of the point closest to the dielectric interface are each sampled with 10^3 more points (see Sec. 2.5.1 for the algorithm to generate these subpaths). This strategy substantially alleviates the major source of sampling error at large χ, while negligibly impacting the computational effort. In terms of the number $m = k$ of partial averages, we make the simplistic choice of choosing a *fixed* value of m for each calculation ($m = 10$, 20, 200, 200, and 500 partial averages were employed for

$n = 1$, 2, 4, 7, and 10 derivatives, respectively), despite the indication of Eq. (3.18) that the number of partial averages should be chosen to be inversely proportional to $\mathcal{T}$ to maintain a controlled error. This is justified by noting that the partial averages can be chosen to have small errors for small values of $\mathcal{T}$, and the effects of the resulting larger error for large values of $\mathcal{T}$ will be suppressed by the factor $\mathcal{T}^{-3}$ in the path integral (3.4). (For high-accuracy evaluation of the path integral, the partial averages should instead be chosen in a $\mathcal{T}$-dependent way.)

Another major numerical challenge that arises in Fig. 3.4 in the case of high-order derivatives comes from the Hermite-polynomial factor in Eq. (3.11). One issue here is that the Hermite polynomial takes on large values for large values of $|\bar{x}_m - x_0|$. But the Gaussian path measure in the path integral only generates such large values rarely. This means that, with ordinary Gaussian paths, rare events make large contributions to the ensemble, leading to poor statistical accuracy in the numerical computations. In these calculations, we employed the direct solution of sampling $\bar{x}_m$ from the Hermite–Gaussian density

$$P_{H_n}(\bar{x}_m) = \frac{\eta_n}{\sqrt{\pi m \Delta\mathcal{T}}} \left| H_n\left(\frac{\bar{x}_m - x_0}{\sqrt{m\Delta\mathcal{T}}}\right)\right| e^{-(\bar{x}_m - x_0)^2/m\Delta\mathcal{T}}, \tag{3.46}$$

where the factor

$$\eta_n^{-1} := \frac{2}{\sqrt{\pi}} \int_0^\infty dx \; |H_n(x)| \; e^{-x^2} \tag{3.47}$$

normalizes the probability distribution. Then a Gaussian deviate δx_m of zero mean and variance $m(1 - 2m/N)\Delta\mathcal{T}/2$ allows the first and last path steps to be generated according to $x_m = \bar{x}_m + \delta x_m$ and $x_{N-m} = \bar{x}_m - \delta x_m$, and the remainder of the path is generated as a Brownian bridge running from x_m to x_{N-m} in time $(N - 2m)\Delta\mathcal{T}$ (see Sec 2.5.1 for the bridge-generating algorithm). With these modified paths, the

path average (3.11) should be modified to read

$$\frac{\partial^n}{\partial x_0^n} I \approx \eta_n^{-1} (m\Delta\mathcal{T})^{-n/2} \left\langle\!\!\left\langle \Phi[\mathbf{x}(t)] \operatorname{sgn}\bigl[H_n(\bar{z})\bigr] \right\rangle\!\!\right\rangle_{H_n}, \tag{3.48}$$

where $\bar{z} := (\bar{x}_m - x_0)/\sqrt{m\Delta\mathcal{T}}$. Because the Hermite polynomial can take either sign, a great deal of cancellation occurs in Eq. (3.48) among the paths, which can again lead to poor statistical performance for high-order derivatives, when the Hermite polynomial has multiple regions of opposing sign. To combat this, for a given path, the path functional can be averaged over multiple values of $\bar{x}_m$ (holding the rest of the path fixed) to effect this cancellation on a pathwise basis. The calculations in Fig. 3.4, used averages over 1, 5, 100, 5000, and 5000 values of $\bar{x}_m$ per path for $n = 1$, 2, 4, 7, and 10 derivatives, respectively, where the $\bar{x}_m$ were sampled from a subrandom (1D van der Corput) sequence to enhance the accuracy of this subaverage.

The numerical performance in Fig. 3.4 is generally quite good, although performance suffers for high-order derivatives. All of the data here represent statistical averages over 10^8 paths (except for $n = 10$ derivatives, which averages over 10^9 paths). The points at a given derivative order n were computed using the same random numbers, so the points within a curve are not statistically independent. The error bars (delimiting one standard error) are invisibly small on the plot, and amount to a relative statistical error of at most 0.2%, 0.5%, 0.7%, 0.8%, 2%, and 2% for $n = 0$, 1, 2, 4, 7, and 10 derivatives, respectively. The observed accuracy of the results is comparable to the standard error in each case except for the 10th derivative, where the observed error is at worst 14%, despite the extra computational effort. However, note that a comparable computation of the 10th derivative via the finite-difference method would be completely unfeasible. For an effective resolution of $N = 10^8$ points per path (with $N = 10^5$ and subsampling of 10^3 points as described above), a length

scale of the order $N^{-1/2} = 10^{-4}$ is appropriate for the finite difference, but this leads to a standard deviation in the path values of the order of 10^{40} relative to the mean.

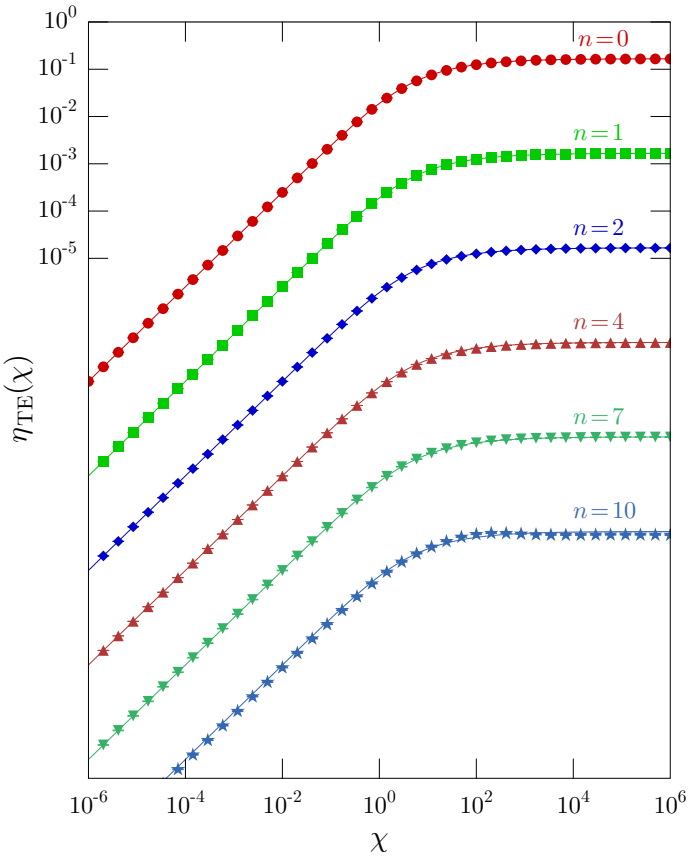

FIGURE 3.4. Numerical evaluation of the path integral (3.4) for the (normalized, dimensionless) Casimir–Polder potential of an atom near a dielectric half-space, as a function of the (dimensionless) dielectric susceptibility χ (data shown as circles). The remaining curves, each successively offset by a factor of 10^{-2} for clarity, show spatial derivatives of the potential according to the method of Eq. (3.11), for $n = 1$ (squares), 2 (diamonds), 4 (triangles), 7 (inverted triangles), and 10 (stars) derivatives. The solid lines give the analytic result (3.45) for comparison in each case. Error bars delimit one standard error. Details of the calculations are given in the text, but the computational difficulty increases with increasing n, and accuracy noticeably suffers by the $n = 10$ case. The same random numbers are used for all the points in the same curve.

3.4.2 *Convergence: Finite Differences vs. Partial Averages*

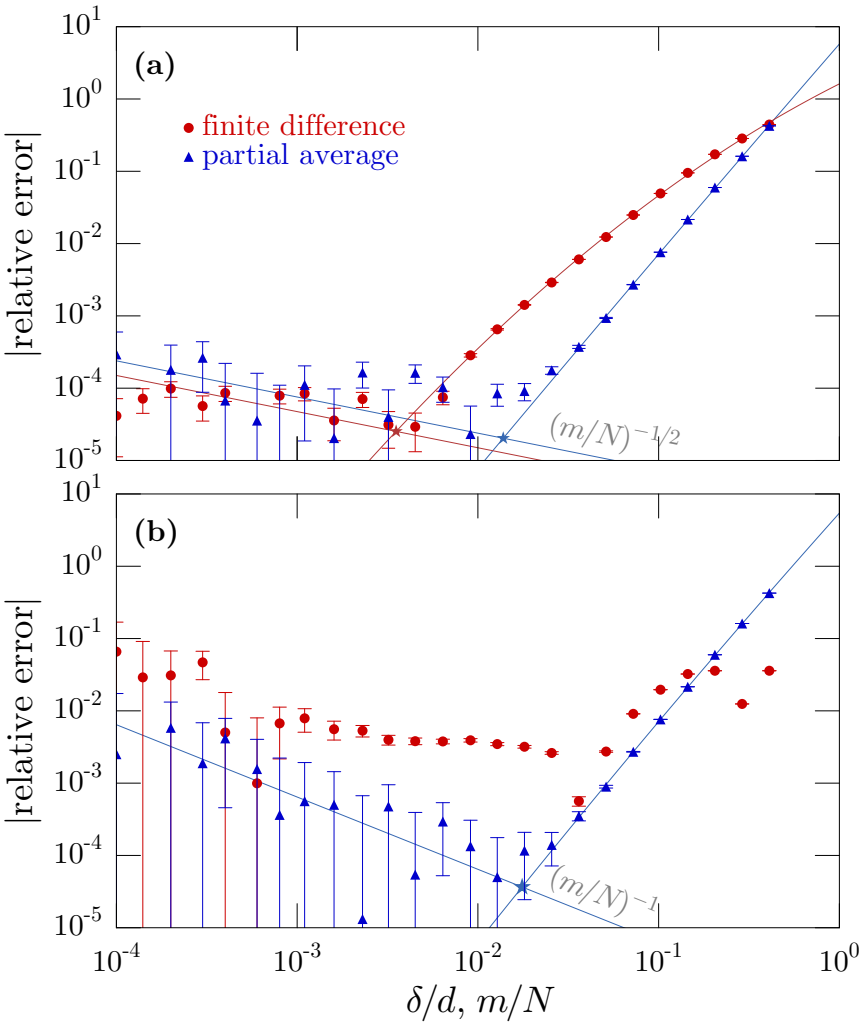

FIGURE 3.5. Magnitude of the relative error in the computation of (a) one spatial derivative and (b) two derivatives of the atom–surface Casimir–Polder potential, for a surface dielectric susceptibility $\chi = 100$. The plots compare the performance of the finite-difference (circles) and partial-averaging (triangles) methods. The finite-difference data are plotted with respect to the spatial displacement δ, normalized to the atom–surface distance d, while the partial-averaging results are plotted as a function of the averaging fraction m/N, where m appears in Eq. (3.16) and N is the number of points per discrete path. The calculations employed paths with $N = 10^4$ points per path, averaging over 10^{11} paths. Error bars delimit one standard error. The lines are fits to the data (except for the second derivative in the finite-difference case), and the intersection (marked by a star) gives the estimated best performance of the method. Data points within each method are statistically independent.

To study the numerical error of the partial-averaging method in more detail, we performed the same calculations as in the previous section for one and two spatial derivatives of the Casimir–Polder potential for an atom near a planar interface, while varying the number m of partial averages (Figs. 3.5 and 3.6). To simplify the analysis, m is held constant (independent of $\mathcal{T}$), ignoring the error-control criterion (3.18). For comparison, the plots also show the corresponding errors when computing the derivatives via finite differences. The first derivative employs the second-order, centered-difference formula $V'_{\mathrm{CP}}(d) = [V_{\mathrm{CP}}(d+\delta) - V_{\mathrm{CP}}(d-\delta)]/2\delta + O(\delta^2)$, where δ is a small spatial displacement. The second derivative exploits the analogous difference formula $V''_{\mathrm{CP}}(d) = [V_{\mathrm{CP}}(d+\delta) - 2V_{\mathrm{CP}}(d) + V_{\mathrm{CP}}(d-\delta)]/\delta^2 + O(\delta^2)$. In implementing the finite-difference methods, it is important to apply these difference formulas on a pathwise basis (or equivalently, apply the difference formulas on ensemble averages over equivalent path samples) for this method to produce any kind of reasonable result. In applying the finite-difference method, the numerical details (path generation, calculation of path averages, etc.) otherwise match those of previous work (see Ref. [27], Sec. V). Although the error for both the partial-averaging and finite-difference methods behaves similarly in the plots, note that the quantities m/N and δ/d from the two methods are not directly comparable. In the partial-averaging method, m sets a length scale $\sqrt{m\Delta\mathcal{T}} = \sqrt{(m/N)\mathcal{T}}$ that varies with $\mathcal{T}$ in the integral in Eq. (3.4). However, it is customary practice for the finite-difference method to use a displacement δ independent of the details of the rest of the calculation, so δ represents a fixed length scale, independent of $\mathcal{T}$. Nevertheless, the plots provide a useful visual comparison of the performance of the two methods.

The performance of the two methods for a dielectric susceptibility $\chi = 100$ (Fig. 3.5) is similar in minimizing the relative error in the case of one derivative.

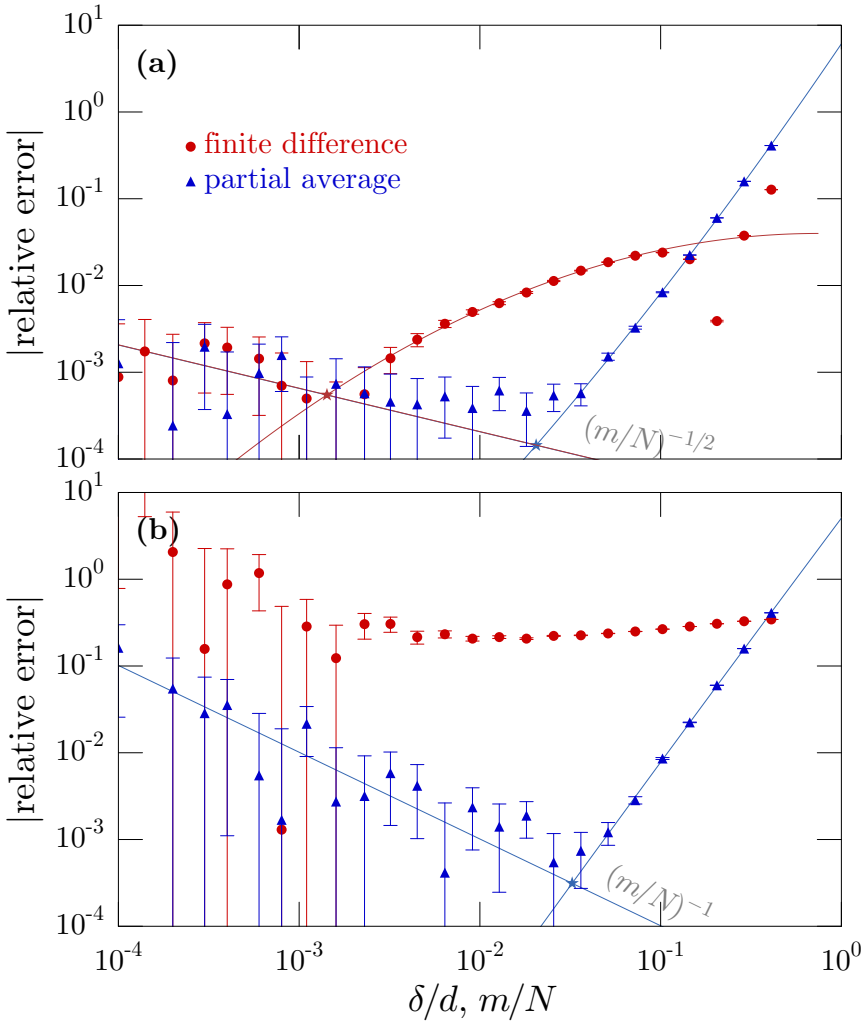

FIGURE 3.6. Magnitude of the relative error in the computation of (a) one spatial derivative and (b) two derivatives of the atom–surface Casimir–Polder potential. The calculations here are similar to those in Fig. 3.5, except here the surface is a perfect conductor ($\chi \longrightarrow \infty$). Also, the calculations here employed paths with $N = 10^6$ points per path (with subpaths of 10^5 points on either side of the point closest to the surface), averaging over 10^9 paths. Other details are as in Fig. 3.5.

However, the partial-averaging method performs clearly better in the two-derivative case. Although $\chi \gg 1$ in this computation, for numerical purposes this calculation is in a "small-χ" regime because $N \gg \chi$ [27]. In terms of the path integral, this means that, in the first-derivative case, when comparing two slightly displaced copies of the same path that overlaps the dielectric interface, the difference in the path-average functional $\langle \epsilon_{\mathrm{r}} \rangle^{-3/2}$ from the path integral (3.4) will be small, of the order $1/N$ for sufficiently small displacements. Finite differences tend to work well when operating on smooth functions, and this is exactly what Fig. 3.5(a) shows: Despite the noisy nature of the paths, the path integral in this regime is relatively well behaved, allowing the finite differences to exhibit performance comparable to that of the partial-averaging method. The clear separation between the methods in Fig. 3.5(b) highlights the better performance of the partial-averaging method for derivatives beyond the first.

Figure 3.5 also shows fits to the data (the range of each fit is shown in Appendix A.3, Table 3.1). On the side of small (δ/d) or (m/N), the data are fit to $a(\delta/d)^{-1/2}$ or $a(m/N)^{-1/2}$ in Fig. 3.5(a), and to $a(m/N)^{-1}$ in Fig. 3.5(b). This reflects the $(\delta/d)^{-n/2}$ or $(m/N)^{-n/2}$ scaling expected of the statistical error in the case of n derivatives [particularly in the latter case, where Eq. (3.11) has a prefactor that scales in this way]. On the side of large (δ/d) or (m/N), the logarithms of the data (on both axes) are fit to a second-order polynomial. The crossings of the corresponding curves are marked by stars, which give the best error expected from the method. The relative errors in the first-derivative methods are both around 2×10^{-5} and the relative error in the second-derivative partial-average method is around 4×10^{-5}. The first-derivative error also exhibits a spurious dip (actually a zero), as noted above, for δ/d near 0.2. However, this does not represent a reliable

error minimum in a more general calculation. Rather, the asymptotic $(\delta/d)^2$ scaling only just becomes visible in a relatively narrow interval (near the center of the interval marked between $\delta/d = 10^{-3}$ and 10^{-1}) before the statistical error takes over. This region represents the true best-case error of this method in this calculation.

The difference in performance between the methods is even more clear in the perfect-conductor ($\chi \longrightarrow \infty$) limit (Fig. 3.6). In both the first- and second-derivative cases the partial-averaging method achieves substantially better accuracy than the finite-difference method. The contrast is particularly striking for the second derivative, where the finite difference achieves a minimum error of around 20%, making the method effectively useless in this regime. (Note that in the finite difference of the first derivative, there is a spurious zero near $\delta/d = 0.2$, as discussed above.) The poor performance of the finite difference is consistent with the argument in the introduction. In the perfect-conductor regime, slightly shifted paths can produce path-functional values that differ by much more than δ—the path-average functional $\langle\epsilon_{\mathrm{r}}\rangle^{-3/2}$ from the path integral (3.4), after renormalization, leads to a null value for paths that do not overlap the interface, but a value of unity for overlapping paths. This leads to large statistical errors in a finite, numerical path average, because finite differences lead to path-functional values switching between zero and δ^{-n} for n derivatives. Also, as is evident in the data, the systematic errors become relatively large in this regime as well, especially in the case of the second derivative. In fact, because we know from prior work [27] that the calculations in the perfect-conductor limit are subject to larger systematic errors than small-χ (i.e., $N \gg \chi$) calculations, we used substantially more points per path in the large-χ calculations ($N = 10^6$ compared to $N = 10^4$ for $\chi = 100$, with the addition here of subpath sampling, using 10^5 points per interval near the path point closest to the surface, as

described in the previous section; to keep the numerical effort comparable in the two cases, the large-χ results average over 10^9 paths, compared to the 10^{11} paths in the $\chi = 100$ case).

The same curve fits were applied in Fig. 3.6 (fit ranges in Appendix A.3, Table 3.1). For the first derivative, the finite-difference best relative error is 5×10^{-4}, while the partial-average best relative error is 1×10^{-4}, a difference of a factor of 5. In the second-derivative case, the partial-average method performs much better than the finite-difference, with a relative error of 3×10^{-4}.

At this point it is worth reiterating one of the main motivations for developing the partial-averaging method for numerical differentiation. The computation of the Casimir–Polder potential in the case of transverse-magnetic (TM) polarization involves the second derivative of a path integral with a path-integral potential that is highly singular at a dielectric interface. Indeed, the TM potential at an interface between finite-χ dielectric materials turns out to be far more pathological than the above behavior of the TE path integral for an interface in the $\chi \longrightarrow \infty$ limit. This pathological behavior is problematic when applying the finite-difference method to the numeric differentiation of the TM path integral. However, as we will show in a future publication, the partial-averaging method is a serviceable alternative method for computing the TM-polarization potential.

3.4.3 Casimir Force and Curvature

The numerical methods of Sec. 3.3 for computing derivatives for Casimir-energy path integrals are similar to the partial-averaging method applied to the Casimir–Polder path integral in the previous section. Figure 3.7 shows the results of such a computation, calculating the Casimir force (first derivative of the Casimir energy)

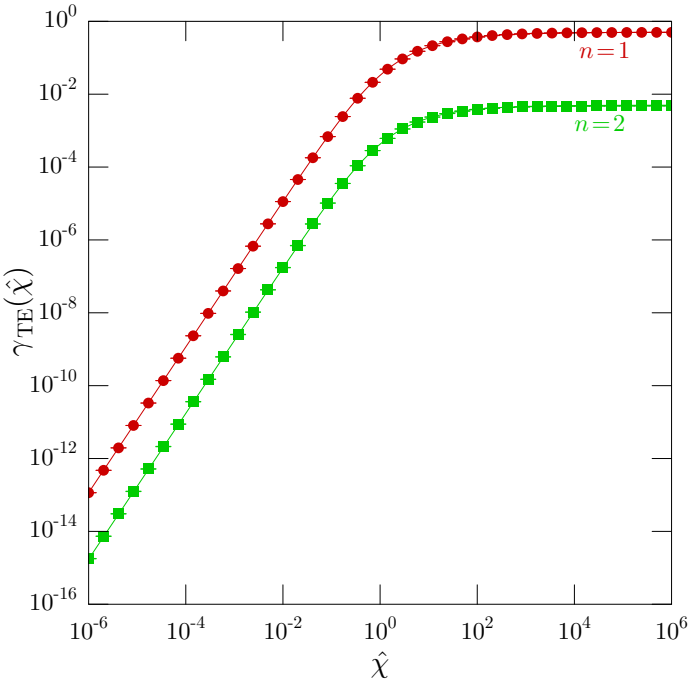

FIGURE 3.7. Numerical evaluation of the derivatives of the path integral (3.2) for the (normalized, dimensionless) Casimir potential of two dielectric thin planes, as a function of the (dimensionless) susceptibility parameter $\hat{\chi}$ (data shown as circles). The first ($n = 1$) derivative is shown (circles) along with the second ($n = 2$) derivative (squares, offset by a factor 10^{-2} for clarity). The solid lines give the derivatives of the analytic result (3.50) for comparison in each case. The calculation used 10^9 paths of 10^5 points per path. Error bars delimit one standard error (on the order of a few times 10^{-4} to a few times 10^{-3} in this plot). The same random numbers are used for the points in each curve.

and the curvature (second derivative of the Casimir energy) between two thin dielectric plates, where the total susceptibility and the relative permittivity are

$$\chi(z) = \hat{\chi}\delta(z) + \hat{\chi}\delta(z-d), \qquad \epsilon_{\mathrm{r}}(z) = 1 + \chi(z). \tag{3.49}$$

Here, viewing the delta-function limit as an idealization of a square profile of a dielectric of finite thickness a, then $\hat{\chi} = \chi a$, where χ is the susceptibility of the medium. The plot compares the numerical data to the exact Casimir force

or curvature. When normalized to the potential in the perfect-conductor limit ($E_{\text{EM}}/A = -\pi^2\hbar c/720d^3$), the Casimir energy has the form

$$\gamma_{\text{TE}}(\chi) = -\frac{180}{\pi^4}\int_0^\infty d\xi\,\xi^2\int_1^\infty dp\,p\ln\bigl(1-r^2e^{-p\xi}\bigr) \tag{3.50}$$

in terms of the Fresnel coefficient $r = -\xi(\hat{\chi}/d)/(2p+\xi\hat{\chi}/d)$. This expression depends on $\hat{\chi}$ and d only in the combination $\hat{\chi}/d$; in the limit $d \gg \hat{\chi}$, this efficiency is $\gamma_{\text{TE}} \approx 27\hat{\chi}^2/4\pi^4d^2$, for a d^{-5} far-field distance dependence, while in the limit $d \ll \hat{\chi}$, the efficiency is $\gamma_{\text{TE}} \approx 1/2$ (i.e., the strong-coupling limit). The data are compared to derivatives of this expression with respect to d.

The numerical method solves the exponential form (3.2) of the path integral; the only error that is not statistical is in treating the two surfaces as independent. That is, the error is in treating the occupation time for each delta-function surface independently, not both surfaces together. This explains the much better performance of the finite-difference method compared to Figs. 3.5 and 3.6. The numerical tests implement Eqs. (3.30) and (3.40), as appropriate for an exponential path integral. The discrete paths over N points are averaged over all subpaths between the points x_{j+1} and x_j; in the one-body approximation, the appropriate quantity is the local time (rather, its generating function) and its derivative, detailed in Appendix A.1.1. Values for $\mathcal{T}$ and s are Monte-Carlo sampled. We also take advantage of the fact that any contributing path must cross any plane between the surfaces. That is, we may start paths midway between the two planes, with a reweighting factor of $N(x_+ - x_-)/2$, where x_+ is the smallest path coordinate such that $x_+ > x_0$ (or just x_0 if no other such point exists), and x_- is the largest path coordinate such that $x_- < x_0$ (or just x_0 if no other such point exists).

The partial-averaging method amounts to looking for path segments that get close enough to the boundaries; details are given in Sec. 3.3.1, particularly Eqs. (3.30), (3.34), and (3.40). Similar to the Casimir–Polder case, renormalization of the one-body energy is necessary to obtain a finite result. For the first derivative, we compute the one-body energy for the undifferentiated surface, and subtract it from the total energy. For the second derivative (3.40), where one derivative is applied to each surface, no renormalization is necessary.

For the finite-difference method, with renormalization of the one-body energies, the path integral has the form

$$I(\mathbf{R}_1, \mathbf{R}_2) = p(\mathbf{R}_1, \mathbf{R}_2) - p_1(\mathbf{R}_1) - p_2(\mathbf{R}_2), \tag{3.51}$$

where p is the two-body energy, p_j is the one-body energy of body j, and $\mathbf{R}_j$ is the position of body j. The first derivative is computed according to a standard, second-order finite difference, which for the z component reads

$$\begin{aligned}\hat{z} \cdot \nabla_{\mathbf{R}_1} I = \frac{1}{2\delta}\Big[&p(\mathbf{R}_1 + \hat{z}\delta, \mathbf{R}_2) - p_1(\mathbf{R}_1 + \hat{z}\delta) \\ &- p(\mathbf{R}_1 - \hat{z}\delta, \mathbf{R}_2) + p_1(\mathbf{R}_1 - \hat{z}\delta)\Big],\end{aligned} \tag{3.52}$$

where δ is some small perturbation. The second derivative is also computed according to a second-order finite difference,

$$\begin{aligned}(\hat{z} \cdot \nabla_{\mathbf{R}_1})^2 I = \frac{1}{\delta^2}\Big[&p(\mathbf{R}_1 + \hat{z}\delta, \mathbf{R}_2) - p_1(\mathbf{R}_1 + \hat{z}\delta) \\ &+ p(\mathbf{R}_1 - \hat{z}\delta, \mathbf{R}_2) - p_1(\mathbf{R}_1 - \hat{z}\delta) \\ &- 2p(\mathbf{R}_1, \mathbf{R}_2) + 2p_1(\mathbf{R}_1)\Big].\end{aligned} \tag{3.53}$$

A better comparison with the partially averaged second derivative is

$$(\hat{z}\cdot\nabla_{\mathbf{R}_1})^2 I = -\frac{1}{4\delta^2}\Big[p(\mathbf{R}_1+\hat{z}\delta,\mathbf{R}_2+\hat{z}\delta) - p(\mathbf{R}_1-\hat{z}\delta,\mathbf{R}_2+\hat{z}\delta) - p(\mathbf{R}_1+\hat{z}\delta,\mathbf{R}_2-\hat{z}\delta) + p(\mathbf{R}_1-\hat{z}\delta,\mathbf{R}_2-\hat{z}\delta)\Big], \tag{3.54}$$

applying one derivative to each interface.

We observe good agreement with the exact results (Fig. 3.7). The calculations employed 10^9 paths, each of 10^5 points per path. The first derivative used partial averaging over 300 points, while the second derivative used 250 points. The relative error in the first derivative ranges from 3.5×10^{-3} for small $\hat{\chi}$ to 4×10^{-4} for large $\hat{\chi}$, and for the second derivative, the relative error ranges from 1.2% at the low end to around 3×10^{-3} at $\hat{\chi}=1$, though the error rises to about 4% for the highest $\hat{\chi}$.

Figures 3.8 and 3.9 show the errors of the partial-average method vs. the finite difference (and in the case of the second derivative, of one finite difference applied to each side). These plots display the relative error vs. the normalized separation δ/d for the finite-difference methods, or the partial-averaging fraction m/N, as described in Sec. 3.3.1. As in Figs. 3.5 and 3.6, the lines for small $\hat{\chi}$ are curve fits to $a(\delta/d)^{-1/2}$ or $a(10m/N)^{-1/2}$ in Figs. 3.8(a) and 3.9(a), and to $a(\delta/d)^{-1/2}$, $a(10m/N)^{-1/2}$, or $a(\delta/d)^{-1}$, as indicated in Figs. 3.8(b) and 3.9(b) (fit ranges indicated in App. A.3, Table 3.2). For large $\hat{\chi}$, the curve fits are second-order polynomials to the log of the data (on both axes). The intersection of the small-$\hat{\chi}$ and large-$\hat{\chi}$ curves is marked with a star, and gives an estimate of the best error of the method. The partial-averaging method outperforms the finite-difference method for the first derivative

in Fig. 3.8(a), for $\hat{\chi} = 1$ (where the best error is 1.5×10^{-4} for partial averaging, vs. 4.9×10^{-4} for finite difference). The partial average still outperforms the finite difference for the second derivative in Fig. 3.8(b), again for $\hat{\chi} = 1$ (where the best error is 1.4×10^{-3} for partial averaging, vs. 4.1×10^{-3} for finite difference, or 2.8×10^{-3} for finite difference, one derivative applied to each side). For $\hat{\chi} = 0.01$ (Fig. 3.9), while the advantage persists for one derivative (where the best error is 5.6×10^{-4} for partial averaging, vs. 1.0×10^{-3} for finite difference); however, for the second derivative, the performance is roughly the same (3.8×10^{-3} for partial averaging, vs. 4.0×10^{-3} for finite difference, or 4.9×10^{-3} for finite difference, one derivative applied to each side). For $\hat{\chi} = 100$ and the $\hat{\chi} \longrightarrow \infty$ limit (both not shown), the methods are comparable in error for both the first and second derivative. So the partial average sometimes performs substantially better than finite differences, and never performs substantially worse. But it should also be appreciated that this partial average method is much faster than finite differences near the optimum value, because of the large time jumps near the surfaces involved.

The method that we have tested here clearly extends to a general geometry. It involves counting the intersections with one (or both) surfaces, and replacing one intersection (or one for each surface) with its derivative. It is thus not geometry specific. The only requirement for partial averaging is that the typical distance covered during a large jump is small compared to a length scale where the nearest surface can be considered flat (assuming that a flat-surface approximation is employed, for example, in a sphere-sphere geometry [57]).

3.5 Summary

We have developed methods for computing derivatives of Casimir–Polder and Casimir-type path integrals. Such derivatives are notable for being difficult to compute using finite differences, because they converge badly—a path only contributes if it marginally touches a surface, but has a large contribution, leading to a large sample variance. For Casimir–Polder-type path integrals, our method involves partial averaging over the region around the atom, which cuts off the sample variance from diverging. For Casimir-type integrals, the method involves counting all intersections with surfaces, and differentiating one of the subpaths. The partial averaging method there involves simply skipping large steps in time, leading to a large gain in computation time. In a future publication, we will apply this method to the Casimir–Polder potential for transverse-magnetic modes, which involves a second derivative.

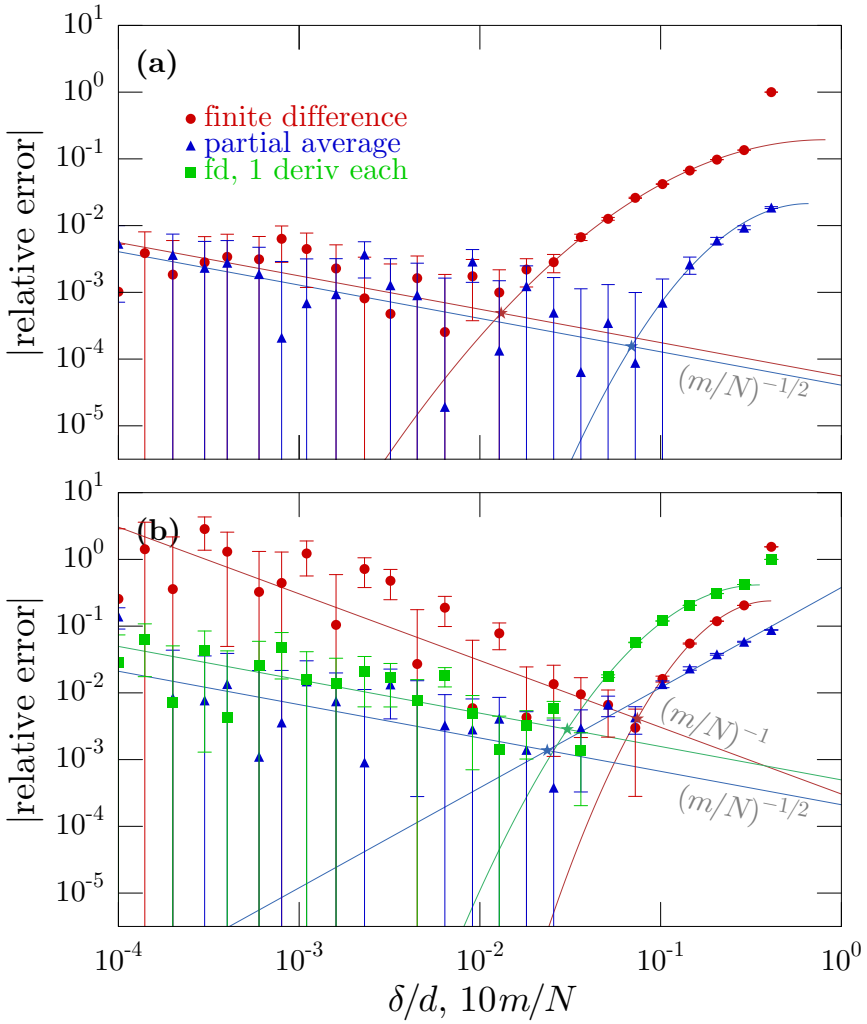

FIGURE 3.8. Magnitude of the relative error in the computation of (a) one spatial derivative and (b) two derivatives of the Casimir potential for two thin planes, for susceptibility parameter $\hat{\chi} = 1$. The plots compare the performance of the finite-difference (circles) and partial-averaging (triangles) methods; the second derivative additionally has one finite difference applied to each surface (squares). The finite-difference data are plotted with respect to the spatial displacement δ, normalized to the atom–surface distance d, while the partial-averaging results are plotted as a function of the averaging fraction m/N, where m appears in Eq. (3.16) and N is the number of points per discrete path. The calculations employed paths with $N = 10^5$ points per path, averaging over 10^9 paths. Error bars delimit one standard error. The lines are fits to the data, and the intersection (marked by a star) gives the estimated best performance of the method. Data points within each method are statistically independent.

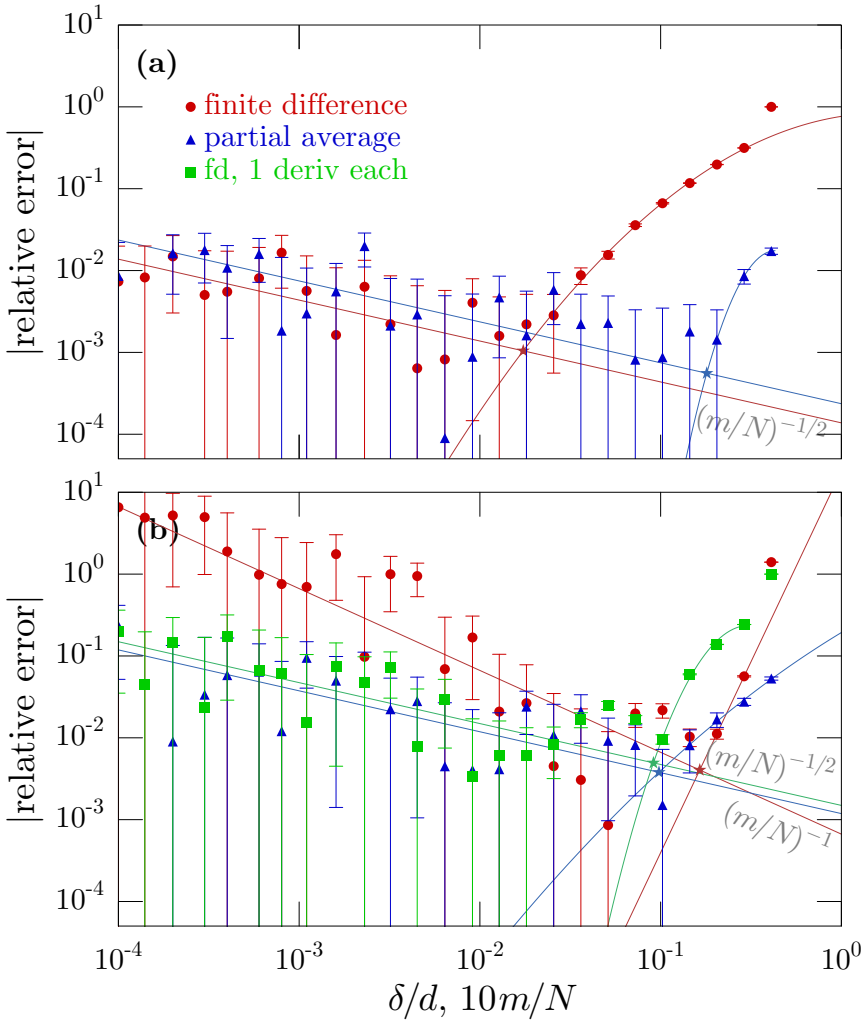

FIGURE 3.9. Magnitude of the relative error in the computation of (a) one spatial derivative and (b) two derivatives of the Casimir potential for 2 thin planes, for susceptibility parameter $\hat{\chi} = 0.01$. Details are as in Fig. 3.8.

Appendix to Chapter III

A.1 Boundary Crossing Statistics

The study of boundary crossing statistics is central to understanding the behavior of stochastic processes near interfaces. These statistics describe various aspects of how a stochastic trajectory interacts with specified thresholds or barriers, including first-passage probabilities, crossing densities, and the distribution of times spent on one side of a boundary.

A central quantity of interest is the *sojourn time* — the total time that the trajectory spends above or below a given level during a fixed observation interval.

Let $y(t)$ be a continuous-time stochastic process, typically a Wiener process or a general diffusion and let $d \in \mathbb{R}$ be a fixed reference level. The sojourn time $T_s[y(t); d]$ of the process $y(t)$ above level d over the interval $[0, t]$ is defined as

$$T_s[y(t); d] := \int_0^t \Theta\big(y(\tau) - d\big)\, d\tau, \tag{3.55}$$

where Θ is the Heaviside step function. Equivalently, T_s measures the cumulative time during which $y(\tau) > d$.

The statistical distribution of the sojourn time T_s depends on the underlying stochastic process $y(t)$ and the boundary geometry of interest. In the special case where the process begins at the boundary, i.e., $a = 0$, and the boundary is fixed at the origin, the distribution of the sojourn time $T_s \in [0, T]$ is given in closed form by the *Lévy arcsine law* [58]:

$$f_{T_s}(s) = \frac{1}{\pi\sqrt{s(T-s)}}, \qquad 0 < s < T. \tag{3.56}$$

This result describes the probability density function (PDF) for the total time s that a Brownian particle, started at the origin, spends in the positive half-line. The divergence of the PDF at both endpoints reflects that paths are more likely to spend nearly all or almost none of the time on one side of the boundary, while an equal-time split is least probable. The cumulative distribution function (CDF) corresponding to Eq. (3.56) is

$$\mathbb{P}(T_s < s) = \frac{2}{\pi} \arcsin\left(\sqrt{\frac{s}{T}}\right), \qquad 0 \le s \le T, \tag{3.57}$$

from which the "arcsine law" terminology originates.

More generally, for Brownian motion starting at $y(0) = a$ and ending at $y(T) = b$, the distribution of the sojourn time above d can be expressed in integral form involving the constrained Brownian paths. Exact expressions exist in terms of error functions but are cumbersome; however, one can compute the moment-generating function

$$\left\langle\!\left\langle e^{-sT_s} \right\rangle\!\right\rangle = \int_0^T e^{-st} f_{T_s}(t)\, dt, \tag{3.58}$$

which simplifies under certain initial and boundary conditions.

The sojourn time is closely related to hitting-time and first-passage observables but differs in that it quantifies cumulative duration rather than the timing of first crossing events. In practical applications — such as path integral Monte Carlo simulations or semiclassical approximations to field-theoretic problems — sojourn times offer a direct route to computing expectation values that depend on spatial occupation. In Casimir physics, for example, sojourn statistics enter naturally when estimating the path-averaged dielectric permittivity in the presence of boundaries or interfaces.

A.1.1 Local Time

In the study of stochastic processes, a key quantity of interest is the amount of time a random trajectory spends in the vicinity of a given spatial location. This is captured by the concept of *local time*, which plays a central role in areas ranging from diffusion processes and path integrals to financial mathematics and quantum field theory.

Let $y(\tau)$ denote a one-dimensional continuous stochastic process (e.g., a Brownian motion or more generally a diffusion process) defined on the interval $\tau \in [0, t]$. The local time $\ell[y(\tau); d]$ at position $d \in \mathbb{R}$ is defined as

$$\ell[y(\tau); d] := \int_0^t d\tau \, \delta\big(y(\tau) - d\big), \tag{3.59}$$

where δ denotes the Dirac delta function. Intuitively, $\ell[y(\tau); d]$ quantifies the cumulative amount of time that the path $y(\tau)$ spends at the position d over the time interval $[0, t]$.

Conceptually, local time is closely related to the sojourn time $T_s[y(\tau); d]$, which measures the total time the process spends above a given threshold (see preceding section). The local time can be expressed as the spatial derivative of the sojourn time:

$$\ell[y(\tau); d] = -\frac{\partial}{\partial d} T_s[y(\tau); d]. \tag{3.60}$$

This relation highlights the role of local time as a density of occupation with respect to space, just as the sojourn time represents an integrated occupation over time.

The local time is a random variable whose distribution can be computed analytically for simple processes. For a Wiener process constrained to start at

$y(0) = a$ and end at $y(t) = b$, the probability density function (PDF) of the local time at position d is given by

$$\begin{aligned} f_\ell(x) = &\left[1 - \exp\left(\frac{(b-a)^2 - (|a-d| + |b-d|)^2}{2t}\right)\right] \delta(x - 0^+) \\ &+ \frac{1}{t}\left(x + |a-d| + |b-d|\right) \\ &\times \exp\left(\frac{(b-a)^2 - (x + |a-d| + |b-d|)^2}{2t}\right), \end{aligned} \tag{3.61}$$

where the singular contribution at $x = 0$ corresponds to trajectories that do not intersect the point d, and the continuous component accounts for all paths with nonzero contact.

For practical computations — particularly in worldline simulations of derivatives of the energy between two thin dielectric planes — one often makes use of the moment generating function of the local time. For the same Brownian bridge between a and b over a duration t, the generating function takes the form

$$\begin{aligned} \left\langle\!\left\langle e^{-s\ell} \right\rangle\!\right\rangle = &1 - \sqrt{\frac{\pi t}{2}}\, s \\ &\times \exp\left[\frac{(b-a)^2 + s^2t^2 + 2st(|a-d| + |b-d|)}{2t}\right] \\ &\times \operatorname{erfc}\left(\frac{|a-d| + |b-d| + st}{\sqrt{2t}}\right), \end{aligned} \tag{3.62}$$

which encodes the full statistics of ℓ, including all its moments and cumulants. This explicit expression, along with its derivative on d, is implemented in the numerical simulations of the worldline differentiation in Sec. 3.4.3.

A.2 Derivation of the TE-Mode Casimir Energy Between Two Thin Delta-Planes

Consider two dielectric planar membranes (thin in thickness) separated by distance d. The spatial dielectric function is then

$$\varepsilon(z) = 1 + \hat{\chi}\delta(z) + \hat{\chi}\delta(z-d), \tag{3.63}$$

where the delta functions represent surface layers of polarization. This description arises as the limiting case of a dielectric slab of finite thickness a and bulk susceptibility χ, with the product

$$\hat{\chi} = \chi a \tag{3.64}$$

held fixed as $a \to 0$. Since the worldline analytic derivation of the Casimir energy is technically intricate, we begin by outlining the key steps of the strategy in concise form below. This roadmap highlights the logical structure of the calculations before presenting the full mathematical derivation.

1. We define the "double local time" of a Brownian path B_t at two spatial points d_0 and $d + d_0$ as

$$l[B_t; d, d_0] = \int_0^t dt' \Big(\delta[B_t(t') - d_0] + \delta[B_t(t') - d - d_0]\Big). \tag{3.65}$$

   This quantity counts, in a distributional sense, the total time the path spends around the two spatial locations.

2. We then construct a path integral of the form

$$L(\lambda, s; d, d_0) = \int_0^\infty \frac{dt}{\sqrt{t}} e^{-\lambda t} \Big\langle\!\Big\langle \exp\Big(- s\, l[B_t; d, d_0]\Big) \Big\rangle\!\Big\rangle_{B_t}, \tag{3.66}$$

which can be obtained by solving the corresponding ODE via the Feynman–Kac formula.

3. The next goal is to construct path integral $I_{D,\alpha}(d, d_0)$ by applying integral transforms of (3.66) on s and λ

$$\begin{aligned} I_{D,\alpha}(d, d_0) &= \int_0^\infty \frac{d\mathcal{T}}{\mathcal{T}^{1+D/2-\alpha}} \Big\langle\!\Big\langle \frac{1}{(\mathcal{T} + \chi l[B_t; d, d_0])^\alpha} - \frac{1}{\mathcal{T}^\alpha} \Big\rangle\!\Big\rangle \\ &= \frac{1}{\Gamma(\alpha)\Gamma[(D - 2\alpha + 1)/2]} \int_0^\infty ds\, s^{\alpha-1} \int_0^\infty d\lambda\, \lambda^{(D-2\alpha-1)/2} \\ &\qquad \times L_{\text{renorm}}(\lambda + s, \chi s; d, d_0), \end{aligned} \tag{3.67}$$

where L_{renorm} is renormalized by properly subtracting contributions from reference configurations.

4. Finally, the Casimir energy of the two-delta-plane configuration is obtained by integrating out x_0.

$$E_{\text{EM}}^{\text{TE}} = -\frac{\hbar c}{2(2\pi)^{D/2}} \int d^{D-2}x_0 \int dd_0\, I_{D,1/2}(d, d_0), \tag{3.68}$$

where the x_0 integral represents the divergent area orthogonal to z.

Following these steps, we start with Eq. (3.66), which can be expressed by solving the ordinary differential equation

$$f''(x) = 2\big[\lambda + s\delta(z) + s\delta(z - d)\big] f(x) - 2e^{ikx}. \tag{3.69}$$

The general solution to this equation is piecewise in three regions

$$f(x) = \begin{cases} Ae^{-\sqrt{2\lambda}x} + \dfrac{e^{ikx}}{\lambda + k^2/2}, & x > d_0 + d \\ Be^{-\sqrt{2\lambda}x} + Ce^{\sqrt{2\lambda}x} + \dfrac{e^{ikx}}{\lambda + k^2/2}, & d_0 < x < d_0 + d \\ De^{\sqrt{2\lambda}x} + \dfrac{e^{ikx}}{\lambda + k^2/2}, & x < d_0 \end{cases} \tag{3.70}$$

and what remains is to match the boundaries. Continuity of $f(x)$ at both boundaries leads to the conditions

$$\begin{aligned} Ae^{-\sqrt{2\lambda}(d_0+d)} &= Be^{-\sqrt{2\lambda}(d_0+d)} + Ce^{\sqrt{2\lambda}(d_0+d)}, \\ Be^{-\sqrt{2\lambda}d_0} + Ce^{\sqrt{2\lambda}d_0} &= De^{\sqrt{2\lambda}d_0}. \end{aligned} \tag{3.71}$$

The δ function in the ODE causes the derivative $f'(x)$ to jump by $2sf(d)$ at each interface, or that is,

$$f'(d_0 - 0^+) = f'(d_0 + 0^+) - 2sf(d_0), \quad f'(d_0 + d - 0^+) = f'(d_0 + d + 0^+) - 2sf(d_0 + d).$$

The condition at $x = d_0 + d$ is

$$\begin{aligned} -\sqrt{2\lambda}Ae^{-\sqrt{2\lambda}(d_0+d)} - 2s\left(Ae^{-\sqrt{2\lambda}(d_0+d)} + \frac{e^{ik(d_0+d)}}{\lambda + k^2/2}\right) \\ = -\sqrt{2\lambda}Be^{-\sqrt{2\lambda}(d_0+d)} + \sqrt{2\lambda}Ce^{\sqrt{2\lambda}(d_0+d)}, \end{aligned} \tag{3.72}$$

and the condition at $x = d_0$ is

$$\sqrt{2\lambda}De^{\sqrt{2\lambda}d_0} + 2s\left(De^{\sqrt{2\lambda}d_0} + \frac{e^{ikd_0}}{\lambda + k^2/2}\right) = -\sqrt{2\lambda}Be^{-\sqrt{2\lambda}d_0} + \sqrt{2\lambda}Ce^{\sqrt{2\lambda}d_0}. \tag{3.73}$$

Solving these four equations and integrating over k gives

$$\begin{aligned}
&\frac{1}{2\pi}\int_{-\infty}^{\infty} dk\, A \\
&= \frac{s}{\sqrt{2\lambda}}\left(\frac{s\, e^{\sqrt{2\lambda}(d_0-d-|d+d_0|)} - \sqrt{2\lambda}e^{\sqrt{2\lambda}(d_0-|d_0|)} - \left(\sqrt{2\lambda}+s\right)e^{\sqrt{2\lambda}(d+d_0-|d_0+d|)}}{(\sqrt{2\lambda}+s)^2 - s^2e^{-2\sqrt{2\lambda}d}}\right) \\
&\frac{1}{2\pi}\int_{-\infty}^{\infty} dk\, B = \frac{s}{\sqrt{2\lambda}}\left(\frac{s\, e^{\sqrt{2\lambda}(d_0-d-|d_0|)} - \left(\sqrt{2\lambda}+s\right)e^{\sqrt{2\lambda}(d_0-|d_0|)}}{(\sqrt{2\lambda}+s)^2 - s^2e^{-2\sqrt{2\lambda}d}}\cdot s^2e^{-2\sqrt{2\lambda}d}\right) \\
&\frac{1}{2\pi}\int_{-\infty}^{\infty} dk\, C = \frac{s}{\sqrt{2\lambda}}\left(\frac{s\, e^{\sqrt{2\lambda}(2d+d_0+|d_0|)} - \left(\sqrt{2\lambda}+s\right)e^{-\sqrt{2\lambda}(d_0+d+|d_0+d|)}}{(\sqrt{2\lambda}+s)^2 - s^2e^{-2\sqrt{2\lambda}d}}\right) \\
&\frac{1}{2\pi}\int_{-\infty}^{\infty} dk\, D \\
&= \frac{s}{\sqrt{2\lambda}}\left(\frac{s\, e^{\sqrt{2\lambda}(2d+d_0+|d_0|)} - \sqrt{2\lambda}e^{-\sqrt{2\lambda}(d_0+d+|d_0+d|)} - \left(\sqrt{2\lambda}+s\right)e^{\sqrt{2\lambda}(d_0+|d_0|)}}{(\sqrt{2\lambda}+s)^2 - s^2e^{-2\sqrt{2\lambda}d}}\right).
\end{aligned} \tag{3.74}$$

Then since we have

$$f(0) = \begin{cases} A + \dfrac{1}{\lambda + k^2/2}, & (0 > d_0 + d) \\ B + C + \dfrac{1}{\lambda + k^2/2}, & (d_0 < 0 < d_0 + d) \\ D + \dfrac{1}{\lambda + k^2/2}, & (0 < d_0) \end{cases} \tag{3.75}$$

and we want to calculate

$$\begin{aligned}
L(\lambda, s; d, d_0) &= \frac{1}{\sqrt{2\pi}}\int_{-\infty}^{\infty} dk\, f(0) \\
&= \int_0^{\infty} \frac{dt}{\sqrt{t}}\, e^{-\lambda t}\left\langle\!\!\left\langle \exp\left(-s\,\delta\big[B_t(t') - d_0\big] - s\,\delta\big[B_t(t') - d_0 - d\big]\right)\right\rangle\!\!\right\rangle_{B_t},
\end{aligned} \tag{3.76}$$

it can be explicitly expressed as

$$L(\lambda, s; d, d_0) = \sqrt{\frac{\pi}{\lambda}} \times \begin{cases} 1 + r_{\text{TE}}(\lambda; s) \dfrac{e^{2\sqrt{2\lambda}(d+d_0)} + [1 + 2r_{\text{TE}}(\lambda; s)]\, e^{2\sqrt{2\lambda}d_0}}{1 - r_{\text{TE}}^2(\lambda; s)\, e^{-2\sqrt{2\lambda}d}}, & (d_0 + d < 0) \\ 1 + r_{\text{TE}}(\lambda; s) \dfrac{2r_{\text{TE}}(\lambda; s)\, e^{-2\sqrt{2\lambda}d} - e^{2\sqrt{2\lambda}d_0} - e^{-2\sqrt{2\lambda}(d+d_0)}}{1 - r_{\text{TE}}^2(\lambda; s)\, e^{-2\sqrt{2\lambda}d}}, & (d_0 < 0 < d_0 + d) \\ 1 + r_{\text{TE}}(\lambda; s) \dfrac{[1 + 2r_{\text{TE}}(\lambda; s)]\, e^{-2\sqrt{2\lambda}(d+d_0)} + e^{-2\sqrt{2\lambda}d_0}}{1 - r_{\text{TE}}^2(\lambda; s)\, e^{-2\sqrt{2\lambda}d}}, & (d_0 > 0) \end{cases} \tag{3.77}$$

where

$$r_{\text{TE}}(\lambda; s) \longrightarrow -\frac{s}{\sqrt{2\lambda} + s} \tag{3.78}$$

is the TE reflection coefficient from a thin, dielectric film.

We define the renormalized quantity L_- as

$$L_-(\lambda, s; d, d_0) := L(\lambda, s; d, d_0) - L_0(\lambda, s), \tag{3.79}$$

where the reference term L_0 is obtained in the limit of $d \to \infty$ and $d_0 \to \pm\infty$ (depending on the region) to move the interfaces arbitrarily far away from the source point. This subtraction removes the geometry-independent baseline, leaving only the

finite contribution due to the presence of the interfaces. Then we obtain

$$L_-(\lambda,s;d,d_0)=\sqrt{\frac{\pi}{\lambda}}$$
$$\times\begin{cases} r_{\rm TE}(\lambda;s)\,\dfrac{e^{2\sqrt{2\lambda}(d+d_0)}+[1+2r_{\rm TE}(\lambda;s)]\,e^{2\sqrt{2\lambda}d_0}}{1-r_{\rm TE}^2(\lambda;s)\,e^{-2\sqrt{2\lambda}d}}, & (d_0+d<0)\\ r_{\rm TE}(\lambda;s)\,\dfrac{2r_{\rm TE}(\lambda;s)\,e^{-2\sqrt{2\lambda}d}-e^{2\sqrt{2\lambda}d_0}-e^{-2\sqrt{2\lambda}(d+d_0)}}{1-r_{\rm TE}^2(\lambda;s)\,e^{-2\sqrt{2\lambda}d}}, & (d_0<0<d_0+d)\\ r_{\rm TE}(\lambda;s)\,\dfrac{[1+2r_{\rm TE}(\lambda;s)]\,e^{-2\sqrt{2\lambda}(d+d_0)}+e^{-2\sqrt{2\lambda}d_0}}{1-r_{\rm TE}^2(\lambda;s)\,e^{-2\sqrt{2\lambda}d}}. & (d_0>0)\end{cases} \tag{3.80}$$

Now, we apply the Laplace–Mellin transform

$$\mathcal{I}_{D,\alpha}(d,d_0)=\frac{1}{\Gamma(\alpha)}\int_0^\infty ds\,s^{\alpha-1}\mathcal{I}_{D-2\alpha}(d,d_0) \tag{3.81}$$

to compute the integral

$$\begin{aligned}\mathcal{I}_{D,\alpha}(d,d_0)&=\int_0^\infty\frac{d\mathcal{T}}{\mathcal{T}^{1+D/2-\alpha}}\left\langle\!\!\left\langle\frac{1}{(\mathcal{T}+\chi\delta[B_\mathcal{T};d,d_0])^\alpha}\right\rangle\!\!\right\rangle\\ &=\frac{2^{3D/2}\Gamma(\alpha)}{\sqrt{\pi}\Gamma\left(\frac{D+1}{2}-\alpha\right)}\int_0^\infty ds\,s^{D/2-1}\int_0^\infty d\lambda\,(\lambda-1)^{(D-1)/2-\alpha}\\ &\quad\times\left[\sqrt{(s/8\pi)}L_-(\lambda s/8,s\chi/8;d,d_0)\right],\end{aligned} \tag{3.82}$$

after letting $\lambda\to\lambda-s$ and then $\lambda\to\lambda s$, and then letting $s\to s/8$. The final Casimir energy should be independent of the reference point d_0, so the next task is to perform the d_0 integral in each regions. We find the sum of contributions from all three regions to be

$$I_I+I_{II}+I_{III}=\frac{2r}{\sqrt{\lambda}[1-r^2e^{-\sqrt{s\lambda}d}]}[(d+\frac{2}{\sqrt{s\lambda}})re^{-\sqrt{s\lambda}d}+\frac{2}{\sqrt{s\lambda}}], \tag{3.83}$$

where $r = r_{\rm TE}(8\lambda; \sqrt{s}\hat{\chi})$. Taking the limit $d \to \infty$,

$$I_0 = \frac{2r}{\sqrt{\lambda}} \frac{2}{\sqrt{s\lambda}} = \frac{4r}{\sqrt{s}\lambda}. \tag{3.84}$$

Again we define the renormalized quantity by removing I_0,

$$\begin{aligned}
&I_I + I_{II} + I_{III} - I_0 \\
&= \frac{2r}{\sqrt{\lambda}[1 - r^2 e^{-\sqrt{s\lambda}d}]}[(d + \frac{2}{\sqrt{s\lambda}})re^{-\sqrt{s\lambda}d} + \frac{2}{\sqrt{s\lambda}}] - \frac{4r}{\sqrt{s}\lambda} \\
&= \frac{2r}{\sqrt{\lambda}[1 - r^2 e^{-\sqrt{s\lambda}d}]}[(d + \frac{2}{\sqrt{s\lambda}})re^{-\sqrt{s\lambda}d} + \frac{2}{\sqrt{s\lambda}}] \\
&\qquad - \frac{2r}{\sqrt{\lambda}[1 - r^2 e^{-\sqrt{s\lambda}d}]}(\frac{2}{\sqrt{s\lambda}}[1 - r^2 e^{-\sqrt{s\lambda}d}]) \\
&= \frac{2r}{\sqrt{\lambda}[1 - r^2 e^{-\sqrt{s\lambda}d}]}[(d + \frac{2}{\sqrt{s\lambda}})re^{-\sqrt{s\lambda}d} + \frac{2}{\sqrt{s\lambda}} - \frac{2}{\sqrt{s\lambda}}(1 - r^2 e^{-\sqrt{s\lambda}d})] \\
&= \frac{2r}{\sqrt{\lambda}[1 - r^2 e^{-\sqrt{s\lambda}d}]}[(d + \frac{2}{\sqrt{s\lambda}})re^{-\sqrt{s\lambda}d} + \frac{2}{\sqrt{s\lambda}} r^2 e^{-\sqrt{s\lambda}d}] \\
&= \frac{2r^2 e^{-\sqrt{s\lambda}d}}{\sqrt{\lambda}[1 - r^2 e^{-\sqrt{s\lambda}d}]}[d + \frac{2 + 2r}{\sqrt{s\lambda}}].
\end{aligned}$$

Using the expression

$$1 + r = \frac{\sqrt{16\lambda}}{\sqrt{16\lambda} + \sqrt{s}\hat{\chi}}, \tag{3.85}$$

the second term in the bracket becomes

$$\frac{2 + 2r}{\sqrt{s\lambda}} = \frac{1}{\sqrt{s\lambda}} \frac{8\sqrt{\lambda}}{\sqrt{16\lambda} + \sqrt{s}\hat{\chi}} = \frac{8}{\sqrt{s}(\sqrt{16\lambda} + \sqrt{s}\hat{\chi})}. \tag{3.86}$$

Multiplying both the numerator and the denominator by $\sqrt{s}$, we obtain

$$\frac{2 + 2r}{\sqrt{s\lambda}} = \frac{8\sqrt{s}}{s(\sqrt{16\lambda} + \sqrt{s}\hat{\chi})} = \frac{-8r}{s\hat{\chi}}. \tag{3.87}$$

Thus, we can rewrite the entire integrand as

$$I_I + I_{II} + I_{III} - I_0 = \frac{2r^2 e^{-\sqrt{s\lambda}d}}{\sqrt{\lambda}[1 - r^2 e^{-\sqrt{s\lambda}d}]}(d - \frac{8r}{s\hat{\chi}}). \tag{3.88}$$

Now recall that we can express the derivative as

$$\partial_\lambda[r^2 e^{-\sqrt{s\lambda}d}] = \frac{1}{2}\sqrt{\frac{s}{\lambda}} r^2 e^{-\sqrt{s\lambda}d}[\frac{8r}{s\hat{\chi}} - d]. \tag{3.89}$$

With this substitution, Eq. (3.88) becomes

$$(I_I + I_{II} + I_{III})_{\text{renorm}} = \frac{-4}{\sqrt{s}} \frac{\partial_\lambda[r^2 e^{-\sqrt{s\lambda}d}]}{[1 - r^2 e^{-\sqrt{s\lambda}d}]} = \frac{-4}{\sqrt{s}} \partial_\lambda \log[1 - r^2 e^{-\sqrt{s\lambda}d}]. \tag{3.90}$$

Finally, all of these terms are related to the Casimir energy per unit area via

$$E^{\text{TE}}_{\text{EM}}/A = -\frac{\hbar c}{2(2\pi)^{D/2}} \int_{-\infty}^{\infty} dd_0 \, I_{D,1/2}(d, d_0), \tag{3.91}$$

where the integral can be written as

$$\begin{aligned} \int_{-\infty}^{\infty} dd_0 \, I_{D,\alpha}(d, d_0) = \frac{\sqrt{\pi}}{2^{3D/2}\Gamma(\alpha)\Gamma[(D+1)/2 - \alpha]} \int_0^{\infty} ds \, s^{D/2-1} \\ \times \int_1^{\infty} d\lambda (\lambda - 1)^{(D-1)/2-\alpha} (I_I + I_{II} + I_{III})_{\text{renorm}}. \end{aligned} \tag{3.92}$$

After taking $\alpha = 1/2$, we obtain

$$\begin{aligned}
&E_{\rm EM}^{\rm TE}/A \\
&= -\frac{\hbar c}{2(16\pi)^{D/2}\Gamma(D/2)} \int_0^\infty ds s^{D/2-1} \int_1^\infty d\lambda (\lambda-1)^{D/2-1} \frac{-4}{\sqrt{s}} \partial_\lambda \log[1 - r^2 e^{-\sqrt{s\lambda}d}] \\
&= \frac{2\hbar c}{(16\pi)^{D/2}\Gamma(D/2)} \int_0^\infty ds s^{D/2-3/2} \int_1^\infty d\lambda (\lambda-1)^{D/2-1} \\
&\qquad \times \partial_\lambda \log[1 - r_{\rm TE}^2(8\lambda; \sqrt{s}\chi) e^{-\sqrt{s\lambda}d}].
\end{aligned} \tag{3.93}$$

Integrating by parts, we reach the general form of the energy density

$$\begin{aligned}
&E_{\rm EM}^{\rm TE}/A \\
&= \frac{(D-2)\hbar c}{(16\pi)^{D/2}\Gamma(D/2)} \int_0^\infty ds s^{D/2-3/2} \int_1^\infty d\lambda (\lambda-1)^{D/2-2} \log[1 - r_{\rm TE}^2(8\lambda; \sqrt{s}\chi) e^{-\sqrt{s\lambda}d}],
\end{aligned} \tag{3.94}$$

where

$$r_{\rm TE}(8\lambda; \sqrt{s}\chi) = -\frac{\sqrt{s}\chi}{\sqrt{16\lambda} + \sqrt{s}\chi}. \tag{3.95}$$

Consider the strong coupling limit in $D = 4$, $\chi \to \infty$ and $r_{\rm TE} \to -1$, the energy density reduces to

$$\begin{aligned}
E_{\rm EM}^{\rm TE}/A &= \frac{2\hbar c}{(16\pi)^2} \int_0^\infty ds \sqrt{s} \int_1^\infty d\lambda \log[1 - e^{-\sqrt{s\lambda}d}] \\
&= -\frac{\pi^2 \hbar c}{1440 d^3}.
\end{aligned} \tag{3.96}$$

The result of large χ is the same as that of the two half dielectric spaces. For finite χ, first we try to scale out distance $s \to s/d^2$

$$\begin{aligned} E_{\text{EM}}^{\text{TE}}/A &= \frac{2\hbar c}{(16\pi)^2}\int_0^\infty ds/d^2\sqrt{s}/d\int_1^\infty d\lambda \log[1-r_{\text{TE}}^2(8\lambda;\sqrt{s}\chi/d)e^{-\sqrt{s\lambda}}] \\ &= \frac{2\hbar c}{(16\pi)^2 d^3}\int_0^\infty ds\sqrt{s}\int_1^\infty d\lambda \log[1-r_{\text{TE}}^2(8d^2\lambda;\sqrt{s}\chi)e^{-\sqrt{s\lambda}}]. \end{aligned} \tag{3.97}$$

This expression is the analytic form of the Casimir energy between two thin membranes that we used in **Chapter III** to benchmark the numerical methods of partial averaging and finite differences. For small χ, $r_{\text{TE}} \approx -\frac{\sqrt{s}\chi}{4d\sqrt{\lambda}}$ to first order in χ. Then, using the expansion $\log(1-x) = -x - x^2/2 - ...$, we obtain

$$\begin{aligned} E_{\text{EM}}^{\text{TE}}/A &= -\frac{\hbar c}{128\pi^2 d^3}\int_0^\infty ds\sqrt{s}\int_1^\infty d\lambda \frac{s\chi^2}{16\lambda d^2}e^{-\sqrt{s\lambda}} \\ &= -\frac{\hbar c\chi^2}{2048\pi^2 d^5}\int_0^\infty ds\sqrt{s}\int_1^\infty d\lambda \frac{s}{\lambda}e^{-\sqrt{s\lambda}} \\ &= -\frac{3\hbar c\chi^2}{320\pi^2 d^5}. \end{aligned} \tag{3.98}$$

So we observe that the weak-coupling result has a d^{-5} dependence.

A.3 Fitting Range and Parameters

TABLE 3.1. Fit ranges for Figs. 3.5 and 3.6.

Figure	Curve Description	Small χ		Large χ	
		Low	High	Low	High
3.5(a)	Finite difference (δ/d)	10^{-4}	4.5×10^{-3}	9.1×10^{-3}	4.096×10^{-1}
3.5(a)	Partial average (m/N)	10^{-4}	4.5×10^{-3}	3.62×10^{-2}	4.096×10^{-1}
3.5(b)	Partial average (m/N)	10^{-4}	1.81×10^{-2}	3.62×10^{-2}	4.096×10^{-1}
3.6(a)	Finite difference (δ/d)	10^{-4}	1.1×10^{-3}	3.2×10^{-3}	7.24×10^{-2}
3.6(a)	Partial average (m/N)	10^{-4}	1.81×10^{-2}	3.62×10^{-2}	4.096×10^{-1}
3.6(b)	Partial average (m/N)	10^{-4}	2.56×10^{-2}	5.12×10^{-2}	4.096×10^{-1}

TABLE 3.2. Fit ranges for Figs. 3.8 and 3.9.

Figure	Curve Description	Small $\hat{\chi}$		Large $\hat{\chi}$	
		Low	High	Low	High
3.8(a)	Finite difference (δ/d)	10^{-4}	9.1×10^{-3}	2.56×10^{-2}	2.897×10^{-1}
3.8(a)	Partial average ($10m/N$)	10^{-4}	5.12×10^{-2}	1.024×10^{-1}	4.096×10^{-1}
3.8(b)	Finite difference (δ/d)	10^{-4}	5.12×10^{-2}	1.024×10^{-1}	2.897×10^{-1}
3.8(b)	Partial average ($10m/N$)	10^{-4}	2.56×10^{-2}	5.12×10^{-2}	4.096×10^{-1}
3.8(b)	FD, 1 derivative each (δ/d)	10^{-4}	2.56×10^{-2}	5.12×10^{-2}	2.897×10^{-1}
3.9(a)	Finite difference (δ/d)	10^{-4}	1.28×10^{-2}	2.56×10^{-2}	2.897×10^{-1}
3.9(a)	Partial average ($10m/N$)	10^{-4}	1.449×10^{-1}	2.048×10^{-1}	4.096×10^{-1}
3.9(b)	Finite difference (δ/d)	10^{-4}	1.024×10^{-1}	2.048×10^{-1}	2.897×10^{-1}
3.9(b)	Partial average ($10m/N$)	10^{-4}	7.24×10^{-2}	1.449×10^{-1}	4.096×10^{-1}
3.9(b)	FD, 1 derivative each (δ/d)	10^{-4}	7.24×10^{-2}	1.024×10^{-1}	2.897×10^{-1}

CHAPTER IV

THE VALIDITY OF SCALAR APPROXIMATION

This work was carried out under the supervision of Daniel A. Steck. I contributed to the mathematical derivations and plotting of the data, and produced most of the paper. The preprint of this work can be found at arXiv:2502.15997.

Throughout this chapter, we restrict our analysis to nonmagnetic atoms, for which the static magnetizability vanishes identically: $\beta_0 = 0$. This assumption is physically well-justified for most atomic and molecular systems of interest and serves to simplify the formalism by eliminating magnetic coupling terms from the interaction energy. Consequently, only electric dipole interactions governed by α_0 contribute to the Casimir–Polder potential.

4.1 Introduction

Casimir–Polder forces generalize van der Waals forces to include boundary conditions and material response [8], and become relevant over distances from tens of nanometers to microns, where retardation and thermal effects emerge. They have been studied in contexts ranging from ultracold atoms near surfaces [31] and MEMS/NEMS devices [30] to atom-optical traps [59, 60]. These forces can be tuned through geometry [61], temperature [6], and material properties [62, 63], enabling new applications in precision sensing and quantum control.

Conventional calculations of Casimir interactions use quantum electrodynamics or Green-function scattering methods [64, 65, 66], but these often require knowledge of system eigenmodes and become impractical for complicated geometries. The worldline path-integral approach offers an efficient alternative. Although the method

is based on scalar field theory and cannot fully capture the vector nature of electromagnetism, scalar models yield accurate results in many settings. They reproduce known Casimir energies for planar geometries [67, 68] and approximate TE and TM contributions in symmetric configurations [27, 40, 42]. Nonetheless, the scalar approximation neglects polarization mixing, and quantifying its limitations remains a key open problem.

This chapter develops the worldline path integral framework for Casimir–Polder interactions involving multiple neutral atoms. After reviewing the QED-based Green tensor formalism, we derive scalar path-integral expressions for two- and three-body energies, generalize to N-body systems, and benchmark against scattering-based results. Emphasis is placed on the scope and limitations of the scalar approximation, and directions for incorporating full electromagnetic dynamics are discussed.

4.2 Green Tensor Calculation of the Casimir–Polder Potential Between Atoms

Recall that Eq. (1.27) describes a single dipole interaction with the field. Now consider a collection of N neutral, nonpolar atoms (or molecules) in vacuum, each located at $\mathbf{r}_i$. These particles possess instantaneous dipoles from linear response to the electromagnetic field. Dispersion interactions arise from the coupling of the dipoles with the field, described by the interaction Hamiltonian

$$\hat{H}_{\text{int}} = -\sum_{i=1}^{N} \hat{\mathbf{d}}_i \cdot \hat{\mathbf{E}}\big(\mathbf{r}_i\big), \tag{4.1}$$

where $\hat{\mathbf{d}}_i$ is the electric dipole operator for the ith particle and $\hat{\mathbf{E}}$ is the quantized electric field operator.

A rigorous foundation for the Casimir interaction between N polarizable atoms in vacuum is furnished by linear response theory, applied to the energy shift induced by atom-field coupling. In this section, we derive the N-body Casimir energy as a trace-logarithmic functional involving the electromagnetic Green tensor.

We model dielectric media microscopically as a discrete collection of N neutral, polarizable atoms located at positions $\{\mathbf{r}_i\}_{i=1}^{N}$ in vacuum. Each atom has a frequency-dependent polarizability tensor $\boldsymbol{\alpha}_i(\omega)$ and responds linearly to the local electric field:

$$\mathbf{d}_i(\omega) = \boldsymbol{\alpha}_i(\omega) \cdot \mathbf{E}(\mathbf{r}_i, \omega). \tag{4.2}$$

The local field $\mathbf{E}(\mathbf{r}_i, \omega)$ at atom i consists of an external field $\mathbf{E}_0(\mathbf{r}_i, \omega)$ plus the field radiated by all dipoles:

$$\mathbf{E}(\mathbf{r}_i, \omega) = \mathbf{E}_0(\mathbf{r}_i, \omega) + \sum_{j=1}^{N} \mathbf{G}^{(0)}(\mathbf{r}_i, \mathbf{r}_j, \omega) \cdot \mathbf{d}_j(\omega), \tag{4.3}$$

where $\mathbf{G}^{(0)}$ is the free-space dyadic Green tensor satisfying

$$\left[\nabla \times \nabla \times - \frac{\omega^2}{c^2}\right] \mathbf{G}^{(0)}(\mathbf{r}, \mathbf{r}', \omega) = \mu_0 \omega^2 \delta^{(3)}(\mathbf{r} - \mathbf{r}'). \tag{4.4}$$

Substituting the field into the dipole response gives a coupled system:

$$\mathbf{d}_i(\omega) = \boldsymbol{\alpha}_i(\omega) \cdot \left[\mathbf{E}_0(\mathbf{r}_i, \omega) + \sum_{j=1}^{N} \mathbf{G}^{(0)}(\mathbf{r}_i, \mathbf{r}_j, \omega) \cdot \mathbf{d}_j(\omega)\right]. \tag{4.5}$$

Let us define a $3N$-dimensional column vector of dipoles

$$\mathbf{d}(\omega) = \begin{pmatrix} \mathbf{d}_1(\omega) \\ \vdots \\ \mathbf{d}_N(\omega) \end{pmatrix}, \quad \mathbf{E}_0(\omega) = \begin{pmatrix} \mathbf{E}_0(\mathbf{r}_1, \omega) \\ \vdots \\ \mathbf{E}_0(\mathbf{r}_N, \omega) \end{pmatrix}, \tag{4.6}$$

a block-diagonal polarizability matrix

$$\boldsymbol{\alpha}(\omega) = \mathrm{diag}\left[\boldsymbol{\alpha}_1(\omega), \ldots, \boldsymbol{\alpha}_N(\omega)\right], \tag{4.7}$$

and a full Green tensor matrix

$$\mathbf{G}^{(0)}(\omega) = \left[\mathbf{G}^{(0)}(\mathbf{r}_i, \mathbf{r}_j, \omega)\right]_{i,j=1}^{N}. \tag{4.8}$$

The system becomes

$$\left[\mathbf{I} - \boldsymbol{\alpha}(\omega) \cdot \mathbf{G}^{(0)}(\omega)\right] \cdot \mathbf{d}(\omega) = \boldsymbol{\alpha}(\omega) \cdot \mathbf{E}_0(\omega), \tag{4.9}$$

whose solution is

$$\mathbf{d}(\omega) = \left[\mathbf{I} - \boldsymbol{\alpha}(\omega) \cdot \mathbf{G}^{(0)}(\omega)\right]^{-1} \cdot \boldsymbol{\alpha}(\omega) \cdot \mathbf{E}_0(\omega). \tag{4.10}$$

This defines the effective collective polarizability of the system:

$$\boldsymbol{\alpha}_{\mathrm{eff}}(\omega) = \left[\mathbf{I} - \boldsymbol{\alpha}(\omega) \cdot \mathbf{G}^{(0)}(\omega)\right]^{-1} \cdot \boldsymbol{\alpha}(\omega). \tag{4.11}$$

We now compute the vacuum energy shift due to the induced interaction by introducing an auxiliary coupling parameter $\lambda \in [0,1]$:

$$\hat{H}_{\rm int}(\lambda) = -\lambda \sum_{n=1}^{N} \hat{\mathbf{d}}_n \cdot \hat{\mathbf{E}}(\mathbf{r}_n). \tag{4.12}$$

The Feynman–Hellmann theorem yields the total energy shift as

$$V_C = \int_0^1 d\lambda \left\langle \lambda \left| \frac{d\hat{H}_{\rm int}(\lambda)}{d\lambda} \right| \lambda \right\rangle = -\sum_{n=1}^{N} \int_0^1 d\lambda \, \langle \hat{\mathbf{d}}_n(\lambda) \cdot \hat{\mathbf{E}}(\mathbf{r}_n) \rangle. \tag{4.13}$$

In analogy to the single-atom Casimir–Polder expression (1.30),

$$V_C = -\frac{\hbar}{2\pi} \int_0^\infty d\xi \int_0^1 \frac{d\lambda}{\lambda} \, \mathrm{Tr} \left[\boldsymbol{\alpha}_{\rm eff}(i\xi;\lambda) \cdot \mathbf{G}^{(0)}(i\xi) \right], \tag{4.14}$$

where the λ-dependent effective polarizability is defined as

$$\boldsymbol{\alpha}_{\rm eff}(i\xi;\lambda) = \left[\mathbf{I} - \lambda \, \boldsymbol{\alpha}(i\xi) \cdot \mathbf{G}^{(0)}(i\xi) \right]^{-1} \cdot \lambda \, \boldsymbol{\alpha}(i\xi). \tag{4.15}$$

To simplify this expression, we use the matrix identity

$$\int_0^1 \frac{d\lambda}{\lambda} \, (\mathbf{I} - \lambda \mathbf{A})^{-1} = \log \, (\mathbf{I} - \mathbf{A})^{-1}, \tag{4.16}$$

valid for any operator $\mathbf{A}$ with spectral norm less than 1. Applying this to the integrand, we arrive at the exact trace-log formula for the Casimir interaction energy among N dipoles in vacuum:

$$V_C = \frac{\hbar}{2\pi} \int_0^\infty d\xi \, \mathrm{Tr} \log \left[\mathbf{I} - \boldsymbol{\alpha}(i\xi) \cdot \mathbf{G}^{(0)}(i\xi) \right]. \tag{4.17}$$

The energy is here expressed as an integral along the imaginary frequency axis. This representation is mathematically equivalent to the real-frequency formalism involving an explicit imaginary part:

$$V_C = \frac{\hbar}{2\pi} \int_0^\infty d\omega \, \mathrm{Im} \, \mathrm{Tr} \log \left[\mathbf{I} - \boldsymbol{\alpha}(\omega) \cdot \mathbf{G}^{(0)}(\omega) \right]. \tag{4.18}$$

The equivalence follows from the analytic properties of the response functions and contour integration in the complex frequency plane. For causal, passive media, the integrand is analytic in the upper half-plane, and the Wick rotation $\omega \to i\xi$ shifts the integration to the imaginary axis, where the Green tensor and polarizability become real and exponentially decaying. The imaginary-frequency formulation is thus both computationally advantageous and rigorously equivalent to the real-frequency approach involving the Im operation.

A formal expansion in powers of the small quantity $\boldsymbol{\alpha} \cdot \mathbf{G}^{(0)}$ gives:

$$V_C = -\frac{\hbar}{2\pi} \int_0^\infty d\omega \, \mathrm{Im} \, \mathrm{Tr} \left[\boldsymbol{\alpha} \cdot \mathbf{G}^{(0)} + \frac{1}{2} (\boldsymbol{\alpha} \cdot \mathbf{G}^{(0)})^2 + \frac{1}{3} (\boldsymbol{\alpha} \cdot \mathbf{G}^{(0)})^3 + \cdots \right]. \tag{4.19}$$

This expansion naturally organizes the Casimir energy into one-body, two-body, and higher-order many-body interactions among the atoms. The first term corresponds to the divergent one-body self-energy of each dipole and is renormalized away. The second term gives the two-body Casimir–Polder potential:

$$V^{(2)} = -\frac{\hbar}{2\pi} \mathrm{Im} \int_0^\infty d\omega \, \frac{1}{2} \sum_{m \neq n} \alpha_0^2 \, G_{ij}^{(0)}(\mathbf{r}_n, \mathbf{r}_m, \omega) \, G_{ji}^{(0)}(\mathbf{r}_m, \mathbf{r}_n, \omega), \tag{4.20}$$

where we have assumed isotropic scalar polarizabilities α_0 and used Einstein summation over repeated indices i, j. Higher-order terms encode genuine many-

body corrections, reflecting the non-additive structure of quantum field-mediated interactions.

In practice, the free-space Green tensor can be expanded in terms of a spectrum of monochromatic plane waves propagating in the $\mathbf{k}$ direction, with $k = \omega/c$. We decompose $\mathbf{k}$ into transverse components (k_x, k_y) and a longitudinal component $k_z = (k^2 - k_x^2 - k_y^2)^{1/2}$, yielding the expression of Green tensor in the plane-wave decomposition,

$$G_{ij}^{(0)}(\mathbf{r}, 0, \omega) = \frac{i}{8\pi^2\varepsilon_0} \int_{-\infty}^{\infty} dk_x \int_{-\infty}^{\infty} dk_y \frac{1}{k_z} (k^2\delta_{ij} + \partial_i\partial_j)\, e^{i(k_x x + k_y y + k_z|z|)}, \tag{4.21}$$

where the source is located at the origin. With $\mathbf{k}$ as the direction of propagation, the projection operator acting on the complex exponential can be expressed as outer products of TE/TM unit vectors as defined relative to $\hat{z}$,

$$G_{ij}^{(0)}(\mathbf{r}, 0, \omega) = \frac{i}{8\pi^2\varepsilon_0} \int_{-\infty}^{\infty} dk_x \int_{-\infty}^{\infty} dk_y \frac{k^2}{k_z} (\hat{e}_i\hat{e}_j + \hat{h}_i\hat{h}_j)\, e^{i(k_x x + k_y y + k_z|z|)}, \tag{4.22}$$

where the TE and TM unit vectors are respectively defined as

$$\begin{aligned} \hat{e} &= \frac{k_y}{k_\rho}\hat{x} - \frac{k_x}{k_\rho}\hat{y} = \frac{\hat{k} \times \hat{z}}{|\hat{k} \times \hat{z}|} \\ \hat{h} &= -\frac{k_z k_x}{k k_\rho}\hat{x} - \frac{k_z k_y}{k k_\rho}\hat{y} + \frac{k_\rho}{k}\hat{z} = \hat{e} \times \hat{k}, \end{aligned} \tag{4.23}$$

and $k_\rho = (k_x^2 + k_y^2)^{1/2}$ denotes the magnitude of the transverse component of the wave vector. The Green tensor now includes contributions from both TE and TM modes [where the electric (TE) or magnetic (TM) field is perpendicular to the z-axis]. When $N = 2$, only one pair of atoms is present, and the interaction energy

contains exactly one term,

$$
\begin{aligned}
V_{\mathrm{CP}} &= -\frac{\hbar\alpha_1\alpha_2}{2\pi}\int_0^\infty ds\,\mathrm{Tr}\left[\mathbf{G}^{(0)}(\mathbf{r}_1,\mathbf{r}_2,is)\cdot\mathbf{G}^{(0)}(\mathbf{r}_2,\mathbf{r}_1,is)\right] \\
&= -\frac{\hbar\alpha_1\alpha_2}{2\pi}\left(\frac{1}{8\pi^2\varepsilon_0}\right)^2\int_0^\infty ds\int_{-\infty}^\infty dk_x\,dk_y\int_{-\infty}^\infty dk_x'\,dk_y' \\
&\quad\times\frac{s^4/c^4}{\kappa(s,k_x,k_y)\kappa(s,k_x',k_y')}\left(\hat{e}_a\hat{e}_b+\hat{h}_a\hat{h}_b\right)\left(\hat{e}_b'\hat{e}_a'+\hat{h}_b'\hat{h}_a'\right) \\
&\quad\times\exp\left[i(k_x(x_1-x_2)+k_y(y_1-y_2))-\kappa(s,k_x,k_y)|z_1-z_2|\right] \\
&\quad\times\exp\left[i(k_x'(x_2-x_1)+k_y'(y_2-y_1))-\kappa(s,k_x',k_y')|z_2-z_1|\right], \qquad (4.24)
\end{aligned}
$$

where the wave vectors satisfy

$$
\begin{aligned}
k &= is/c \\
k_z &= i\sqrt{s^2/c^2+k_x^2+k_y^2}\equiv i\kappa(s,k_x,k_y). \qquad (4.25)
\end{aligned}
$$

Note that this imaginary-frequency form is equivalent, via Wick rotation, to the result in Eq. (4.18). Using the definitions of the TE/TM vectors in Eq. (4.23), the tensor contraction part of this expression is given by

$$
[\hat{e}\hat{e}] = \begin{pmatrix} \frac{k_y^2}{k_\rho^2} & \frac{-k_xk_y}{k_\rho^2} & 0 \\ \frac{-k_xk_y}{k_\rho^2} & \frac{k_x^2}{k_\rho^2} & 0 \\ 0 & 0 & 0 \end{pmatrix} =: [\mathbf{A}_e] \qquad (4.26)
$$

and

$$
[\hat{h}\hat{h}] = \begin{pmatrix} \frac{k_x^2k_z^2}{k_\rho^2k^2} & \frac{k_xk_yk_z^2}{k_\rho^2k^2} & \frac{-k_xk_z}{k^2} \\ \frac{k_xk_yk_z^2}{k_\rho^2k^2} & \frac{k_y^2k_z^2}{k_\rho^2k^2} & \frac{-k_yk_z}{k^2} \\ \frac{-k_xk_z}{k^2} & \frac{-k_yk_z}{k^2} & \frac{k_\rho^2}{k^2} \end{pmatrix} =: [\mathbf{A}_h], \qquad (4.27)
$$

which represent TE and TM contributions, respectively. Note that the tensor contraction in Eq. (4.24) corresponds to tracing the matrix products, with each term given by

$$\begin{aligned}
\mathrm{Tr}(\mathbf{A}_e\mathbf{A}_e'^{\mathrm{T}}) &= \frac{(k_x k_x' + k_y k_y')^2}{k_\rho'^2 k_\rho^2} \\
\mathrm{Tr}(\mathbf{A}_h\mathbf{A}_h'^{\mathrm{T}}) &= \frac{(k_x k_x' k_z k_z' + k_x^2 k_\rho'^2 + k_y k_y' k_z k_z' + k_y^2 k_\rho'^2)^2}{k'^2 k_\rho^2 k^2 k_\rho'^2} \\
\mathrm{Tr}(\mathbf{A}_h\mathbf{A}_e'^{\mathrm{T}}) &= \frac{(k_x' k_y - k_x k_y')^2 k_z^2}{k_\rho^2 k_\rho'^2 k^2} \\
\mathrm{Tr}(\mathbf{A}_e\mathbf{A}_h'^{\mathrm{T}}) &= \frac{(k_x' k_y - k_x k_y')^2 k_z'^2}{k'^2 k_\rho^2 k_\rho'^2}.
\end{aligned} \tag{4.28}$$

The first two terms are pure TE/TM components and the last two terms characterize the mixing between these modes. To further simplify, we assume the two atoms are separated on z-axis, so $x_1 = x_2 = y_1 = y_2 = 0$. By explicitly integrating all k's and the imaginary frequency s, we combine each contribution to obtain

$$\begin{aligned}
&V^{\mathrm{TE}} + V^{\mathrm{TM}} + 2V^{\mathrm{TE/TM}} \\
&= \Big(-\frac{3\hbar c\alpha_1\alpha_2}{16\pi} - \frac{73\hbar c\alpha_1\alpha_2}{16\pi} - \frac{\hbar c\alpha_1\alpha_2}{\pi} \Big) \frac{1}{(4\pi\varepsilon_0)^2 z^7} \\
&= -\frac{23\hbar c\alpha_1\alpha_2}{4\pi} \frac{1}{(4\pi\varepsilon_0)^2 z^7}.
\end{aligned} \tag{4.29}$$

This result is consistent with the full Casimir–Polder potential derived using alternative formalisms; see, for example, Refs. [29, 65].

The preceding calculation extends naturally to the case of three atoms ($N = 3$). The complete derivation is provided in Appendix 4.5. Consider three atoms aligned along the z-axis at positions z_1, z_2, and z_3, equally spaced by a distance $R/2$, thereby forming a collinear configuration. The total interaction energy includes the pairwise

two-body potentials among all three atom pairs, along with an irreducible three-body contribution proportional to the product $\alpha_1\alpha_2\alpha_3$. This three-body energy can be expressed in terms of products of Green tensors as

$$V_{\mathrm{CP}}(z_1,z_2,z_3) = -\frac{\hbar}{2\pi}\int_0^\infty ds\,\mathrm{Tr}\Big[\alpha_1\mathbf{G}_{12}^{(0)}\cdot\alpha_2\mathbf{G}_{23}^{(0)}\cdot\alpha_3\mathbf{G}_{31}^{(0)} + \alpha_1\mathbf{G}_{13}^{(0)}\cdot\alpha_2\mathbf{G}_{21}^{(0)}\cdot\alpha_3\mathbf{G}_{32}^{(0)}\Big]. \tag{4.30}$$

The three-body cross interaction formally consists of $3! = 6$ terms, corresponding to all possible permutations of dipole interactions among the three atoms. However, due to the cyclic invariance of the trace and the symmetry properties of the Green tensors, only two of these terms are distinct. The remaining permutations yield equivalent contributions under the trace. As a result, the combinatorial factor $\frac{1}{3}$ that appears explicitly in Eq. (4.19) is implicitly absorbed through this symmetry reduction. Evaluating Eq. (4.30) for the collinear configuration ultimately gives

$$V_{\mathrm{CP}}(R) = -186\frac{\hbar c\alpha_1\alpha_2\alpha_3}{\pi}\frac{1}{(4\pi\varepsilon_0)^3R^{10}}. \tag{4.31}$$

Again, this result is in agreement with the known analytic expression for three-body Casimir–Polder interactions derived in Ref. [65]. Compared to the $N = 2$ case, the three-body configuration exhibits qualitatively richer behavior due to the non-additive nature of quantum field-mediated forces. As a representative example, consider three identical atoms arranged in an equilateral triangle of side length R. For this geometry, the three-body interaction energy evaluates to

$$V_{\mathrm{CP}}(R) = +5.2\frac{\hbar c\alpha_1\alpha_2\alpha_3}{\pi}\frac{1}{(4\pi\varepsilon_0)^3R^{10}}. \tag{4.32}$$

Notably, this result features a positive sign, indicating a repulsive three-body contribution. In contrast to the two-body Casimir–Polder force — which is universally attractive — the three-body interaction may be either attractive or repulsive depending on the spatial configuration of the atoms. This sensitivity to geometry arises from interference among the multiple scattering paths mediated by the electromagnetic field. By working directly with the full tensorial Green functions in vacuum, this formulation accurately captures the polarization structure and non-pairwise correlations inherent to many-body dispersion forces.

4.3 Multi-Atom Generalization of Scalar Worldlines

As discussed in the previous chapters, the worldline formalism has proven particularly effective in scalar representations of quantum electrodynamics, where it captures key aspects of fluctuation-induced interactions through a computationally efficient path-integral framework. In the context of wave propagation, scalar models can approximate vector field behavior in the paraxial regime, particularly when field polarization remains approximately conserved during propagation. Such approximations are especially justified in systems exhibiting planar or cylindrical symmetry, where the electromagnetic field naturally decomposes into independent transverse-electric (TE) and transverse-magnetic (TM) polarization modes. Each of these modes satisfies a scalar Helmholtz equation, enabling the use of scalar Green functions to represent the propagator and compute the corresponding field partition function. This in turn yields the free energy and Casimir interaction forces in a tractable form.

In this section, we begin by formulating the two-body interaction energy between polarizable particles within the scalar worldline approximation. We demonstrate

that in this simple geometry, the scalar model provides quantitatively accurate results when compared to the full vectorial theory. The analysis is then extended to include three-body and more general N-body interactions among discrete polarizable particles. This allows us to probe the structure of non-additive dispersion forces in settings where geometric symmetry is reduced. Our results develop the scalar worldline expressions of inter-atomic Casimir–Polder potentials to arbitrary number of atoms, and show that the scalar approximation fails to capture essential features of polarization mixing that arise in three-body geometries. This breakdown underscores the limitations of scalar worldline methods and motivates the development of fully vectorial worldline formulations capable of capturing the complete polarization structure of Casimir and Casimir–Polder interactions.

4.3.1 TE Mode

The simplest case starts with developing the worldline expression for two-atom Casimir–Polder potential. Introducing the atoms as small variation $\delta\varepsilon_r$, the variation in energy up to second order is then

$$\delta E_{\text{EM}} = E[\varepsilon + \delta\varepsilon] - E[\varepsilon] \tag{4.33}$$

$$= \int d^{D-1}r \frac{\delta E}{\delta\varepsilon(\mathbf{r})}\delta\varepsilon(\mathbf{r}) + \frac{1}{2}\int d^{D-1}r \int d^{D-1}r' \frac{\delta^2 E}{\delta\varepsilon(\mathbf{r})\delta\varepsilon(\mathbf{r}')}\delta\varepsilon(\mathbf{r})\delta\varepsilon(\mathbf{r}'), \tag{4.34}$$

where the perturbation due to the two atoms located at $\mathbf{r}_1, \mathbf{r}_2$ with polarizability α_1, α_2 can be described as

$$\delta\varepsilon_r(\mathbf{r}) = \frac{\alpha_1}{\varepsilon_0}\delta^{D-1}(\mathbf{r}-\mathbf{r}_1) + \frac{\alpha_2}{\varepsilon_0}\delta^{D-1}(\mathbf{r}-\mathbf{r}_2). \tag{4.35}$$

The first functional derivative can be calculated as

$$\begin{aligned}\frac{\delta E}{\delta\varepsilon_r(\mathbf{r})} &= \frac{\delta}{\delta\varepsilon_r(\mathbf{r})}\Big[-\frac{\hbar c}{2(2\pi)^{D/2}}\int_0^\infty \frac{d\mathcal{T}}{\mathcal{T}^{1+D/2}}\int d^{D-1}x_0\Big\langle\!\Big\langle \langle\varepsilon_r(\mathbf{x})\rangle_{\mathbf{x}(\tau)}^{-1/2}\Big\rangle\!\Big\rangle_{\mathbf{x}(\tau)}\Big] \\ &= -\frac{\hbar c}{2(2\pi)^{D/2}}\int_0^\infty \frac{d\mathcal{T}}{\mathcal{T}^{1+D/2}}\int d^{D-1}x_0\Big\langle\!\Big\langle \frac{-1}{2}\langle\varepsilon_r(\mathbf{x})\rangle_{\mathbf{x}(\tau)}^{-3/2}\frac{\delta\langle\varepsilon_r(\mathbf{x})\rangle}{\delta\varepsilon_r(\mathbf{r})}\Big\rangle\!\Big\rangle_{\mathbf{x}(\tau)}, \quad (4.36)\end{aligned}$$

where

$$\begin{aligned}\frac{\delta\langle\varepsilon_r(\mathbf{x})\rangle}{\delta\varepsilon_r(\mathbf{r})} &= \frac{1}{\mathcal{T}}\int_0^{\mathcal{T}}\frac{\delta\varepsilon_r(\mathbf{x}(t))}{\delta\varepsilon(\mathbf{r})}dt \quad (4.37)\\ &= \frac{1}{\mathcal{T}}\int_0^{\mathcal{T}}\delta^{D-1}(\mathbf{x}(t)-\mathbf{r})dt. \quad (4.38)\end{aligned}$$

Together with $\delta\varepsilon$,

$$\frac{\alpha_1}{\varepsilon_0}\int d^{D-1}r\delta(\mathbf{r}-\mathbf{r}_1)\Big[\frac{1}{\mathcal{T}}\int_0^{\mathcal{T}}\delta^{D-1}(\mathbf{x}(t)-\mathbf{r})dt\Big] = \frac{\alpha_1}{\varepsilon_0}\frac{1}{\mathcal{T}}\int_0^{\mathcal{T}}\delta^{D-1}(\mathbf{x}(t)-\mathbf{r}_1)dt. \quad (4.39)$$

Therefore, the full 1st-order result for the Casimir–Polder potential with the presence of two atoms near a dielectric environment is

$$\begin{aligned}V_{\text{CP}}(\mathbf{r}_1,\mathbf{r}_2) = &\frac{\hbar c\alpha_1}{4(2\pi)^{D/2}\varepsilon_0}\int_0^\infty\frac{d\mathcal{T}}{\mathcal{T}^{1+D/2}}\int d^{D-1}x_0\Big\langle\!\Big\langle\frac{\int_0^T dt\delta^{D-1}[\mathbf{x}(t)-\mathbf{r}_1]}{\mathcal{T}\langle\varepsilon_r(\mathbf{x})\rangle_{\mathbf{x}(\tau)}^{3/2}}\Big\rangle\!\Big\rangle_{\mathbf{x}(\tau)} \\ &+\frac{\hbar c\alpha_2}{4(2\pi)^{D/2}\varepsilon_0}\int_0^\infty\frac{d\mathcal{T}}{\mathcal{T}^{1+D/2}}\int d^{D-1}x_0\Big\langle\!\Big\langle\frac{\int_0^T dt\delta^{D-1}[\mathbf{x}(t)-\mathbf{r}_2]}{\mathcal{T}\langle\varepsilon_r(\mathbf{x})\rangle_{\mathbf{x}(\tau)}^{3/2}}\Big\rangle\!\Big\rangle_{\mathbf{x}(\tau)}. \quad (4.40)\end{aligned}$$

By shifting the path's origin to the atomic positions, the delta functions are evaluated, and we obtain

$$V_{\text{CP}}(\mathbf{r}_1,\mathbf{r}_2)=\frac{\hbar c\alpha_1}{4(2\pi)^{D/2}\varepsilon_0}\int_0^\infty\frac{d\mathcal{T}}{\mathcal{T}^{1+D/2}}\left\langle\!\!\left\langle\langle\varepsilon_r(\mathbf{x})\rangle_{\mathbf{x}(\tau)}^{-3/2}\right\rangle\!\!\right\rangle_{\mathbf{x}(\tau)=\mathbf{r}_1+B_{\mathcal{T}}(\tau)}$$
$$+\frac{\hbar c\alpha_2}{4(2\pi)^{D/2}\varepsilon_0}\int_0^\infty\frac{d\mathcal{T}}{\mathcal{T}^{1+D/2}}\left\langle\!\!\left\langle\langle\varepsilon_r(\mathbf{x})\rangle_{\mathbf{x}(\tau)}^{-3/2}\right\rangle\!\!\right\rangle_{\mathbf{x}(\tau)=\mathbf{r}_2+B_{\mathcal{T}}(\tau)}. \tag{4.41}$$

These two terms represent the individual one-body contributions associated with each atom. No interatomic coupling appears at this order, reflecting the additive nature of the linear response approximation in the absence of overlapping worldlines.

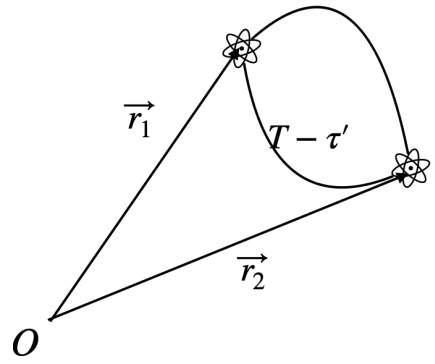

FIGURE 4.1. A sketch of two atoms interacting with each other in the worldline picture. The path of total running time $\mathcal{T}$ starts from one atom and is set to hit the second atom at an arbitrary intermediate time τ'.

To find the second functional derivative for the interaction:

$$\begin{aligned}
&\frac{\delta^2 E}{\delta\varepsilon_r(\mathbf{r}')\delta\varepsilon_r(\mathbf{r}'')} \\
&= -\frac{\hbar c}{2(2\pi)^{D/2}}\int_0^\infty \frac{d\mathcal{T}}{\mathcal{T}^{1+D/2}}\int d^{D-1}x_0 \left\langle\!\!\left\langle \frac{\delta^2}{\delta\varepsilon_r(\mathbf{r}')\delta\varepsilon_r(\mathbf{r}'')}\langle\varepsilon_r(\mathbf{x})\rangle_{\mathbf{x}(\tau)}^{-1/2}\right\rangle\!\!\right\rangle_{\mathbf{x}(\tau)} \\
&= -\frac{\hbar c}{2(2\pi)^{D/2}}\int_0^\infty \frac{d\mathcal{T}}{\mathcal{T}^{1+D/2}}\int d^{D-1}x_0 \left\langle\!\!\left\langle \left[\frac{1}{\mathcal{T}}\int_0^{\mathcal{T}} dt\delta^{D-1}(\mathbf{r}''-\mathbf{x}(t))\right]\right.\right. \\
&\left.\left.\times\left[\frac{1}{\mathcal{T}}\int_0^{\mathcal{T}} dt'\delta^{D-1}(\mathbf{r}'-\mathbf{x}(t'))\right]\frac{3}{4}\langle\varepsilon_r(\mathbf{x})\rangle_{\mathbf{x}(\tau)}^{-5/2}\right\rangle\!\!\right\rangle_{\mathbf{x}(\tau)} \\
&= \frac{-3\hbar c}{8(2\pi)^{D/2}}\int_0^\infty \frac{d\mathcal{T}}{\mathcal{T}^{2+D/2}}\int_0^{\mathcal{T}} d\tau' \left\langle\!\!\left\langle \langle\varepsilon_r(\mathbf{x})\rangle_{\mathbf{x}(\tau)}^{-5/2}\delta^{D-1}[\mathbf{r}''-\mathbf{x}(\tau')]\right\rangle\!\!\right\rangle_{\mathbf{x}(\tau)=\mathbf{r}'+B_{\mathcal{T}}(\tau)}.
\end{aligned} \tag{4.42}$$

The full 2nd-order result for the Casimir–Polder potential contains 3 terms of order α_1^2, α_2^2 and $\alpha_1\alpha_2$. The $\alpha_1\alpha_2$ term can be written as

$$V_{\text{CP}}(\mathbf{r}_1,\mathbf{r}_2) = \frac{-3\hbar c\alpha_1\alpha_2}{8(2\pi)^{D/2}\varepsilon_0^2}\int_0^\infty \frac{d\mathcal{T}}{\mathcal{T}^{2+D/2}}\int_0^{\mathcal{T}} d\tau' \left\langle\!\!\left\langle \langle\varepsilon_r(\mathbf{x})\rangle_{\mathbf{x}(\tau)}^{-5/2}\delta^{D-1}[\mathbf{r}_2-\mathbf{x}(\tau')]\right\rangle\!\!\right\rangle_{\mathbf{x}(\tau)}, \tag{4.43}$$

where $\mathbf{x}(\tau) = \mathbf{r}_1 + B_{\mathcal{T}}$. Using the identity

$$\left\langle\!\!\left\langle F[\mathbf{x}(\tau)]\delta^{D-1}[\mathbf{r}'-\mathbf{x}(\tau')]\right\rangle\!\!\right\rangle_{\mathbf{x}(\tau)} = P_{\mathbf{x}(\tau')}(\mathbf{r}')\left\langle\!\!\left\langle F[\mathbf{x}(\tau)]\right\rangle\!\!\right\rangle_{\mathbf{x}(\tau)|\mathbf{x}(\tau')=\mathbf{r}'}, \tag{4.44}$$

where P in our case is the probability density of a Brownian bridge to reach $\mathbf{r}_2-\mathbf{r}_1$ at time τ' in $D-1$ spatial dimensions and F is a test functional, the delta function is eliminated by introducing the crossing probability. A sketch of conditioned worldlines connecting two atoms is shown in Fig. 4.1.

Recall that $B_{\mathcal{T}}(t) = \sqrt{\mathcal{T}}B(t/\mathcal{T})$, and $\mathrm{Var}(B_{\mathcal{T}}(t)) = \mathcal{T} \times \mathrm{Var}(B(t/\mathcal{T})) = \mathcal{T}(\frac{t}{\mathcal{T}}(1 - \frac{t}{\mathcal{T}})) = t(1 - t/\mathcal{T})$, then the Gaussian form of $P[t; r, \mathcal{T}]$ can be determined as

$$P[t; r, \mathcal{T}] = \frac{\exp[-r^2/2t(1-t/\mathcal{T})]}{[2\pi t(1-t/\mathcal{T})]^{(D-1)/2}}, \tag{4.45}$$

with $r = |\mathbf{r}_2 - \mathbf{r}_1|$. Thus, the final form for two atoms TE potential is given by

$$V_{\mathrm{CP}}(\mathbf{r}_1, \mathbf{r}_2) = \frac{-3\hbar c\alpha_1\alpha_2}{8(2\pi)^{D/2}\varepsilon_0^2}\int_0^\infty \frac{d\mathcal{T}}{\mathcal{T}^{2+D/2}}\int_0^{\mathcal{T}} d\tau' \frac{\exp[-r^2/2\tau'(1-\tau'/\mathcal{T})]}{[2\pi\tau'(1-\tau'/\mathcal{T})]^{(D-1)/2}} \times \left\langle\!\!\left\langle \langle \varepsilon_r(\mathbf{x})\rangle_{\mathbf{x}(\tau)}^{-5/2} \right\rangle\!\!\right\rangle_{\mathbf{x}(\tau)=\mathbf{r}_1+B_{\tau',0\to r}(\tau)}. \tag{4.46}$$

To find the potential between the two atoms in vacuum, we take ε_r to be 1 through all space. By change of variables $y = \tau'/\mathcal{T}$ and rescaling of $\mathcal{T} \to r^2\mathcal{T}$ to factor out the r dependence, we have

$$\begin{aligned} V_{\mathrm{CP}}(\mathbf{r}_1, \mathbf{r}_2) &= \frac{-3\hbar c\alpha_1\alpha_2}{8(2\pi)^{D/2}\varepsilon_0^2}\int_0^\infty \frac{d\mathcal{T}}{\mathcal{T}^{2+D/2}}\int_0^{\mathcal{T}} d\tau' \frac{\exp[-r^2/2\tau'(1-\tau'/\mathcal{T})]}{[2\pi\tau'(1-\tau'/\mathcal{T})]^{(D-1)/2}} \\ &= \frac{-3\hbar c\alpha_1\alpha_2}{8(2\pi)^{D/2}\varepsilon_0^2}\int_0^\infty \frac{d\mathcal{T}}{\mathcal{T}^{2+D/2}}\int_0^1 \mathcal{T} dy \frac{\exp[-r^2/2\mathcal{T}y(1-y)]}{[2\pi\mathcal{T}y(1-y)]^{(D-1)/2}} \\ &= \frac{-3\hbar c\alpha_1\alpha_2}{8(2\pi)^{D/2}\varepsilon_0^2}\int_0^\infty \frac{r^2 d\mathcal{T}}{r^{4+D}\mathcal{T}^{2+D/2}}\int_0^1 r^2\mathcal{T} dy \frac{\exp[-1/2\mathcal{T}y(1-y)]}{r^{D-1}[2\pi\mathcal{T}y(1-y)]^{(D-1)/2}} \\ &= \frac{-3\hbar c\alpha_1\alpha_2}{8(2\pi)^{D/2}\varepsilon_0^2}\frac{1}{r^{2D-1}}\int_0^\infty \frac{d\mathcal{T}}{\mathcal{T}^{1+D/2}}\int_0^1 dy \frac{\exp[-1/2\mathcal{T}y(1-y)]}{[2\pi\mathcal{T}y(1-y)]^{(D-1)/2}}. \end{aligned} \tag{4.47}$$

The double integral can be evaluated as

$$\int_0^\infty \frac{d\mathcal{T}}{\mathcal{T}^{1+D/2}}\int_0^1 dy \frac{\exp[-1/2\mathcal{T}y(1-y)]}{[2\pi\mathcal{T}y(1-y)]^{(D-1)/2}} = \frac{2^{D/2}\pi^{\frac{1}{2}-\frac{D}{2}}\Gamma\left(\frac{D}{2}+1\right)^2\Gamma\left(D-\frac{1}{2}\right)}{\Gamma(D+2)}. \tag{4.48}$$

In 3+1-dimensional spacetime, take $D = 4$, the expression reduces to $\frac{1}{4\pi}$. So according to the worldline method, the TE potential between two ground-state

neutral atoms is

$$V_{\text{TE}}(r) = \frac{-3\hbar c\alpha_1\alpha_2}{128\pi^3\varepsilon_0^2}\frac{1}{r^7}. \tag{4.49}$$

Comparing to the full potential Eq. (4.29), this TE-component calculation only accounts for about 6.5% of the actual interaction.

The above procedures can be generalized to find the TE potential for an arbitrary number of atoms expanded to arbitrary order of variation. To start with this derivation, suppose N represents the number of atoms and k represents the order of variation. Introducing N atoms corresponds to a vector of N perturbations in the dielectric background, given by $\mathbf{h}(\mathbf{r})$:

$$\mathbf{h}(\mathbf{r}) = \begin{pmatrix} \delta\varepsilon_1 \\ \delta\varepsilon_2 \\ \delta\varepsilon_3 \\ \cdots \\ \delta\varepsilon_N \end{pmatrix} = \begin{pmatrix} \frac{\alpha_1}{\varepsilon_0}\delta(\mathbf{r}-\mathbf{r}_1) \\ \frac{\alpha_2}{\varepsilon_0}\delta(\mathbf{r}-\mathbf{r}_2) \\ \frac{\alpha_3}{\varepsilon_0}\delta(\mathbf{r}-\mathbf{r}_3) \\ \cdots \\ \frac{\alpha_N}{\varepsilon_0}\delta(\mathbf{r}-\mathbf{r}_N) \end{pmatrix}. \tag{4.50}$$

Carrying out the functional derivatives up to k-th order ($k \leq N$) explicitly, we obtain the general expression

$$\begin{aligned} V_{\text{CP}}^{\text{TE}(k)}(\mathbf{r}_1,\ldots,\mathbf{r}_N) = (-1)^{k+1}\frac{(2k-1)!!\hbar c}{2^{k+1}k!(2\pi)^{D/2}\varepsilon_0^k}\sum_{k_1,\ldots,k_k=1}^{N}\alpha_{k_1}\ldots\alpha_{k_k}\int_0^\infty\frac{d\mathcal{T}}{\mathcal{T}^{k+D/2}} \\ \times\int_0^{\mathcal{T}}\prod_{i=2}^{k}d\tau_i\, f_{\mathbf{x}(\tau_2)}(\mathbf{r}_2)f_{\mathbf{x}(\tau_3)}(\mathbf{r}_3)\ldots f_{\mathbf{x}(\tau_k)}(\mathbf{r}_k) \\ \times\left\langle\!\!\left\langle \langle\varepsilon_r\rangle_{\mathbf{x}(\tau)}^{-k-1/2} \right\rangle\!\!\right\rangle_{\mathbf{x}(\tau)|\mathbf{x}(0)=\mathbf{r}_{k_1},\mathbf{x}(\tau_j)=\mathbf{r}_{k_j},\mathbf{x}(\mathcal{T})=\mathbf{x}(0)}. \end{aligned} \tag{4.51}$$

The expectation $\langle\varepsilon_r\rangle_{\mathbf{x}(\tau)}$ is evaluated along the fluctuating path conditioned to intersect the specified atomic sites at times $\tau_2 < \tau_3 < \cdots < \tau_k$, with starting and

ending position at $\mathbf{r}_{k_1}$. The Gaussian bridge densities $f_{\mathbf{x}(\tau_j)}(\mathbf{r}_{k_j})$ encode the likelihood of the path intersecting the atomic position $\mathbf{r}_{k_j}$ at time τ_j, conditioned on all prior locations.

The first bridge density describes the probability of a Brownian loop beginning and ending at $\mathbf{r} = \mathbf{r}_{k_1}$ intersecting the second atom at $\mathbf{r}_2$ at time τ_2:

$$f_{\mathbf{x}(\tau_2)}(\mathbf{r}_2) = \frac{1}{[2\pi\tau_2(1-\tau_2/\mathcal{T})]^{d/2}} e^{-(\mathbf{r}_2-\mathbf{r})^2/2\tau_2(1-\tau_2/\mathcal{T})}. \tag{4.52}$$

Subsequent bridge probabilities depend on prior intermediate points, since the stochastic process evolves forward in time. Two distinct cases naturally arise depending on whether $\tau_3 < \tau_2$ or $\tau_3 > \tau_2$, as the causal sequence of interactions determines how field correlations propagate through the trajectory. This temporal ordering plays a critical role in constructing consistent conditional probability densities for the Brownian bridge.

In the case $\tau_3 < \tau_2$, the Brownian path first reaches the point $\mathbf{r}_3$ at time τ_3, then proceeds to $\mathbf{r}_2$ at a later time τ_2, before ultimately returning to its endpoint $\mathbf{r}$ at total time $\mathcal{T}$. The conditional density of observing $\mathbf{x}(\tau_3) = \mathbf{r}_3$ given that $\mathbf{x}(\tau_2) = \mathbf{r}_2$ is expressed as

$$f_{\mathbf{x}(\tau_3)}(\mathbf{r}_3 \mid \mathbf{x}(\tau_2) = \mathbf{r}_2) = \frac{1}{[2\pi\tau_3(1-\tau_3/\tau_2)]^{d/2}} e^{-[\mathbf{r}_3-\mathbf{r}_2(1-\tau_3/\tau_2)-\mathbf{r}\tau_3/\tau_2]^2/2\tau_3(1-\tau_3/\tau_2)}. \tag{4.53}$$

Conversely, if $\tau_3 > \tau_2$, then the path first encounters $\mathbf{r}_2$ and subsequently $\mathbf{r}_3$ at time τ_3, before terminating at $\mathbf{r}$ at time $\mathcal{T}$. The corresponding conditional density

is given by

$$f_{\mathbf{x}(\tau_3)}(\mathbf{r}_3 \mid \mathbf{x}(\tau_2) = \mathbf{r}_2) = \frac{1}{[2\pi\tau_{3-}(1-\tau_{3-}/\mathcal{T}_2)]^{d/2}} \times e^{-[\mathbf{r}_3 - \mathbf{r}_2(1-\tau_{3-}/\mathcal{T}_2) - \mathbf{r}\tau_{3-}/\mathcal{T}_2]^2/2\tau_{3-}(1-\tau_{3-}/\mathcal{T}_2)}, \tag{4.54}$$

where the shifted variables $\tau_{3-} := \tau_3 - \tau_2$ and $\mathcal{T}_2 := \mathcal{T} - \tau_2$ denote the elapsed time since the last conditioned point and the remaining time to the endpoint, respectively. These substitutions serve to locally re-anchor the Brownian segment relative to the most recent reference point, allowing each step to be described in its natural causal frame.

For a given temporal ordering, the total joint bridge probability is constructed by multiplying the successive conditional densities. For instance, in the case $\tau_3 > \tau_2$, the product of the two bridge densities for reaching $\mathbf{r}_2$ and then $\mathbf{r}_3$ is

$$\begin{aligned} f_{\mathbf{x}(\tau_2)}(\mathbf{r}_2) f_{\mathbf{x}(\tau_3)}(\mathbf{r}_3 \mid \mathbf{x}(\tau_2) = \mathbf{r}_2) &= \frac{e^{-(\mathbf{r}_2-\mathbf{r})^2/2\tau_2(1-\tau_2/\mathcal{T})}}{[2\pi\tau_2(1-\tau_2/\mathcal{T})]^{d/2}} \\ &\times \frac{e^{-[\mathbf{r}_3-\mathbf{r}_2(1-\tau_{3-}/\mathcal{T}_2)-\mathbf{r}\tau_{3-}/\mathcal{T}_2]^2/2\tau_{3-}(1-\tau_{3-}/\mathcal{T}_2)}}{[2\pi\tau_{3-}(1-\tau_{3-}/\mathcal{T}_2)]^{d/2}} \\ &= \frac{e^{-(\mathbf{r}_3-\mathbf{r})^2/2\tau_3(1-\tau_3/\mathcal{T})}}{[2\pi\tau_3(1-\tau_3/\mathcal{T})]^{d/2}} \frac{e^{-[\mathbf{r}_2-\mathbf{r}(1-\tau_2/\tau_3)-\mathbf{r}_3\tau_2/\tau_3]^2/2\tau_2(1-\tau_2/\tau_3)}}{[2\pi\tau_2(1-\tau_2/\tau_3)]^{d/2}} \\ &= f_{\mathbf{x}(\tau_3)}(\mathbf{r}_3) f_{\mathbf{x}(\tau_2)}(\mathbf{r}_2 \mid \mathbf{x}(\tau_3) = \mathbf{r}_3). \end{aligned} \tag{4.55}$$

This final equality reveals a profound symmetry: the joint probability density is invariant under permutation of the time labels, provided the positions are appropriately conditioned. This mutual consistency stems from the basic identity of joint probabilities in conditional form, namely

$$P(A \cap B) = P(A)P(B \mid A) = P(B)P(A \mid B). \tag{4.56}$$

This statistical symmetry is essential for maintaining the consistency and reparameterization invariance of the worldline path integral. The equivalence of the normalization prefactors in Eq. (4.55) can be verified algebraically:

$$\begin{aligned}\tau_2(1-\tau_2/\mathcal{T})\tau_{3-}(1-\tau_{3-}/\mathcal{T}_2) &= \tau_2(\mathcal{T}-\tau_2)\tau_{3-}(\mathcal{T}_2-\tau_{3-})/\mathcal{T}\mathcal{T}_2 \\ &= \tau_2(\tau_3-\tau_2)(\mathcal{T}-\tau_3)/\mathcal{T} \\ &= \tau_3(1-\tau_3/\mathcal{T})\tau_2(1-\tau_2/\tau_3), \end{aligned} \tag{4.57}$$

confirming that the two probability factorizations are mathematically equivalent. This guarantees that no spurious asymmetry is introduced by choosing one time ordering over another and validates the robustness of multi-point conditioning in the Brownian bridge construction.

To systematically generate the full contribution of the N-body TE potential, we perform nested integrations over all intermediate times in a fixed time ordering:

$$\begin{aligned} V_{\rm CP}^{\rm TE(}{}^{(k)}(\mathbf{r}_1,\ldots,\mathbf{r}_N) &= (-1)^{k+1}\frac{(2k-1)!!\,\hbar c}{2^{k+1}k(2\pi)^{D/2}\varepsilon_0^k}\sum_{k_1,\ldots,k_k=1}^{N}\alpha_{k_1}\cdots\alpha_{k_k}\int_0^\infty\frac{d\mathcal{T}}{\mathcal{T}^{k+D/2}} \\ &\times\int_{0\le\tau_2\le\cdots\le\tau_k\le\mathcal{T}}\prod_{i=2}^{k}d\tau_i\, f_{\mathbf{x}(\tau_2)}(\mathbf{r}_2)\, f_{\mathbf{x}(\tau_3)}(\mathbf{r}_3|\mathbf{x}(\tau_2)=\mathbf{r}_2)\cdots f_{\mathbf{x}(\tau_k)}(\mathbf{r}_k|\mathbf{x}(\tau_{k-1})=\mathbf{r}_{k-1}) \\ &\times\left\langle\!\!\left\langle \langle\varepsilon_r\rangle_{\mathbf{x}(\tau)}^{-k-1/2}\right\rangle\!\!\right\rangle_{\mathbf{x}(\tau)|\mathbf{x}(0)=\mathbf{r}_{k_1},\mathbf{x}(\tau_j)=\mathbf{r}_{k_j},\mathbf{x}(\mathcal{T})=\mathbf{x}(0)}. \end{aligned} \tag{4.58}$$

The additional factor of $1/k$ compared to Eq. (4.51) accounts for the number of permutations of intermediate time orderings $(k-1)!$, which are folded into the fixed-time-ordered form by integrating over $0\le\tau_2\le\cdots\le\tau_k\le\mathcal{T}$. This formulation offers a recursive, fully probabilistic representation of higher-order many-body Casimir–Polder interactions in the TE mode, and lays the foundation for developing efficient

worldline Monte Carlo methods incorporating bridge sampling and time-ordering constraints.

4.3.2 TM Mode

The TM Casimir–Polder interaction shares a structural similarity with the TE case under a formal duality: exchanging the roles of permittivity and permeability, $\varepsilon_r \leftrightarrow \mu_\mathrm{r}$, and replacing the atomic coupling α_0/ε_0 with its magnetic analog $\beta_0\mu_0$. While this symmetry provides conceptual guidance, the actual path-integral calculation is more involved in the TM sector. In particular, the TM potential defined in Eq. (2.59) contains gradient and Laplacian terms of $\log\varepsilon_r$, which makes the evaluation of worldline integrals more subtle. When we include a polarizable atom as a point-like perturbation and expand the total potential to first order in α_0, the resulting expression becomes

$$V_{\mathrm{TM}}(\mathbf{x}) \to \frac{1}{8}(\nabla\log\varepsilon_r)^2 - \frac{1}{4}\nabla^2\log\varepsilon_r - \frac{\alpha_0}{4\varepsilon_0}\big[(\nabla\log\varepsilon_r)\cdot\nabla - \nabla^2\big]\frac{1}{\varepsilon_r}\delta^{D-1}(\mathbf{x}-\mathbf{r}). \tag{4.59}$$

In a region where ε_r is uniform, the gradient terms vanish, and only the atomic term contributes. This leads to a worldline expression for the TM Casimir–Polder potential analogous to the TE case:

$$V_{\mathrm{CP}}^{\mathrm{TM}}(\mathbf{r}) = \frac{\hbar c\alpha_0}{4(2\pi)^{D/2}\varepsilon_0}\int_0^\infty \frac{d\mathcal{T}}{\mathcal{T}^{1+D/2}}\left\langle\!\!\left\langle\left(\frac{1}{\langle\varepsilon_r\rangle_{\mathbf{x}_\mathbf{r}(\tau)}} - \frac{\mathcal{T}}{2\varepsilon_r}\nabla^2\right)\langle\varepsilon_r\rangle_{\mathbf{x}_\mathbf{r}(\tau)}^{-1/2} e^{-\mathcal{T}\langle V_{\mathrm{TM}}\rangle_{\mathbf{x}_\mathbf{r}(\tau)}}\right\rangle\!\!\right\rangle_{\mathbf{x}_\mathbf{r}}. \tag{4.60}$$

This formula sets the stage for Monte Carlo evaluations of TM Casimir forces, as discussed in Ref. [69].

The two-body case ($N = 2$) proceeds similarly. Assuming a vacuum background with $\varepsilon_r = 1$, the second-order shift yields the TM cross-energy between two atoms:

$$V_{\rm CP}^{\rm TM}(\mathbf{r}_1,\mathbf{r}_2) = -\frac{\hbar c\alpha_1\alpha_2}{8(2\pi)^{D-1/2}\varepsilon_0^2}\int_0^\infty \frac{d\mathcal{T}}{\mathcal{T}^{2+D/2}}\int_0^{\mathcal{T}} d\tau' \left(3 - \frac{\mathcal{T}}{2}\left(\nabla_1^2+\nabla_2^2\right) + \frac{\mathcal{T}^2}{4}\nabla_1^2\nabla_2^2\right) \times \frac{1}{[\tau'(1-\tau'/\mathcal{T})]^{d/2}} e^{-(\mathbf{r}_1-\mathbf{r}_2)^2/2\mathcal{T}\tau'(1-\tau'/\mathcal{T})}. \tag{4.61}$$

Here, the Laplacians act only on the individual atom coordinates. For $D = 4$, the result becomes

$$V_{\rm CP}^{\rm TM}(r) = -\frac{43\hbar c\alpha_1\alpha_2}{8\pi(4\pi\varepsilon_0)^2}\frac{1}{r^7}. \tag{4.62}$$

This accounts for roughly 93.5% of the total Casimir–Polder energy, much more than the TE contribution. Note that this differs from the Green-tensor result, which gives a pure TM coefficient of $-73/16$ in Eq. (4.29), but the sum of the TE and TM worldline results still reproduces the exact full answer — confirming that the scalar decomposition is complete here.

Just like in the TE case, we can extend this to N-body TM interactions between N polarizable particles. The full expression for the kth-order term ($k \le N$) is

$$V_{\rm CP}^{{\rm TM}(k)}(\mathbf{r}_1,\ldots,\mathbf{r}_N) = (-1)^{k+1}\frac{\hbar c}{2^{k+1}k!(2\pi)^{D/2}\varepsilon_0^k}\sum_{k_1,\ldots,k_k=1}^{N}\alpha_{k_1}\cdots\alpha_{k_k}\int_0^\infty\frac{d\mathcal{T}}{\mathcal{T}^{k+D/2}} \int_0^{\mathcal{T}} d\tau_2\cdots d\tau_k f_{\mathbf{x}(\tau_2)}(\mathbf{r}_2)f_{\mathbf{x}(\tau_3)}(\mathbf{r}_3)\cdots f_{\mathbf{x}(\tau_k)}(\mathbf{r}_k) \times\left\langle\!\!\left\langle \prod_{j=1}^{k}\left[\frac{2j-1}{\langle\varepsilon_r\rangle_{\mathbf{x}(\tau)}} - \frac{\mathcal{T}}{2\varepsilon_r(\mathbf{r}_{k_j})}\nabla_{k_j}^2\right]\frac{e^{-\mathcal{T}\langle V_{\rm TM}\rangle}}{\langle\varepsilon_r\rangle_{\mathbf{x}(\tau)}^{1/2}}\right\rangle\!\!\right\rangle_{\mathbf{x}(\tau)|\mathbf{x}(0)=\mathbf{r}_{k_1},\mathbf{x}(\tau_j)=\mathbf{r}_{k_j},\mathbf{x}(\mathcal{T})=\mathbf{x}(0)}. \tag{4.63}$$

This expression is the multi-atom generalization of Eq. (4.61) in analogy to the TE result (4.51).

After explicitly time-ordering the intermediate events, we arrive at a more structured expression:

$$V_{\rm CP}^{{\rm TM}(k)}(\mathbf{r}_1,\ldots,\mathbf{r}_N) = (-1)^{k+1}\frac{\hbar c}{2^{k+1}k(2\pi)^{D/2}\varepsilon_0^k}\sum_{k_1,\ldots,k_k=1}^{N}\alpha_{k_1}\cdots\alpha_{k_k}\int_0^\infty\frac{d\mathcal{T}}{\mathcal{T}^{k+D/2}}$$
$$\times\int_{0\le\tau_2\le\cdots\le\tau_k\le\mathcal{T}}\prod_{i=2}^{k}d\tau_i\, f_{\mathbf{x}(\tau_2)}(\mathbf{r}_2)f_{\mathbf{x}(\tau_3)}(\mathbf{r}_3\mid\mathbf{x}(\tau_2)=\mathbf{r}_2)\cdots f_{\mathbf{x}(\tau_k)}(\mathbf{r}_k\mid\mathbf{x}(\tau_{k-1})=\mathbf{r}_{k-1})$$
$$\times\left\langle\!\!\left\langle\prod_{j=1}^{k}\left[\frac{2j-1}{\langle\varepsilon_r\rangle_{\mathbf{x}(\tau)}}-\frac{\mathcal{T}}{2\varepsilon_r(\mathbf{r}_{k_j})}\nabla_{k_j}^2\right]\frac{e^{-\mathcal{T}\langle V_{\rm TM}\rangle}}{\langle\varepsilon_r\rangle_{\mathbf{x}(\tau)}^{1/2}}\right\rangle\!\!\right\rangle_{\mathbf{x}(\tau)|\mathbf{x}(0)=\mathbf{r}_{k_1},\mathbf{x}(\tau_j)=\mathbf{r}_{k_j},\mathbf{x}(\mathcal{T})=\mathbf{x}(0)}. \tag{4.64}$$

Here, the bridge densities ensure proper probabilistic structure between insertions. The differential operators $\nabla_{k_j}^2$ act on distinct, spatially localized atomic positions and therefore commute with one another. As a result, the product of these Laplacians remains invariant under permutation, allowing the operator ordering within the integrand to be arbitrary. This commutativity simplifies both the formal structure and the numerical evaluation of higher-order multi-body Casimir–Polder terms in the TM sector.

4.4 The Breakdown of Scalar Approximation at $N = 3$

To critically evaluate the scalar decomposition's validity in multi-body Casimir–Polder interactions, we now apply the general formalism to the case of three atoms. When $N = 3$, one additional crossing time τ_3 is needed to enforce that the worldline intersects all three atomic positions. Beginning with the TE polarization sector, the

contribution from three-body cross-interactions is

$$
\begin{aligned}
V_{\mathrm{CP}}^{\mathrm{TE}(3)}(\mathbf{r}_1,\mathbf{r}_2,\mathbf{r}_3) &= \frac{15\hbar c\alpha_1\alpha_2\alpha_3}{48(2\pi)^{D/2}\varepsilon_0^3}\int_0^\infty \frac{d\mathcal{T}}{\mathcal{T}^{3+D/2}}\int_{0\le\tau_2\le\tau_3\le\mathcal{T}} d\tau_2\, d\tau_3 \\
&\quad\times f_{\mathbf{x}(\tau_2)}(\mathbf{r}_2) f_{\mathbf{x}(\tau_3)}(\mathbf{r}_3|\mathbf{x}(\tau_2)=\mathbf{r}_2) \\
&= \frac{15\hbar c\alpha_1\alpha_2\alpha_3}{48(2\pi)^{D/2}\varepsilon_0^3}\int_0^\infty \frac{d\mathcal{T}}{\mathcal{T}^{3+D/2}}\int_0^{\mathcal{T}} d\tau_2\int_{\tau_2}^{\mathcal{T}} d\tau_3\, \frac{e^{-(\mathbf{r}_3-\mathbf{r}_1)^2/2\tau_3(1-\tau_3/\mathcal{T})}}{[2\pi\tau_3(1-\tau_3/\mathcal{T})]^{d/2}} \\
&\qquad\times \frac{e^{-[\mathbf{r}_2-\mathbf{r}_1(1-\tau_2/\tau_3)-\mathbf{r}_3\tau_2/\tau_3]^2/2\tau_2(1-\tau_2/\tau_3)}}{[2\pi\tau_2(1-\tau_2/\tau_3)]^{d/2}}. \qquad (4.65)
\end{aligned}
$$

The time-ordering $\tau_2 < \tau_3$ enforces that the worldline, beginning at $\mathbf{r}_1$ and running for duration $\mathcal{T}$, hits the second atom at time τ_2 and subsequently the third atom at τ_3. All paths satisfying this ordering are integrated over. The interaction strength is thus accumulated over the ensemble of such constrained Brownian bridges.

The TM polarization sector is more complicated due to the appearance of Laplacian operators, resulting from the longitudinal structure of the Green tensor. The TM three-body contribution takes the form

$$
\begin{aligned}
V_{\mathrm{CP}}^{\mathrm{TM}(3)}(\mathbf{r}_1,\mathbf{r}_2,\mathbf{r}_3) &= \frac{\hbar c\alpha_1\alpha_2\alpha_3}{48(2\pi)^{D/2}\varepsilon_0^3}\int_0^\infty \frac{d\mathcal{T}}{\mathcal{T}^{3+D/2}}\int_0^{\mathcal{T}} d\tau_2\int_{\tau_2}^{\mathcal{T}} d\tau_3 \\
&\quad\times\left[15-\frac{3\mathcal{T}}{2}\nabla_1^2-\frac{3\mathcal{T}}{2}\nabla_2^2-\frac{3\mathcal{T}}{2}\nabla_3^2+\frac{\mathcal{T}^2}{4}\nabla_1^2\nabla_2^2\right. \\
&\quad\left.+\frac{\mathcal{T}^2}{4}\nabla_1^2\nabla_3^2+\frac{\mathcal{T}^2}{4}\nabla_2^2\nabla_3^2-\frac{\mathcal{T}^3}{8}\nabla_1^2\nabla_2^2\nabla_3^2\right]\frac{e^{-(\mathbf{r}_3-\mathbf{r}_1)^2/2\tau_3(1-\tau_3/\mathcal{T})}}{[2\pi\tau_3(1-\tau_3/\mathcal{T})]^{d/2}} \\
&\quad\times \frac{e^{-[\mathbf{r}_2-\mathbf{r}_1(1-\tau_2/\tau_3)-\mathbf{r}_3\tau_2/\tau_3]^2/2\tau_2(1-\tau_2/\tau_3)}}{[2\pi\tau_2(1-\tau_2/\tau_3)]^{d/2}}. \qquad (4.66)
\end{aligned}
$$

At this stage, the positions $\mathbf{r}_i$ remain arbitrary. To explore geometry dependence, we analyze two configurations: (i) three atoms arranged linearly with spacing $R/2$, and (ii) an equilateral triangle with side length R.

Collinear Configuration: The scalar worldline method gives

$$\Delta E_{\text{scalar}}^{\text{linear}} \approx +358 \frac{\hbar c \alpha_1 \alpha_2 \alpha_3}{\pi} \frac{1}{(4\pi\varepsilon_0)^3 R^{10}}, \tag{4.67}$$

whereas the exact Green-tensor method gives

$$\Delta E_{\text{tensor}}^{\text{linear}} = -186 \frac{\hbar c \alpha_1 \alpha_2 \alpha_3}{\pi} \frac{1}{(4\pi\varepsilon_0)^3 R^{10}}. \tag{4.68}$$

This substantial discrepancy in both magnitude and sign indicates strong polarization coupling that the scalar approximation in worldline methods fails to capture.

Equilateral Triangle Configuration: The scalar method yields

$$\Delta E_{\text{scalar}}^{\triangle} \approx -1.97 \frac{\hbar c \alpha_1 \alpha_2 \alpha_3}{\pi} \frac{1}{(4\pi\varepsilon_0)^3 R^{10}}, \tag{4.69}$$

while the Green-tensor approach gives

$$\Delta E_{\text{tensor}}^{\triangle} = +5.2 \frac{\hbar c \alpha_1 \alpha_2 \alpha_3}{\pi} \frac{1}{(4\pi\varepsilon_0)^3 R^{10}}. \tag{4.70}$$

Again, the discrepancy emphasizes the limitations of scalar decomposition in geometries where electromagnetic polarization modes strongly interact.

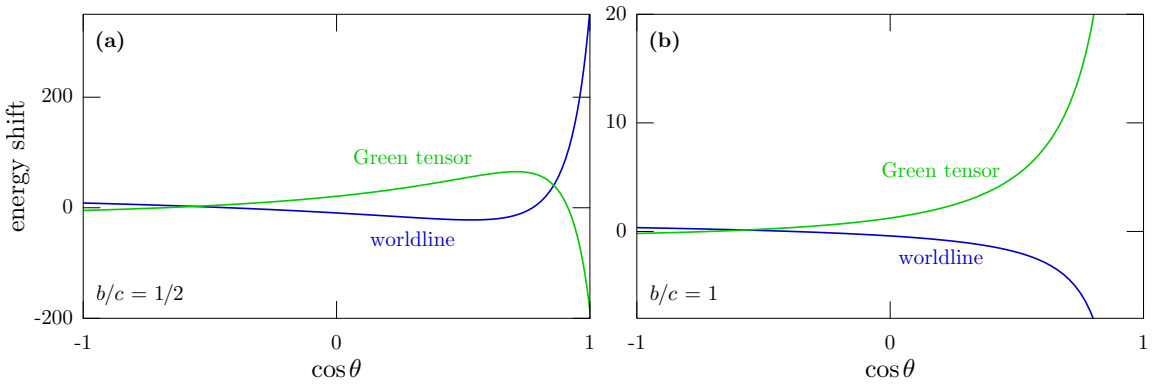

FIGURE 4.2. The Casimir–Polder coefficients for the three-body interaction obtained from the worldline scalar sum and the Green tensor method, as a function of the cosine of the angle between the displacement vectors. The comparison for $b/c = 0.5$ is shown in (a), where the collinear configuration corresponds to $\cos\theta = 1$. The case $b/c = 1$ is shown in (b), where the equilateral-triangle configuration corresponds to $\cos\theta = 0.5$. In both cases, the energy shift is plotted in units of $\hbar c \alpha_1 \alpha_2 \alpha_3/(4\pi\varepsilon_0)^3 \pi R^{10}$.

Geometric Interpolation: To systematically study the extent of this breakdown of the scalar approximation, we define the atomic positions as

$$\begin{aligned} \mathbf{r}_A &= (0,0,0), \\ \mathbf{r}_B &= (b,0,0), \\ \mathbf{r}_C &= (c\cos\theta, c\sin\theta, 0), \end{aligned} \tag{4.71}$$

with the angular parameter θ controlling the triangular geometry. For example, $\cos\theta = 1$ and $b/c = 0.5$ corresponds to a linear chain; $\cos\theta = 0.5$ and $b/c = 1$ gives an equilateral triangle. A scan over a continuous range of θ reveals directly the distinct predictions from the two methods in three-body configurations.

As seen in Fig. 4.2, the scalar worldline and tensor methods yield qualitatively and quantitatively different results across geometries, highlighting that the scalar approximation — while accurate in the two-body case — is unreliable in three-body

configurations due to unaccounted TE/TM mixing in polarization. This motivates extending the worldline formalism to incorporate full electromagnetic vector degrees of freedom.

4.5 Physical Interpretation and Future Direction

The discrepancy between the Green-tensor and worldline formalism becomes especially pronounced in the case of three-body Casimir–Polder interactions. While both approaches nominally employ a decomposition into transverse-electric (TE) and transverse-magnetic (TM) polarizations, they do so at fundamentally different levels of the theory, leading to nonequivalent results when multiple bodies are involved.

To see this, recall that in the Green tensor formalism, the interaction energy is expressed in terms of products of dyadic Green functions — each representing the response of the electromagnetic field to a point source. In the three-body interaction potential [Eq. (4.30)], the relevant terms involve products like $\mathbf{G}_{12} \cdot \mathbf{G}_{23} \cdot \mathbf{G}_{31}$, with each Green tensor $\mathbf{G}_{ij}$ associated with a distinct spatial domain of integration. The TE and TM components are preserved within each tensor, but the contractions between them naturally give rise to cross-polarization coupling terms. Thus, even if one starts with a TE or TM Green tensor, the resulting three-body energy contains contributions from both pure and mixed polarization channels. This interplay is intrinsic to the full electromagnetic description.

In contrast, the scalar worldline method introduces the TE/TM decomposition at the level of the scalar wave equations, which are derived from simplifying the full vector Maxwell equations under symmetry assumptions. The scalar fields corresponding to TE and TM modes are treated as independent fields, and their Casimir energies are evaluated using path integrals over closed random walks or

worldlines. However, this scalarization process neglects polarization mixing. Each scalar sector contributes independently, without any mechanism to reproduce cross-polarization terms.

This difference in how TE and TM modes are handled is relatively benign in the two-body case. Although the individual TE and TM contributions computed from the scalar worldline approach differ from those obtained via the Green-tensor method, the total energy — the sum of TE and TM components — matches exactly for planar or high-symmetry configurations. This accidental agreement stems from the symmetry and factorization properties of two-body interactions, where polarization mixing either vanishes or averages out.

However, this fortuitous matching no longer holds in the three-body case. When the geometry allows for genuine multi-path interactions, such as cyclic propagation between three distinct atoms, the lack of polarization mixing in the scalar worldline method leads to quantitative and qualitative discrepancies. For example, the three-body Casimir–Polder energy computed from the full Green tensor formalism includes significant contributions from mixed TE/TM terms. These are entirely absent in the scalar worldline calculation, which accounts only for additive contributions from TE-like and TM-like scalar paths. As a result, the total interaction potential from the scalar worldline method deviates from the exact value — both in magnitude and, in some cases, in sign — across a wide range of geometrical configurations.

This mismatch provides strong evidence that polarization coupling plays an essential role in many-body Casimir physics. The scalar worldline approximation, while powerful and geometrically flexible, fails to capture these inherently vectorial effects. Consequently, this observation motivates the development of extended worldline methods that go beyond the scalar paradigm — possibly incorporating

vector field degrees of freedom, polarization-resolved path ensembles, or hybrid tensor-scalar formulations. Such extensions would be necessary to achieve quantitative agreement with full electromagnetic Casimir energies in general geometries and multi-body settings.

Appendix to Chapter IV

A.1 Derivation of $N = 3$ Co-linear Casimir–Polder Potential with Green-Tensor Decomposition

We consider three neutral atoms located along the z-axis at positions z_1, z_2, and z_3 such that the distances are symmetric: $|z_3 - z_2| = |z_2 - z_1| = R/2$. This setup represents a natural generalization of the two-body Casimir–Polder interaction to the three-body case. The irreducible three-body potential, arising from closed-loop interactions mediated by the electromagnetic field, is given in terms of Green tensors as in Eq. (4.30).

To evaluate the contribution from the first term in the trace structure, we express it as an integral over frequency and transverse wavevectors:

$$\begin{aligned} V_{\mathrm{CP}}^{(3)} = -\frac{\hbar\alpha_1\alpha_2\alpha_3}{2\pi(8\pi^2\varepsilon_0)^3}\int_0^\infty ds \int_{-\infty}^\infty dk_x dk_y dk_x' dk_y' dk_x'' dk_y'' \frac{-s^6/c^6}{\kappa(s,k_x,k_y)\kappa(s,k_x',k_y')\kappa(s,k_x'',k_y'')} \\ \times \delta_{ab}\delta_{cd}\delta_{ef}(e_b e_c + h_b h_c)(e_d' e_e' + h_d' h_e')(e_f'' e_a'' + h_f'' h_a'') \\ \times e^{-\kappa(s,k_x,k_y)z} e^{-\kappa(s,k_x',k_y')z'} e^{-\kappa(s,k_x'',k_y'')z''}. \end{aligned} \tag{4.72}$$

The tensor structure contracts three Green tensors through dyadic polarizations. Expanding this product yields eight distinct terms, corresponding to all combinations

of electric and magnetic polarizations:

$$\begin{aligned}
&\delta_{ab}\delta_{cd}\delta_{ef}(\hat{e}_b\hat{e}_c + \hat{h}_b\hat{h}_c)(\hat{e}'_d\hat{e}'_e + \hat{h}'_d\hat{h}'_e)(\hat{e}''_f\hat{e}''_a + \hat{h}''_f\hat{h}''_a) \\
&= (\hat{e}_a\hat{e}_d + \hat{h}_a\hat{h}_d)(\hat{e}'_d\hat{e}'_f + \hat{h}'_d\hat{h}'_f)(\hat{e}''_f\hat{e}''_a + \hat{h}''_f\hat{h}''_a) \\
&= \mathrm{Tr}(\mathbf{A}_e\mathbf{A}'_e\mathbf{A}''_e) + \mathrm{Tr}(\mathbf{A}'_e\mathbf{A}''_e\mathbf{A}_h) + \mathrm{Tr}(\mathbf{A}_e\mathbf{A}''_e\mathbf{A}'_h) + \mathrm{Tr}(\mathbf{A}''_e\mathbf{A}_h\mathbf{A}'_h) \\
&\quad + \mathrm{Tr}(\mathbf{A}_e\mathbf{A}'_e\mathbf{A}''_h) + \mathrm{Tr}(\mathbf{A}'_e\mathbf{A}_h\mathbf{A}''_h) + \mathrm{Tr}(\mathbf{A}_e\mathbf{A}'_h\mathbf{A}''_h) + \mathrm{Tr}(\mathbf{A}_h\mathbf{A}'_h\mathbf{A}''_h). \qquad (4.73)
\end{aligned}$$

The first and last terms correspond to purely TE and TM polarizations, respectively, while the remaining six represent mixed polarization traces. We now evaluate these components one by one.

Transverse Electric (TE) Contribution

The TE trace evaluates to:

$$\mathrm{Tr}(\mathbf{A}_e\mathbf{A}'_e\mathbf{A}''_e) = \frac{(k_xk'_x + k_yk'_y)(k_xk''_x + k_yk''_y)(k'_xk''_x + k'_yk''_y)}{k_\rho^2 k_\rho'^2 k_\rho''^2}, \qquad (4.74)$$

and results in the energy:

$$\begin{aligned}
V^{(3)}_{\mathrm{TE}}(R) &= \frac{\hbar\alpha_1\alpha_2\alpha_3}{2\pi}\left(\frac{1}{8\pi^2\varepsilon_0}\right)^3 (2\pi^3)\int_0^\infty ds \int_0^\infty dk_\rho dk'_\rho dk''_\rho \\
&\quad \times \frac{s^6 k_\rho k'_\rho k''_\rho}{c^6\kappa\kappa'\kappa''}\, e^{-\kappa z}e^{-\kappa' z'}e^{-\kappa'' z''}\Big|_{z=z'=R/2,z''=R} \\
&= \frac{45\hbar c\alpha_1\alpha_2\alpha_3}{16\pi}\frac{1}{(4\pi\varepsilon_0)^3 R^{10}}. \qquad (4.75)
\end{aligned}$$

Transverse Magnetic (TM) Contribution

The TM contribution is more intricate due to the longitudinal components:

$$V_{\text{TM}}^{(3)}(R) = -\frac{\hbar\alpha_1\alpha_2\alpha_3}{2\pi}\left(\frac{1}{8\pi^2\varepsilon_0}\right)^3 \int_0^\infty ds \int_0^\infty dk_\rho dk'_\rho dk''_\rho \\ \times \frac{k_\rho k'_\rho k''_\rho \left[(2\pi)^3 k_\rho^2 k_\rho'^2 k_\rho''^2 + 2\pi^3 k_z^2 k_z'^2 k_z''^2\right]}{\kappa\kappa'\kappa''} e^{-\kappa z} e^{-\kappa' z'} e^{-\kappa'' z''}\Big|_{z=z'=R/2, z''=R} \\ = -\frac{3297\hbar c\alpha_1\alpha_2\alpha_3}{16\pi}\frac{1}{(4\pi\varepsilon_0)^3 R^{10}}. \tag{4.76}$$

Mixed TE/TM Contributions

The mixed polarization traces yield six distinct terms. The three TE-dominated terms are:

$$\begin{aligned} \text{Tr}(\mathbf{A}'_e \mathbf{A}''_e \mathbf{A}_h) &\to 2\pi^3 \frac{k_z^2}{k^2}, \\ \text{Tr}(\mathbf{A}_e \mathbf{A}''_e \mathbf{A}'_h) &\to 2\pi^3 \frac{k_z'^2}{k'^2}, \\ \text{Tr}(\mathbf{A}_e \mathbf{A}'_e \mathbf{A}''_h) &\to 2\pi^3 \frac{k_z''^2}{k''^2}. \end{aligned} \tag{4.77}$$

Each of these yields:

$$V_1^{\text{TE/TM}}(R) = \frac{153\hbar c\alpha_1\alpha_2\alpha_3}{16\pi}\frac{1}{(4\pi\varepsilon_0)^3 R^{10}}, \quad V_3^{\text{TE/TM}}(R) = \frac{87\hbar c\alpha_1\alpha_2\alpha_3}{16\pi}\frac{1}{(4\pi\varepsilon_0)^3 R^{10}}. \tag{4.78}$$

The TM-dominated mixing terms yield:

$$\begin{aligned} \text{Tr}(\mathbf{A}''_e \mathbf{A}_h \mathbf{A}'_h) &\to 2\pi^3 \frac{k_z^2 k_z'^2}{k^2 k'^2}, \\ \text{Tr}(\mathbf{A}'_e \mathbf{A}_h \mathbf{A}''_h) &\to 2\pi^3 \frac{k_z^2 k_z''^2}{k^2 k''^2}, \\ \text{Tr}(\mathbf{A}_e \mathbf{A}'_h \mathbf{A}''_h) &\to 2\pi^3 \frac{k_z'^2 k_z''^2}{k'^2 k''^2}, \end{aligned} \tag{4.79}$$

leading to

$$V_2^{\mathrm{TE/TM}}(R) = \frac{677\hbar c\alpha_1\alpha_2\alpha_3}{16\pi}\frac{1}{(4\pi\varepsilon_0)^3R^{10}},$$
$$V_{4,5}^{\mathrm{TE/TM}}(R) = \frac{347\hbar c\alpha_1\alpha_2\alpha_3}{16\pi}\frac{1}{(4\pi\varepsilon_0)^3R^{10}}. \tag{4.80}$$

Total Interaction Energy

Summing all contributions:

$$V_{\mathrm{TE}}^{(3)} + V_{\mathrm{TM}}^{(3)} + \sum V_{\mathrm{TE/TM}}^{(3)} = -93\frac{\hbar c\alpha_1\alpha_2\alpha_3}{\pi}\frac{1}{(4\pi\varepsilon_0)^3R^{10}}. \tag{4.81}$$

Finally, noting the symmetry in Eq. (4.30), the full irreducible three-body Casimir–Polder potential for collinear atoms is:

$$V_{\mathrm{CP}}^{(3)}(R) = -186\frac{\hbar c\alpha_1\alpha_2\alpha_3}{\pi}\frac{1}{(4\pi\varepsilon_0)^3R^{10}}. \tag{4.82}$$

This result agrees with the known collinear configuration of three-body dispersion forces derived by Power and Thirunamachandran [65]. The structure of the Green tensor contractions used here is completely general and does not depend on the specific geometry until the final substitution of coordinates. As such, this approach can be extended to configurations like equilateral triangles by updating only the position inputs to the integrals.

REFERENCES CITED

[1] H. B. G. Casimir, Proc. K. Ned. Akad. Wet. **51**, 793 (1948).

[2] S. K. Lamoreaux, Phys. Rev. Lett. **78**, 5 (1997).

[3] E. Buks and M. L. Roukes, Phys. Rev. B **63**, 033402 (2001).

[4] H. Bender, P. W. Courteille, C. Marzok, *et al.*, Phys. Rev. Lett. **104**, 083201 (2010).

[5] T. A. Pasquini, Y. Shin, C. Sanner, *et al.*, Phys. Rev. Lett. **93**, 223201 (2004).

[6] J. M. Obrecht, R. J. Wild, M. Antezza, *et al.*, Phys. Rev. Lett. **98**, 063201 (2007).

[7] E. Lifshitz, J. Exper. Theoret. Phys. USSR **29**, 94 (1956).

[8] I. E. Dzyaloshinskii, E. M. Lifshitz, and L. P. Pitaevskii, Soviet Physics Uspekhi **4**, 153 (1961).

[9] U. Mohideen and A. Roy, Physical Review Letters **81**, 4549 (1998).

[10] H. B. Chan, V. A. Aksyuk, R. N. Kleiman, *et al.*, Phys. Rev. Lett. **87**, 211801 (2001).

[11] A. Larraza and B. Denardo, Physics Letters A **248**, 151 (1998).

[12] R. Decca, D. López, E. Fischbach, *et al.*, Annals of Physics **318**, 37 (2005), special Issue.

[13] R. S. Decca, D. López, E. Fischbach, *et al.*, Phys. Rev. D **75**, 077101 (2007).

[14] G. Bimonte, D. López, and R. S. Decca, Phys. Rev. B **93**, 184434 (2016).

[15] G. L. Klimchitskaya, P. Kuusk, and V. M. Mostepanenko, Phys. Rev. D **101**, 056013 (2020).

[16] V. M. Mostepanenko, Int. J. Mod. Phys. A **31**, 1641020 (2016), arXiv:1604.01328 [hep-ph] .

[17] G. L. Klimchitskaya and V. M. Mostepanenko, Phys. Rev. D **95**, 123013 (2017).

[18] P. Brax and P. Brun, Phys. Rev. D **110**, 056015 (2024).

[19] M. Bordag, Phys. Rev. D **75**, 065003 (2007).

[20] C. D. Fosco, F. C. Lombardo, and F. D. Mazzitelli, Phys. Rev. D **86**, 045021 (2012).

[21] S. J. Rahi, T. Emig, N. Graham, *et al.*, Phys. Rev. D **80**, 085021 (2009).

[22] H. Gies, K. Langfeld, and L. Moyaerts, J. High Energy Phys. **2003**, 018 (2003), arXiv:hep-th/0303264 .

[23] H. Gies and K. Klingmüller, J. Phys. A **39**, 6415 (2006), arXiv:hep-th/0511092 .

[24] P. A. M. Dirac, Physikalische Zeitschrift der Sowjetunion **3**, 64 (1933), reprinted in *Quantum Mechanics of Atoms, Molecules, and Photons*, eds. J. C. Slater and N. H. Frank (McGraw-Hill, 1939).

[25] R. P. Feynman, Rev. Mod. Phys. **20**, 367 (1948).

[26] J. Schwinger, Phys. Rev. **82**, 664 (1951).

[27] J. B. Mackrory, T. Bhattacharya, and D. A. Steck, Phys. Rev. A **94**, 042508 (2016), arXiv:1606.00150 .

[28] J. B. Mackrory, H. Zheng, and D. A. Steck, Phys. Rev. A **110**, 042826 (2024), arXiv:2407.06470 .

[29] H. B. G. Casimir and D. Polder, Phys. Rev. **73**, 360 (1948).

[30] H. B. Chan, V. A. Aksyuk, R. N. Kleiman, *et al.*, Science **291**, 1941 (2001).

[31] D. M. Harber, J. M. Obrecht, J. M. McGuirk, and E. A. Cornell, Phys. Rev. A **72**, 033610 (2005), arXiv:cond-mat/0506208 .

[32] H. Gies and K. Klingmuller, Phys. Rev. Lett. **96**, 220401 (2006), arXiv:quant-ph/0601094 .

[33] H. Gies and K. Klingmuller, Phys. Rev. Lett. **97**, 220405 (2006), arXiv:quant-ph/0606235 .

[34] H. Gies and K. Klingmuller, Phys. Rev. D **74**, 045002 (2006), arXiv:quant-ph/0605141 .

[35] K. Klingmuller and H. Gies, J. Phys. A **41**, 164042 (2008), arXiv:0710.4473 .

[36] A. Weber and H. Gies, Phys. Rev. D. **80**, 065033 (2009), arXiv:0906.2313 .

[37] C. Fosco, F. Lombardo, and F. Mazzitelli, Phys. Lett. B **690**, 189 (2010), arXiv:0912.0886 .

[38] A. Weber and H. Gies, Phys. Rev. Lett. **105**, 040403 (2010), arXiv:1003.0430 .

[39] K. Aehlig, H. Dietert, T. Fischbacher, and J. Gerhard, (2011), arXiv:1110.5936 .

[40] M. Schäfer, I. Huet, and H. Gies, Int. J. Mod. Phys. Conf. Ser. **14**, 511 (2012), arXiv:1112.0469 .

[41] D. Mazur and J. S. Heyl, Phys. Rev. D **91**, 065019 (2015).

[42] M. Schäfer, I. Huet, and H. Gies, J. Phys. A **49**, 135402 (2016), arXiv:1509.03509 .

[43] C. Schneider, G. Torgrimsson, and R. Schutzhold, Phys. Rev. D **98**, 085009 (2018), arXiv:1806.00943 .

[44] S. Franchino-Viñas and H. Gies, Phys. Rev. D **100**, 105020 (2019), arXiv:1908.04532 .

[45] O. Corradini and M. Muratori, J. High Energy Phys. **2020**, 169 (2020), arXiv:2006.02911 .

[46] K. Rajeev, Phys. Rev. D **104**, 105014 (2021), arXiv:2105.12194 .

[47] F. Bastianelli and M. D. Paciarini, Class. Quantum Grav. **41**, 115002 (2024), arXiv:2305.06650 .

[48] A. Scardicchio and R. L. Jaffe, Nucl. Phys. B **743**, 249 (2006), arXiv:quant-ph/0507042 .

[49] P. Glasserman, *Monte Carlo Methods in Financial Engineering* (Springer, 2004).

[50] S. Asmussen and P. W. Glynn, *Stochastic Simulation* (Springer, 2007).

[51] A. Matacz, J. Comput. Finance **6**, 79 (2002), arXiv:cond-mat/0005319 .

[52] C. Predescu, J. Math. Phys. **44**, 1226 (2003), arXiv:math-ph/0209058 .

[53] M. Kac, Trans. Amer. Math. Soc. **64**, 1 (1949).

[54] R. Durrett, *Stochastic Calculus: A Practial Introduction* (CRC Press, 1996).

[55] I. Karatzas and S. E. Shreve, *Brownian Motion and Stochastic Calculus* (Spring-Verlag, 1991).

[56] J. F. Babb, G. L. Klimchitskaya, and V. M. Mostepanenko, Phys. Rev. A **70**, 042901 (2004), arXiv:quant-ph/0405163 .

[57] T. Schoger, B. Spreng, G.-L. Ingold, *et al.*, Int. J. Mod. Phys. A **37**, 2241005 (2022), arXiv:2205.10812 .

[58] P. Lévy, Comptes Rendus Hebdomadaires des Séances de l'Académie des Sciences **208**, 318 (1939).

[59] R. Folman, P. Kruger, J. Schmiedmayer, *et al.*, Microscopic atom optics: From wires to an atom chip (2002), arXiv:0805.2613 [quant-ph] .

[60] J. Fortágh and C. Zimmermann, Rev. Mod. Phys. **79**, 235 (2007).

[61] M. Levin, A. P. McCauley, A. W. Rodriguez, *et al.*, Phys. Rev. Lett. **105**, 090403 (2010), arXiv:1003.3487 .

[62] J. N. Munday, F. Capasso, and V. A. Parsegian, Nature **457**, 170 (2009), arXiv:1003.3487 .

[63] P. S. Venkataram, S. Molesky, P. Chao, and A. W. Rodriguez, Phys. Rev. A **101**, 052115 (2020).

[64] E. A. Power and T. Thirunamachandran, Proc. R. Soc. Lond. A **372**, 265 (1980).

[65] E. A. Power and T. Thirunamachandran, Proc. R. Soc. Lond. A **401**, 267 (1985).

[66] S. G. Johnson, in *Casimir Physics*, Lecture Notes in Physics, Vol. 834, edited by D. Dalvit, P. Milonni, D. Roberts, and F. da Rosa (Springer Berlin Heidelberg, Berlin, Heidelberg, 2011) p. 175.

[67] R. L. Jaffe and A. Scardicchio, Phys. Rev. Lett. **92**, 070402 (2004), arXiv:quant-ph/0310194 .

[68] A. Scardicchio and R. Jaffe, Nucl. Phys. B **704**, 552 (2005), arXiv:quant-ph/0406041 .

[69] H. Zheng, J. B. Mackrory, and D. A. Steck (2025), in preparation